

Active Friction Control via Piezoelectrically Generated Ultrasonic Vibrations

THESIS

Presented in Partial Fulfillment of the Requirements for the Degree Master of Science in
the Graduate School of The Ohio State University

By

Shravan Bharadwaj

Graduate Program in Mechanical Engineering

The Ohio State University

2009

Master's Examination Committee:

Dr. Marcelo J. Dapino, Advisor

Dr. S. John Yu

© Copyright by
Shravan Bharadwaj
2009

ABSTRACT

The ability to control the effective friction coefficient between sliding surfaces is a problem of significant interest in automotive applications. For reducing friction, lubricants or different material combinations are typically used. In this research, the role of ultrasonic vibrations on the friction coefficient between sliding surfaces is investigated, with the goal of being able to control the friction coefficient in an automotive seat belt system by modulating the vibrations at the interface between the D-ring and seat belt webbing. These ultrasonic vibrations are generated using piezoelectric materials that respond mechanically to an electrical input. To that end, a systematic approach is developed, with the help of experiments and models, to predict and characterize the frictional force between sliding surfaces in the presence of ultrasonic vibrations under various controlling parameters.

The applied ultrasonic vibrations may be tangential, perpendicular or out-of-plane to the direction of sliding velocity. For rigid surfaces in contact, maximum friction reduction has been reported in the case of tangential vibrations. It has been shown that the extent of friction reduction depends on the ratio of the velocity of the ultrasonic vibrations to the sliding velocity. A series of experiments over a wide range of loads and speeds are designed to characterize the friction reduction effect between solid-solid contacts and Hertzian contacts in the case of seat belts. Using Coulomb and

Dahl friction models, the mechanism of friction reduction in the presence of ultrasonic vibrations is studied.

System level analytical modeling is presented which consists of a single degree-of-freedom model with LuGre friction at the sliding interface. By controlling parameters such as load, system stiffness, contact stiffness and the control force generated by the piezoelectric stack, characterization plots are obtained which can help optimize design parameters of ultrasonic lubrication systems.

In summary, this research investigates the potential of ultrasonic vibrations in actively controlling friction in automotive seat belt systems and other systems in which the use of lubricants is undesirable. For a given ultrasonic power, the extent of reduction decreases at higher speeds and loads. Active control of friction would help improve the performance, efficiency and lifetime of general sliding mechanisms.

To my uncle and aunt, Suresh Sundaresan and Raji Ayer

ACKNOWLEDGMENTS

I would like to express my sincere gratitude towards my advisor, Prof. Marcelo Dapino, for his continuous guidance, understanding, and patience during my M.S. program. My stay at OSU has been most fruitful in terms of knowledge, time management, technical writing and presentation. Prof. Dapino's professional and systematic way of training takes all credit for my development in these areas. This research would not have been possible without his insightful ideas, suggestions and enthusiasm.

I would also like to thank Doug Longhitano, Chuck Thomas and Duane Detwiller of Honda R&D Americas Inc., for mentoring me during this research. Their valuable input has helped me appreciate the design and development of various automotive systems related to my work. I would like to thank the Smart Vehicle Concepts Center for sponsoring this research.

I am grateful to Dr. Karl Graff at Edison Welding Institute for his guidance and help in addressing various technical issues. The knowledge acquired through his short course on ultrasonics has been invaluable towards my research.

I would like to thank Dr. S. John Yu for being on my thesis examination committee and providing his valuable insights. I am thankful to all my colleagues at the Smart Materials and Structures Lab, especially Brett Burton, Suryarghya Chakrabarti, Phillip Evans, Arjun Mahadevan and Ryan Hahnen for their help in

addressing various experimental and theoretical issues. I would like to extend my sincere gratitude towards Joe West at the Student Electronics Shop who has provided me useful technical guidance many times, and Neil Gardner at the Student Machine Shop for his assistance in building a number of test setups.

Finally, I would like to thank my parents and my sister for all their love and encouragement. I am truly indebted to Sthiti for her steadfast support and faith in me. She has been instrumental in instilling patience and strength in me.

VITA

October 1, 1982 Born - Calcutta, India

May 2004 B.Tech., Mechanical Engineering
National Institute of Technology,
Tiruchirappalli, India

2004-2007 Assistant Manager,
Vehicle Body Design,
Suzuki Motor Corporation, India

2008-Present Graduate Research Associate,
The Ohio State University,
Columbus, OH

PUBLICATIONS

Research Publications

S. Bharadwaj, M. J. Dapino, “*Effect of Load on Active Friction Control using Ultrasonic Vibrations,*” Proceedings SPIE Smart Structures/NDE, Paper 7290-15, 2009

FIELDS OF STUDY

Major Field: Mechanical Engineering

Studies in Smart Materials and Structures: Prof. M. Dapino

TABLE OF CONTENTS

	Page
Abstract	ii
Dedication	iv
Acknowledgments	v
Vita	vii
List of Tables	xi
List of Figures	xii
Chapters:	
1. Introduction	1
1.1 Friction	1
1.1.1 Rules of Sliding Friction	2
1.1.2 Mechanisms of Sliding Friction	2
1.2 Active Friction Control	5
1.3 Problem Definition	8
1.4 Statement of Work	10
2. Generation of Ultrasonic Vibrations using Piezoelectric Materials	12
2.1 Ultrasonics	12
2.1.1 Elements of Ultrasonic Waves	13
2.1.2 Wave Propagation	14
2.2 Piezoelectricity	17
2.2.1 The Piezoelectric Effect	18
2.2.2 Parameters for Piezoelectric Effect	20

2.3	Ultrasonic Transducers	26
2.3.1	Ultrasonic Transducer Design	27
3.	Experimental Work	32
3.1	Experiment #1: Low Load, Low Speed	32
3.1.1	Objective	32
3.1.2	Design of Ultrasonic Transducer	32
3.1.3	Design of Experimental Setup	34
3.1.4	Experimental Results	36
3.1.5	Discussion	37
3.2	Experiment #2: High Load, Low Speed	41
3.2.1	Objective	41
3.2.2	Design of Experimental Setup	42
3.2.3	Experimental Results	44
3.2.4	Discussion	49
4.	Analytical Modeling	50
4.1	Friction Models	50
4.1.1	Coulomb Model	50
4.1.2	Dahl Model	52
4.1.3	LuGre Model	54
4.2	System Model	56
4.3	Simulation Results	60
4.3.1	Time and Frequency Domain Plots	63
4.3.2	Energy Considerations	67
4.3.3	Effect of Controlling System Parameters	71
4.3.4	Correlation with Experimental Data	80
4.4	Influence of Tangential Excitation Waveforms	81
4.4.1	Effect of Excitation Waveforms on Dahl Equation	81
4.4.2	Effect of Excitation Waveforms on SDOF Model	84
4.5	Summary	85
5.	Conclusion	90
5.1	Summary	90
5.2	Conclusions	92
5.3	Future Work	93

Appendices:

A.	Experiment # 1 Test Setup Drawings	95
B.	Design and Prototyping of an Ultrasonic Motor	109
B.1	Ultrasonic Motor	109
B.2	Mechanism of USMs	109
B.2.1	Equations of Motion	112
B.2.2	Motion of Particle on Stator Surface	114
B.3	Simulation Results	115
B.4	Fabrication of Prototype	115
B.4.1	Selective Removal of Electrode Coating	118
B.4.2	Phase Shifter Circuit	120
B.5	Experimental Setup	120
B.6	Laser Vibrometer Measurements	122
B.7	Final Prototype	123
B.8	Conclusion	125
	Bibliography	126

LIST OF TABLES

Table	Page
2.1 Wave Parameters	14
3.1 Transducer Specifications	35
3.2 Dukane Ultrasonic Transducer Specifications	42
4.1 Simulation Parameters	61
B.1 USM Simulation Parameters	115

LIST OF FIGURES

Figure	Page
1.1 Active friction control in seat belt system.	10
2.1 Propagating harmonic wave.	13
2.2 Basic types of elastic waves (a) Pressure (b) Shear (c) Surface. . . .	15
2.3 Successive instants in the propagation of a harmonic wave.	16
2.4 A thin rod (a) with coordinate x and displacement u of a section; (b) the stresses acting on differential element of rod.	17
2.5 First three mode shapes of vibration of a free-free rod.	18
2.6 The piezoelectric effect (a) Longitudinal (b) Transverse.	19
2.7 Dielectric strain characteristics for a PLZT piezoelectric ceramic. . .	20
2.8 Representation of strain induced by pole reversals in ceramic materials.	22
2.9 Coordinate axes and corresponding subscript numbers.	23
2.10 Piezoelectric stress vs. strain characteristics (a) without prestressing (b) increase in stress limit with prestressing.	27
2.11 Cross section of a high power piezoelectric ultrasonic transducer. . .	28
2.12 (a) Half wavelength stepped horn (b) Commercial booster (<i>Courtesy: Edison Welding Institute</i>).	29
2.13 Family of transducers with variable ceramic location.	30

3.1	PMN-PT stack ultrasonic transducer.	34
3.2	Rendering of experimental setup.	36
3.3	Experimental setup for measuring the average frictional force with and without ultrasonic vibrations at various sliding velocities.	37
3.4	Friction force measured at transducer velocity of 0.038 m/s in (a) OFF state and (b) OFF/ON state.	38
3.5	Friction force measured at transducer velocity of 0.068 m/s in (a) OFF state and (b) OFF/ON state.	39
3.6	Experimental setup.	43
3.7	Effect of duration of ultrasonics ON time on friction reduction.	45
3.8	Effect of load on friction force in the OFF state.	46
3.9	Effect of load on friction reduction at 50% amplitude.	47
3.10	Effect of load on friction reduction at 70% amplitude.	47
3.11	Effect of vibration amplitude on friction reduction at 270 N.	48
3.12	Effect of vibration amplitude on friction reduction at 450 N.	48
4.1	Coulomb friction model.	51
4.2	Dahl friction model.	53
4.3	LuGre friction model.	54
4.4	Single degree-of-freedom model of ultrasonic transducer.	57
4.5	Simulink block diagram for system model with LuGre Friction.	59
4.6	Comparison of Coulomb and Dahl model-Friction ratio versus velocity ratio.	60

4.7	Instantaneous friction force vs. time using (a) Coulomb model (b) Dahl model.	62
4.8	(a) Displacement vs. time (b) Velocity vs. time.	64
4.9	(a) Instantaneous friction force vs. time (b) Instantaneous power dissipation vs. time.	65
4.10	Fast Fourier Transform of (a) Velocity (b) Friction force.	66
4.11	Effect of control force on (a) Friction ratio vs. velocity ratio (b) Power dissipation ratio vs. velocity ratio.	75
4.12	Effect of coefficient of friction on (a) Friction ratio vs. velocity ratio (b) Power dissipation ratio vs. velocity ratio.	76
4.13	Effect of load on (a) Friction ratio vs. velocity ratio (b) Power dissipation ratio vs. velocity ratio.	77
4.14	Effect of friction induced oscillations on (a) Friction ratio vs. velocity ratio (b) Power dissipation ratio vs. velocity ratio.	78
4.15	Effect of system stiffness on (a) Friction ratio vs. velocity ratio (b) Power dissipation ratio vs. velocity ratio.	79
4.16	Comparison of various models with experimental data.	80
4.17	Dahl friction force vs. time.	82
4.18	Instantaneous power vs. time.	82
4.19	Friction ratio versus velocity ratio.	83
4.20	Power dissipation ratio versus velocity ratio.	83
4.21	Displacement vs. time.	86
4.22	Velocity vs. time.	86
4.23	Friction force vs. time.	87

4.24	Instantaneous power dissipated vs. time.	87
4.25	Friction ratio versus velocity ratio.	88
4.26	Power dissipation ratio versus velocity ratio.	88
A.1	Experimental #1 setup.	95
A.2	#6-32 nut.	96
A.3	Preloading screw with #6-32 thread.	97
A.4	Aluminum transducer shell.	98
A.5	Aluminum transducer shell.	99
A.6	Connector bracket.	100
A.7	Cross arm.	101
A.8	Guide rail.	102
A.9	Pillar.	103
A.10	Pillar Extension.	104
A.11	Rocker arm.	105
A.12	Slider arm.	106
A.13	Support.	107
A.14	L-Bracket.	108
B.1	Ultrasonic motor and parts.	110
B.2	Principle of traveling wave USM.	110
B.3	Classification of USMs.	111
B.4	A beam in bending.	112

B.5	Simulation results	116
B.6	Plot of Y-displacement vs. Z-displacement.	116
B.7	PZT-5A piezoelectric sheet with Nickel electrodes.	117
B.8	PZT-5A piezoelectric sheet properties.	118
B.9	Selective removal of Ni electrode on piezo sheet.	119
B.10	All pass filter circuit.	121
B.11	All pass filter circuit implementation.	121
B.12	Drive electronics for USM.	122
B.13	Final prototype of ultrasonic motor.	123
B.14	Displacement measurement by laser vibrometer at 20 kHz.	124
B.15	Displacement measurement by laser vibrometer at 40 kHz.	124

CHAPTER 1

INTRODUCTION

1.1 Friction

Friction is defined as the resistance to sliding or rolling motion when one body moves tangentially over another [2]. This resistive tangential force acts in a direction directly opposite to the direction of motion. There are two main types of friction that are commonly encountered: dry friction and fluid friction. Dry friction, also called ‘Coulomb’ friction, describes the tangential component of the contact force that exists when two dry surfaces move or tend to move relative to one another. Fluid friction describes the tangential component of the contact force that exists between adjacent layers in a fluid that are moving at different velocities relative to each other as in a liquid or gas between bearing surfaces.

When two solid bodies are loaded together, the tangential force required to initiate motion is the static friction force, $\mathbf{F}_{\text{static}}$. It takes finite time before relative motion is initiated at the interface. The tangential force required to maintain relative motion is known as the kinetic (or dynamic) friction force, $\mathbf{F}_{\text{kinetic}}$. Friction is not a material property, it is a system response.

1.1.1 Rules of Sliding Friction

There are two basic rules of intrinsic friction, referred to as Amontons' equations. The first rule defines the friction force, \mathbf{F} by the following equation:

$$\mathbf{F} = \mu \mathbf{N} \quad (1.1)$$

where μ is a constant called the coefficient of friction and is independent of the normal load N .

The second rule states that the friction force is independent of the apparent area of contact between the bodies. Thus two bodies, regardless of their physical size, have the same coefficient of friction.

Sometimes, a third rule is added to the above two rules. It states that the kinetic friction force is independent of the sliding velocity once motion starts.

These three rules are entirely empirical; situations in which these rules are not followed do not imply violation of more fundamental laws of nature.

At microscopic scales, these rules do not necessarily hold. The coefficient of friction is strictly constant only for a given pair of sliding materials under a given set of operating conditions (temperature, humidity, normal pressure and sliding velocity).

1.1.2 Mechanisms of Sliding Friction

Initially, it was proposed that metallic friction can be attributed to mechanical interactions of asperities on the contacting surfaces. In the Coulomb model, it is assumed that wedge-shaped asperities cause the two surfaces to move apart as they slide and then come close again. Work is done in raising the asperities from one position to another and most of the potential energy stored in one phase of the

motion is recovered as surfaces move back. Only a fraction of energy is dissipated during sliding down the asperities. Since friction is a dissipative process, this theory of mechanical interactions was abandoned. A realistic friction theory should include mechanisms of energy dissipation. As explained by Bhushan [2], the following are basic mechanisms of dissipative friction:

1.1.2.1 Adhesion

When two nominally flat surfaces are placed in contact under load, the contact takes place at the tips of the asperities, and discrete contact spots (junctions) are formed. The sum of the areas of all the contact spots constitutes the real (true) area of contact and for most materials this is only a small fraction of the apparent (nominal) area of contact [2]. The proximity of the asperities results in adhesive contacts caused by either physical or chemical interaction. When these two surfaces move relative to each other, a lateral force is required to shear the adhesive bonds formed at the interface in the regions of the real area of contact. Rupture occurs in the weakest regions, either at the interface or in one of the mating bodies. After shearing of existing contacts, new contacts are formed. Since adhesion arises from molecular forces between the surfaces, the adhesive forces are of the same nature as forces existing between the molecules themselves. Consequently, the interface may be as strong as the bulk materials, and during sliding the shearing process may tear fragments of materials. The adhesion strength of the interface depends on the mechanical properties and the physical/chemical interaction of the contacting bodies. Adhesion strength is reduced by reducing surface interactions at the interface. Thus, a deliberately applied fluid film would reduce the adhesion strength and hence friction force.

1.1.2.2 Deformation

During sliding, there are two types of interaction that occurs. Microscopic interaction where primarily plastic deformation and displacement of the interlocking surface asperities is required, and the more macroscopic interaction where the asperities of the harder material either plough grooves in the surface of the softer one via plastic deformation or result in fracture, tearing, or fragmentation. Ploughing can also occur by wear particles trapped between them, and truly macroscopic ploughing of the softer material by the harder, with dimensions of the ploughed groove being orders of magnitude greater than those of the asperities. Due to ploughing displacement, a certain lateral (friction) force is required to maintain motion. Ploughing not only increases friction force, it creates wear particles, which in turn increase subsequent friction and wear. The dominant mechanism of energy dissipation in metals is plastic deformation. In the case of viscoelastic materials, the deformation included energy loss caused by a delayed recovery of the material after indentation by a particular asperity, and gives rise to the hysteresis friction.

1.1.2.3 Ratchet Mechanism

If asperities of one surface are significantly smaller in lateral dimensions than that of the mating surface and contact stresses are lower than plastic flow stress, sharper asperities climb up and down over broader asperities without creating interfacial damage. Energy (or force) is required to climb up the asperity of a given slope, and it decreases during climbing down. In sliding down the asperity, there may be impact energy and energy may be lost either by impact deformation or by generation of phonons. This mechanism resembles the Coulomb model. Surface roughness also has

an influence if adhesive friction is present. These roughness effects are important if one surface is compliant (such as fibers sliding on a hard surface) or one surface is much rougher than another surface with comparable hardness.

1.1.2.4 Structural Effects

Hexagonal close-packed (HCP) metals exhibit low coefficient of friction and much less wear (about 30%) than face-centred cubic (FCC) metals. The key factor which affects friction and wear is the number of slip planes.

1.1.2.5 Grain Boundary Effects

For polycrystalline materials, the presence of grain boundaries in the material influences adhesion and friction behavior, surface fracture and wear. The near surface dislocations in the sliding process are blocked in their movement by a grain boundary, they accumulate at the grain boundary and produce strain hardening at the surface layers. This strain hardening makes it more difficult for sliding and increases friction force of materials in sliding contact.

1.2 Active Friction Control

Conventional methods of reducing friction rely on lubricants and suited material combinations. A thin layer of lubricant avoids contact and interfacing between the asperities on either surfaces and hence reduces friction. As the layer of lubricant becomes thicker, viscous friction comes into play. The behavior and effectiveness of lubricants are strongly dependent on temperature, pressure and shear rate. Lubrication may be hydrostatic, hydrodynamic, elastohydrodynamic, mixed or boundary layer. These regimes are based on the Stribeck curve [2]. This plot for a hypothetical

fluid-lubricated bearing system presents the coefficient of friction as a function of the product of absolute viscosity (η) and rotational speed in revolutions per unit second (N) divided by the load per unit projected bearing area (P). The regimes of lubrication are identified by the lubricant film parameter equal to h/σ , which is the mean film thickness divided by the composite standard deviation of surface heights of the two surfaces.

The need for active control of friction arises in sliding mechanisms which operate under varying conditions of load and speed. This has been of technological interest in automotive systems such as gear trains, seat belts, sliding doors, etc. One proven and effective way of controlling friction actively is by the superimposition of ultrasonic vibrations on the sliding motion. A number of researchers have studied this phenomenon of ultrasonically induced friction reduction.

The reduction in static friction by sonic vibrations was first described by Fridman and Levesque in 1959 [5]. It was later investigated by Pohlman and Lefeldt [23]. Hesjedal et al. [9] demonstrated the effect of friction reduction caused by Rayleigh type surface acoustic waves. By increasing the wave amplitude, friction was found to be completely suppressed in microscopic mechanical contacts. Many studies on the influence of contact micro vibrations on the friction force suggest that this force can be reduced by ultrasonic vibrations superimposed both in the normal and tangential direction to the plane of contact. Depending on the direction of vibration, the friction reduction can be explained either in terms of change in magnitude and direction of the resultant sliding velocity vector, or in terms of a change in magnitude of the normal load. The former effect occurs in case of in-plane vibrations, both tangential and perpendicular in the plane containing the interacting surfaces, whereas the latter

applies in the case of out-of-plane normal vibrations. The effect of normal vibrations on friction was studied by Hess and Soom [10]. As a result of the nonlinear Hertzian stiffness, the average normal contact deflection during oscillations is smaller than the static deflections under the same average load. This results in a reduction in the average area of contact, and hence average friction force. The maximum average friction reduction without contact loss is reported to be approximately ten percent. The ability of ultrasonic vibrations to reduce friction has been applied in machining processes such as drilling, cutting and wire drawing. Kumar and Hutchings [13] conducted experiments for different sets of interacting materials under the influence of ultrasonics. At high vibration amplitudes however, the reduction in friction was less than predicted by models, and was attributed to significant metallic transfer between the surfaces.

The first theoretical model describing the influence of longitudinal vibrations on the friction force was presented by Mitskevich [20]. According to this model, it is possible to reduce the average friction force through a cyclic and instantaneous change of the vector sign of this force registered in every vibrations period provided that the amplitude of the vibration is higher than the constant component of the sliding motion velocity. This phenomenon described as the friction vector effect is commonly regarded as one of the most important mechanisms which can lower the friction force in sliding motion under the influence of tangential vibrations. Littmann et al [17],[18] and [25] used the Coulomb friction in order to model this phenomenon. However, there were discrepancies in comparison with results obtained by experiment. Leus and Gutowski [15] and Tsai and Tseng [27] developed models based on Dahl friction

which takes into account the contact deformation at the interface. A much better agreement of friction force calculations was obtained using Dahl’s friction model.

A related application of ultrasonic vibrations is the suppression of friction-induced oscillations. Typically, there are two phases of such oscillations: a stick phase with no slippage between parts and friction forces limited by static friction, followed by a slip phase with a lower friction force. Since these oscillations occur without any external periodic input, they are called self-excited [8]. Superimposition of high frequency signals or dither has been successfully used in reducing these friction driven oscillations which give rise to unwanted effects like squeal noise. Dither control is characterized by the application of a control effort at a frequency higher than the disturbance controlled [3]. Extensive research has been conducted in the area of dither control for suppression of automotive brake squeal. Dither signals are known to eliminate the stick-slip oscillations causing an effective decrease in the friction force. The harmonic force generated by piezoelectric ceramics placed within the brake caliper’s piston creates a small variation in the normal clamping force and a small reduction in the braking torque ($< 2\%$) was reported in experiments [1].

1.3 Problem Definition

Current seat belt systems include different functions designed to place the occupant into a safe crash position and control the occupant’s energy. Typically, a force or ‘load’ limiting mechanism (based on a deforming torsion bar) is integrated into the seat belt retractor mechanism to control the release the seat belt webbing. This load limiter is used in tandem with a pretensioner which helps remove excess slack in the webbing during the crash. Usually the pretensioner consists of a pyrotechnic

charge and linkage mechanism embedded in the retractor or seat belt buckle which can operate by directly pulling the belt towards the floor or by winding the retractor.

Existing seat belts have a number of design tradeoffs. Seat belts are passive and are designed as a compromise for various occupants and loading conditions. The diameter of the load-limiting torsion bar is selected to achieve a near constant shoulder force. This is an open loop mechanism and the belt tension is proportional to the webbing displacement. Thus, the load limiter is designed for a fixed percentile occupant size under given load conditions. Occupants whose size or load conditions lying outside this envelope may experience excessive or insufficient energy absorption in a crash.

Experimental data suggests that during a crash, small changes in the friction coefficient between the D-ring and the webbing can have a large effect on the chest force relative to the retractor force. By modulating this friction coefficient between ‘high’ and ‘low’ states, it is possible to control the shoulder belt force.

This research is aimed at developing an active seat belt system with the goal of being able to control the friction force at the interface between the D-ring and seat belt webbing. Active control of friction is achieved by superimposing ultrasonic vibrations on the sliding motion (Figure 1.1). With this feature, force control strategies can be developed which would optimally manage the energy of the occupant’s torso. The active seat belt system can thus eliminate the tradeoffs in current suboptimal designs which are designed for a fixed percentile occupant size.

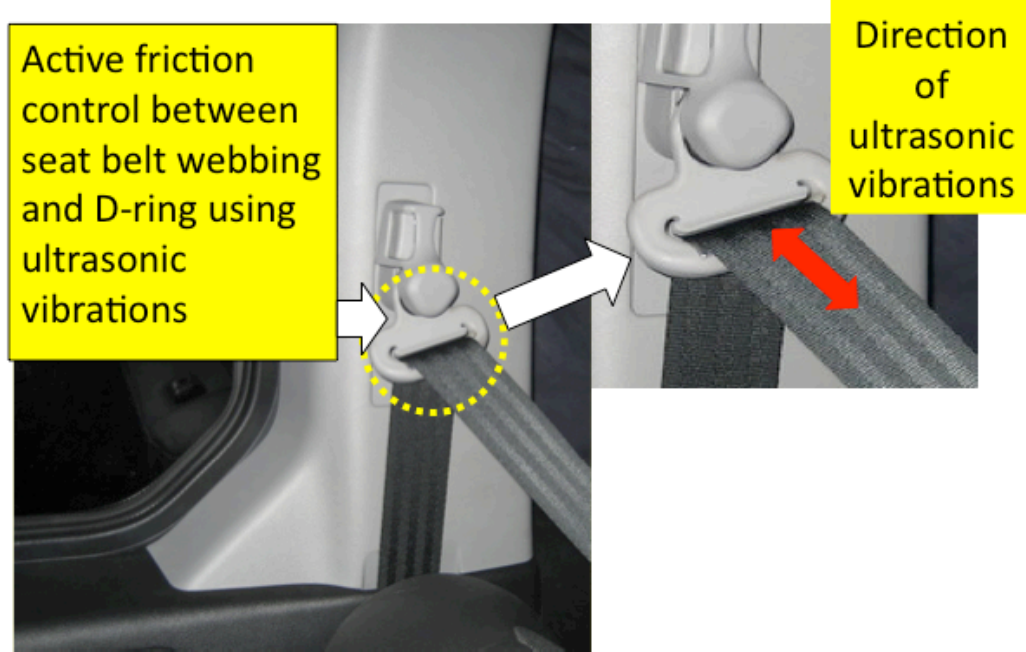


Figure 1.1: Active friction control in seat belt system.

1.4 Statement of Work

Experimental work has been categorized as: (a) Low load and low speed (b) High load and low speed, and (c) High load and high speed. These experiments are devised to demonstrate the concept of ultrasonic lubrication and define the performance envelope for a range of loads and speeds.

Experiment # 1 is a low load (up to 10 N) and low speed (up to 0.068 m/s) setup. Using a piezoelectric PMN-PT stack, a low force ultrasonic transducer is fabricated. The transducer is excited using a high frequency voltage to generate ultrasonic vibrations. The ultrasonic transducer is slid on aluminum guide rails and the friction force at the interface is measured at the interface with and without ultrasonic vibrations.

Friction reduction up to 68% is obtained in these tests. An increase in load was found to be detrimental to the friction reduction effect. These tests were conducted at two different sliding speeds of 0.038 m/s and 0.068 m/s respectively.

Experiment # 2 is a high load (up to 670 N) and low speed (up to 0.025 m/s) setup. Using a commercial Dukane ultrasonic welder, ultrasonic vibrations are generated normal to the direction of sliding motion. A normally loaded seat belt is pulled using a pneumatic cylinder and the friction force is measured with and without ultrasonics. In this case, friction reduction to the extent of 58% is achieved using the high power ultrasonic welder. At high loads, much higher power is required to modulate the high friction forces and obtain a reduction in friction. The effect of vibration amplitudes, load and duration of ultrasonics is studied.

Analytical modeling and finite element simulations have been performed to understand the phenomenon and characterize the friction reduction. A study on the parametric dependence of the friction force in the presence of ultrasonic vibrations is conducted. Various friction models (Coulomb, Dahl and LuGre models) have been studied to explain and predict the reduction in friction in the presence of ultrasonics. The role of system dynamics in friction reduction has been presented in this research. The influence of system excitation waveforms on friction reduction shows that square waves and chirp signals have been found to be most effective in reducing friction.

A concurrent research conducted is the design and fabrication of an ultrasonic motor prototype. Ultrasonic motors are fundamentally friction drives. The development of this motor is complementary to the study of ultrasonic vibrations in controlling friction. These motors have many applications in robotic joints, camera-auto focus mechanisms and linear/rotary actuation.

CHAPTER 2

GENERATION OF ULTRASONIC VIBRATIONS USING PIEZOELECTRIC MATERIALS

2.1 Ultrasonics

Ultrasonics is a branch of acoustics dealing with the generation and use of acoustic waves at frequencies higher than 20 kHz [6]. There are two broad areas of use, sometimes delineated as low and high intensity applications. Thus, low intensity applications typically involve frequencies on the order of 100 Hz or higher, and power levels on the order of milliwatts. High intensity applications will typically involve frequencies of 5 to 100 kHz and powers of hundreds to thousands of watts. The total frequency range of all ultrasonic applications ranges from audible 5 to 10 kHz to as high as 10^{10} Hz. There are also applications, such as sonar, which are exceptions to the previous categorizations, since intense power levels are involved in conveying information via underwater sound.

The term ‘ultrasonics’ is associated with the science of high frequency waves. Other terms, such as ‘ultrasound’ or ‘sonics’ are sometimes used synonymously with ultrasonics. ‘Supersonics’ is used only to designate velocities faster than sound. The

designation of ‘microsonics’ is sometimes used in conjunction with high intensity applications.

2.1.1 Elements of Ultrasonic Waves

For an ultrasonic wave with propagation velocity, c , wave length λ , and period of vibration, T shown in Figure 2.1,

$$\lambda = cT. \quad (2.1)$$

$$\frac{c}{\lambda} = 1/T = f, \quad (2.2)$$

where f is the cyclic frequency.

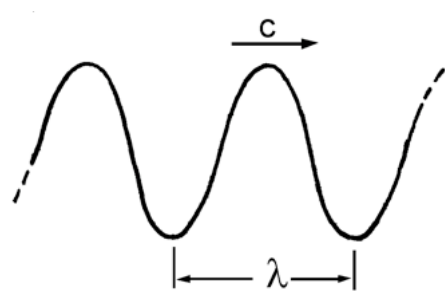


Figure 2.1: Propagating harmonic wave.

In ultrasonics, the range of these parameters is wide. Propagation velocities depend on the material, and range from 0.3×10^3 m/s to 10×10^3 m/s. Wavelengths accordingly vary from 0.5 to 5×10^{-4} m.

Three basic types of wave may exist in a material, depending on whether it is solid or fluid and depending on the nature of its boundaries. The wave types are pressure, shear, and surface waves. The basic natures of the waves are shown in Figure 2.2. The

Table 2.1: Wave Parameters

Symbol	Parameter
A	Amplitude of wave (length)
ω	Radial frequency of wave (radians/time)
f	Cyclic frequency of wave (cycles/time)
γ	Wavenumber of wave (1/length)
c	Phase velocity of wave (length/time)
T	Period of wave (time)

pressure wave (also called a dilatational wave) may exist in solids, liquids, and gases, and is the familiar wave of acoustic theory. Here, the particle motion is in the same direction as propagation direction. A shear wave (also called a transverse wave or an equivoluminal wave), on the other hand, exists only in solids. The particle motion is perpendicular, or transverse to the direction of propagation. These are the only two types of wave that may exist in an extended media. If a free surface exists, a surface (or Rayleigh) wave may propagate. Such a wave has a complicated particle motion at the surface, and has an amplitude that rapidly decoys away from the surface.

2.1.2 Wave Propagation

Ultrasonics involves the propagation of acoustic waves. The basic features of propagating waves and mathematical equations governing wave propagation are described below. The major parameters of the wave are defined in Table 4.1.

$$\omega = \gamma \mathbf{c}, \quad \omega = 2\pi \mathbf{f}, \quad \lambda = 2\pi / \gamma. \quad (2.3)$$

The propagating wave may be described by,

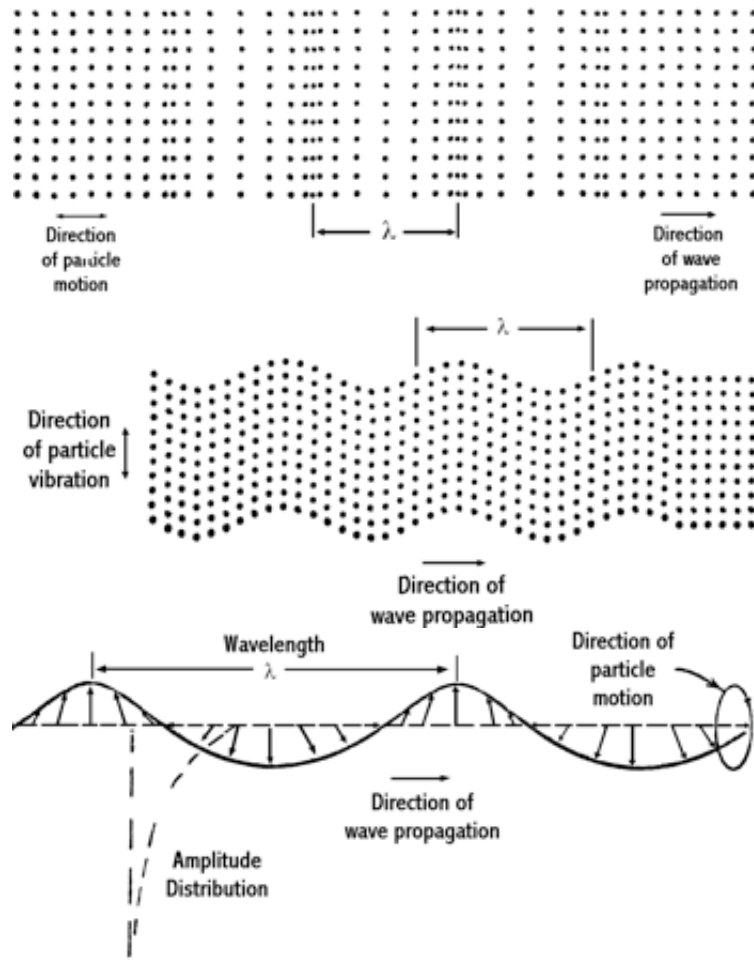


Figure 2.2: Basic types of elastic waves (a) Pressure (b) Shear (c) Surface.

$$y(x, t) = \mathbf{B} \cos(\gamma \mathbf{x} - \omega \mathbf{t}) = \mathbf{B} \cos \gamma(\mathbf{x} - \mathbf{c} \mathbf{t}), \quad (2.4)$$

or,

$$y(x, t) = \mathbf{B} \sin(\gamma \mathbf{x} - \omega \mathbf{t}) = \mathbf{B} \sin \gamma(\mathbf{x} - \mathbf{c} \mathbf{t}), \quad (2.5)$$

where \mathbf{B} is a constant.

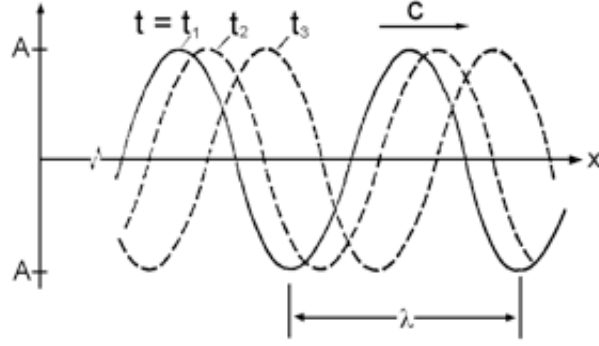


Figure 2.3: Successive instants in the propagation of a harmonic wave.

For a thin rod shown in Figure 2.4, the equation of motion in an element of the rod is

$$-\sigma \mathbf{A} + \left(\sigma + \frac{\partial \sigma}{\partial x} dx\right) \mathbf{A} = \rho A dx \frac{\partial^2 \mathbf{u}}{\partial t^2}, \quad (2.6)$$

where \mathbf{A} is the cross-sectional area and ρ is the mass density. This reduces to

$$\frac{\partial \sigma}{\partial x} = \rho \frac{\partial^2 u}{\partial t^2}. \quad (2.7)$$

For an elastic material,

$$\sigma = \mathbf{E} \epsilon, \quad (2.8)$$

where ϵ is the strain in the material and is defined as

$$\epsilon = \frac{\partial u}{\partial x}. \quad (2.9)$$

Thus, the wave equation in a thin rod is given as

$$\mathbf{E} \frac{\partial^2 \mathbf{u}}{\partial x^2} = \rho \frac{\partial^2 \mathbf{u}}{\partial t^2}. \quad (2.10)$$

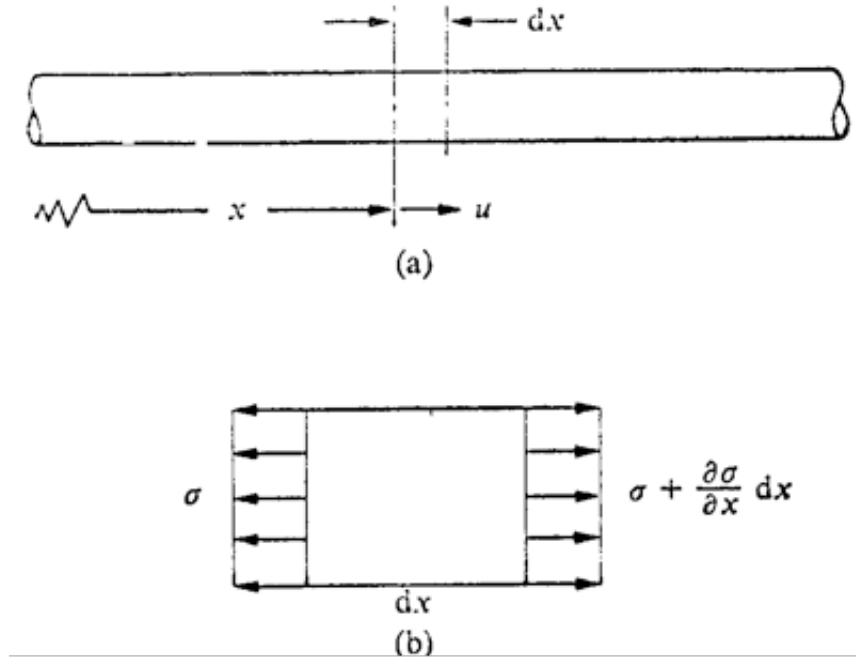


Figure 2.4: A thin rod (a) with coordinate x and displacement u of a section; (b) the stresses acting on differential element of rod.

For a free-free rod of length l in vibration, the vibrational modes are given by

$$U(x) = D \cos \frac{n\pi}{l} x \quad (n = 1, 2, \dots), \quad (2.11)$$

where D is a constant.

The natural frequencies of the rod are given by

$$\omega_0 = \frac{n\pi c_0}{l}, \quad f_n = \frac{nc_0}{2l}. \quad (2.12)$$

The first three mode shapes are shown in Figure 2.5.

2.2 Piezoelectricity

Piezoelectric materials possess the ability of producing mechanical work when they are electrically excited or generating electrical energy if they are mechanically

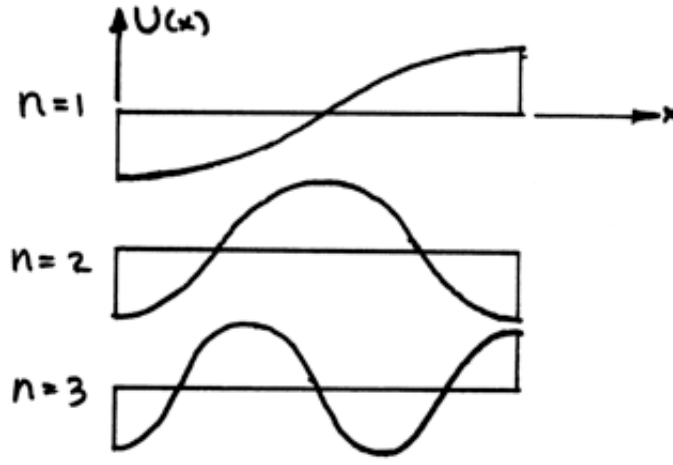


Figure 2.5: First three mode shapes of vibration of a free-free rod.

stressed [11]. Elements such as tourmaline and quartz are inherently piezoelectric. Other ceramic elements that are not naturally piezoelectric, such as barium titanate, can be transformed to quasi-piezoelectric by poling. An ultrasonic transducer utilizes this unique property of piezoelectric materials and converts the input electrical energy to ultrasonic mechanical vibrations.

2.2.1 The Piezoelectric Effect

J. Curie and P. Curie discovered the piezoelectric effect in quartz in 1880. Certain types of crystals when subjected to tensile or compressive forces (or stresses) results in a polarized state in the crystal. Conversely, if the crystal is being polarized by an electric field, strains along with resulting stresses are created. Together, these two effects are known as the piezoelectric effect. In crystals which show piezoelectric properties, mechanical quantities, such as stress (T) or strain (S), and electrical quantities such as electric field (E), electric displacement (flux density) or polarization (P), are interrelated. This phenomenon is called electromechanical coupling.

Longitudinal and transverse effects in the piezoelectric phenomena are particularly important. In the longitudinal effect, deformations take place parallel to the electric axis as shown in Figure 2.6 (a). Figure 2.6 (b) illustrates the transverse effect deformations occurring at right angles to the electric axis. In practice, these two types of effect take place at the same time.

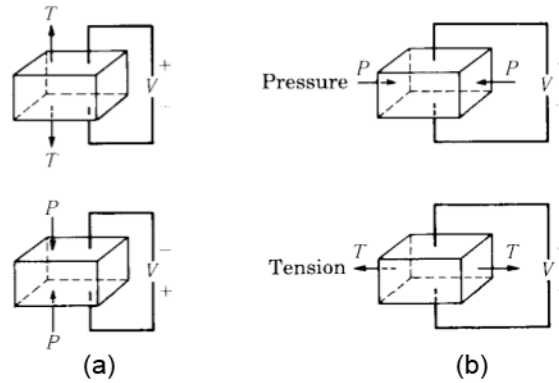


Figure 2.6: The piezoelectric effect (a) Longitudinal (b) Transverse.

When a crystal is placed in an electric field, two types of strain can be observed, one is proportional to the field strength and the other is proportional to the square of the field strength. Strictly speaking, the former represents the piezoelectric effect while the latter is sometimes distinguished as the electrostrictive phenomenon. Practical piezoelectric ceramics have a complex multidomain structure under the microscope and exhibit quite complex behavior. Figure 2.7 is a plot of strain in the direction of the applied electric field (i.e., longitudinal effect) for a PLZT material (materials whose main composites are $(\text{Pb}, \text{La})(\text{Zr}, \text{Ti})\text{O}_3$) [24]. This property is referred as hysteresis as the state of the material is determined by its previous history.

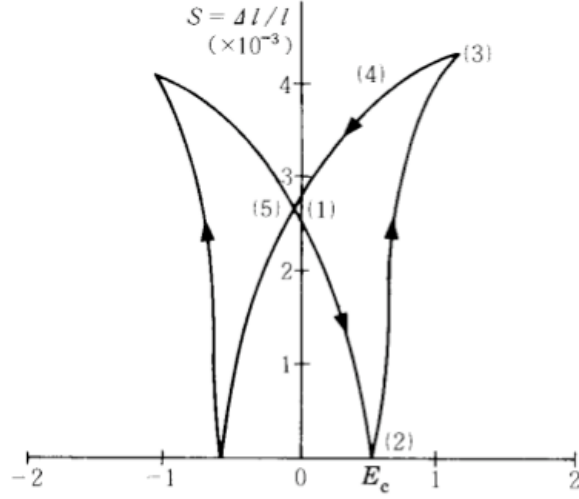


Figure 2.7: Dielectric strain characteristics for a PLZT piezoelectric ceramic.

2.2.2 Parameters for Piezoelectric Effect

1. Polarization(P)

The polarization, P , is related to the electric displacement (or electric flux density) D through the linear expression

$$D_i = P_i + \varepsilon_0 E_i, \quad (2.13)$$

where the subscript i represents any of the three coordinates x, y and z , and ε_0 is the permittivity of free space, equal to $8.854 \times 10^{-12} \text{ Fm}^{-1}$.

2. *Permittivity (ϵ)*

Permittivity is defined as the incremental change in electric displacement per unit electric field when the magnitude of the measuring field is very small compared to the coercive electric field denoted by E_C in Figure 2.8.

3. *Remnant Polarization*

Remnant polarization is the value of the polarization that remains after an electric field is removed.

4. *Poling and Switching*

Poling is a process by which a D.C. electric field exceeding the coercive field is applied to a specimen of multi-domain ceramic to produce a net remnant polarization. In Figure 2.8, the crystal is initially polarized in the negative direction and each domain is polarized in the downward direction. If an electric field in the positive direction is gradually applied, the block contracts initially since the field opposes the polarized direction. As strength of the electric field increases, some of the poles in the grains begin to reverse their directions. At a certain voltage, the block will no longer be able to contract further.

This electric field is known as the coercive field, E_C as indicated in Figure 2.8. If the field continues to increase, the ceramic block expands. At field E_{max} , all the poles are reversed and the block does not expand any further. If the electric field is reduced, the strain will keep decreasing until the electric field reaches zero. In the final state, the poles in all the grains are reversed from the initial state and the block is polarized in the positive direction.

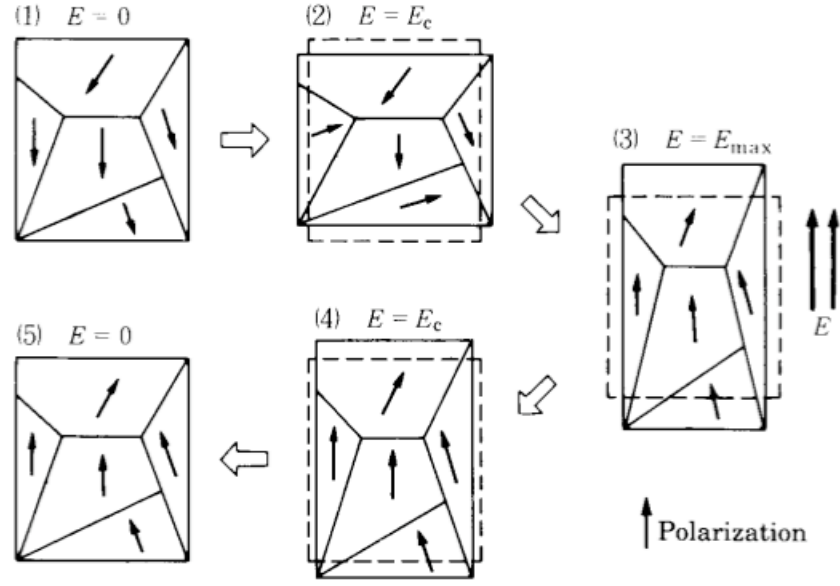


Figure 2.8: Representation of strain induced by pole reversals in ceramic materials.

5. Piezoelectric Strain Constant (d)

Strain and applied voltage are proportional in a polarized crystal. Ignoring hysteresis effects, their relationship can be expressed as,

For positive polarized state

$$\frac{\Delta l}{l} = d\mathbf{E}. \quad (2.14)$$

For negative polarized state

$$\frac{\Delta l}{l} = -d\mathbf{E}. \quad (2.15)$$

The proportionality constant d is known as the piezoelectric strain constant.

6. Poisson's Ratio (σ^E)

Piezoelectric strains are generally extremely small. Strain constant (d) ranges typically from 10^{-10} to 10^{-12} mV^{-1} . Poisson's ratio is a parameter which indicates relative deformations in the longitudinal and transverse directions. Specifically, it is the ratio of transverse elongation to longitudinal contraction when a pressure is applied to a solid at a constant voltage.

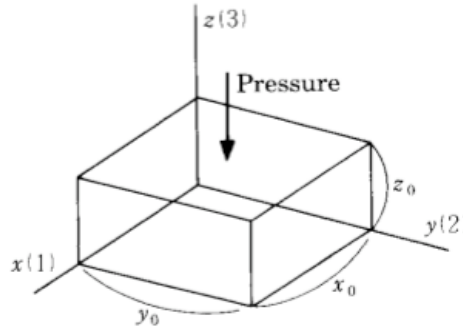


Figure 2.9: Coordinate axes and corresponding subscript numbers.

$$\sigma^E = \frac{S_{31}}{S_{33}}. \quad (2.16)$$

The superscript denotes an unvarying parameter during state changes; thus σ^E is the Poisson's ratio when the applied voltage is constant. Subscripts indicate axis direction for cause and effect. The numbers 1, 2 and 3 correspond to axes x, y and z respectively shown in Figure 2.9. Thus, pressure in the z -direction

creates a strain $\Delta z/z_0$ in the same direction represented by S_{33} . Similarly, S_{31} is the strain in the x -direction caused by pressure in the z -direction.

7. Directionality of Piezoelectric Strain Constant

If deformations are caused by an electric field, Poisson's ratio cannot be used for determining the relative deformations. In this case, the piezoelectric strain constant in the z -direction is usually represented by d_{33} .

$$\frac{\Delta z}{z_0} = d_{33}E_z. \quad (2.17)$$

The elongation in the x -direction is given by d_{31} .

$$\frac{\Delta x}{x_0} = \frac{\Delta y}{y_0} = d_{31}E_z. \quad (2.18)$$

8. Voltage of output coefficients

The reverse piezoelectric effect is formulated as

$$E_z = -g_{33}T_z = -g_{31}T_{x,y}. \quad (2.19)$$

where g is called the voltage output constant (VmN^{-1}) and is related to the strain constant d by the following relationship:

$$g_{33} = d_{33}/\varepsilon_{33}^T. \quad (2.20)$$

$$g_{31} = d_{31}/\varepsilon_{31}^T. \quad (2.21)$$

where ε is the permittivity of the ceramics.

9. *Piezoelectric Coupled Equations*

The following equations represent a characteristic piezoelectric ceramic. They are known as the linear piezoelectric equations and represented using tensor notation. These equations may be represented depending on which variables are selected as independent and dependent. Based on actuation formulation or “Strain-Charge” form, the equations are,

$$S_{ij} = s_{ijkl}^E T_{kl} + d_{ijn} E_n, \quad (2.22)$$

$$D_m = d_{mj} T_j + \epsilon_{mk}^T E_k. \quad (2.23)$$

and based on sensing formulation or “Strain-Field” form”, the equations are,

$$S_i = s_{ij}^D T_j + g_{mi} D_m, \quad (2.24)$$

$$E_k = g_{mj} T_j + \beta_{km}^T D_m. \quad (2.25)$$

where

D - Electric flux density

T - Stress

S - Strain

E - Electric field

Equations 2.22 and 2.24 represent the inverse effect, whereas equations 2.23 and 2.25 represent the direct effect.

10. *Coupling Coefficient (k)*

Electromechanical coupling describes the conversion of energy from mechanical form to electrical form or vice versa. It is represented by the coupling coefficient, k , which is the square root of the ratio between the input and output energy.

$$k = \sqrt{\frac{\text{Mechanical energy stored}}{\text{Electrical energy applied}}} = \sqrt{\frac{\text{Electrical energy stored}}{\text{Mechanical energy applied}}}. \quad (2.26)$$

11. *Voltage –Stress Limits*

If the applied voltage exceeds a certain level, the voltage-strain relationship loses its linearity. In general, the limitation on field strength is typically between 500 V/mm and 1000 V/mm depending on the poling process, the operating temperature and the duration. Figure 2.10 shows the stress-strain relation at the positive and negative voltage limits respectively. The parallelograms show the limits for voltage and force. The theoretical maximum output is obtained when the stress or strain follows the parallelograms perimeter in the plot.

2.3 Ultrasonic Transducers

Piezoelectric materials are commonly used as source of generation of ultrasonic vibrations in transducers. The Langevin transducer was one of the first piezoelectric transducers involving a composite construction [7]. Development of piezoceramics in the early 1950s led to their use in high power transducers. However, the bonded joints of the Langevin construction and fragile nature of these ceramics led to failure.

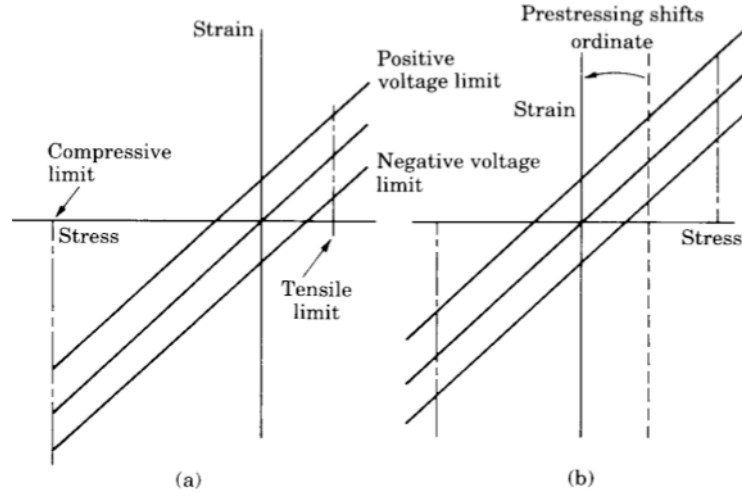


Figure 2.10: Piezoelectric stress vs. strain characteristics (a) without prestressing (b) increase in stress limit with prestressing.

A key development was the prestressed construction introduced by Miller [7]. This concept resolved both difficulties, that of attachment and that of tensile failure.

2.3.1 Ultrasonic Transducer Design

Design of ultrasonic transducers is based on performance characteristics such as frequency, efficiency, acoustic and electrical impedance, power and reliability. A typical piezoelectric ultrasonic transducer is shown in Figure 2.11.

Ultrasonic transducer designs are analyzed using finite element methods to determine the resonant frequency at half wavelength. The mass of the steel backing and the shape of the front mass affect the transducer impedance, axial displacements, stresses and the bolt stress.

Ultrasonic transducers are typically used in series with a half wavelength booster to amplify displacement. The stepped horn is the simplest form of a booster (Figure

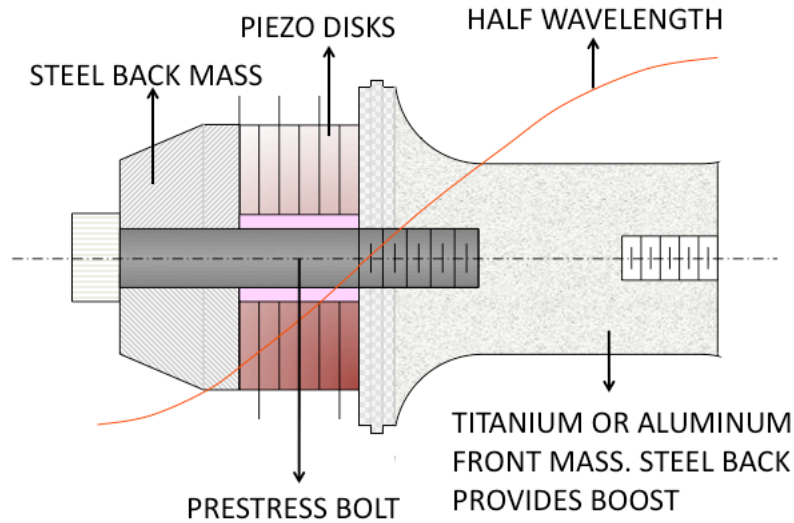


Figure 2.11: Cross section of a high power piezoelectric ultrasonic transducer.

2.12. The most common configuration is where the length of each section in the horn is equal to quarter wavelength. Then, the magnifying factor or booster gain is the ratio of the cross sectional areas at either end.

The Poisson effect causes lateral expansion and contraction during vibration. To obtain uniaxial displacements as far as possible, large horns are slotted to minimize the effect of lateral motion. The placement and thickness of these slots is determined by finite element analysis.

Some of the key design aspects of ultrasonic transducers that have been investigated by researchers are:

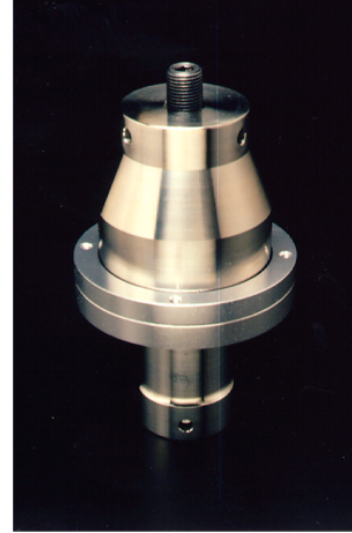
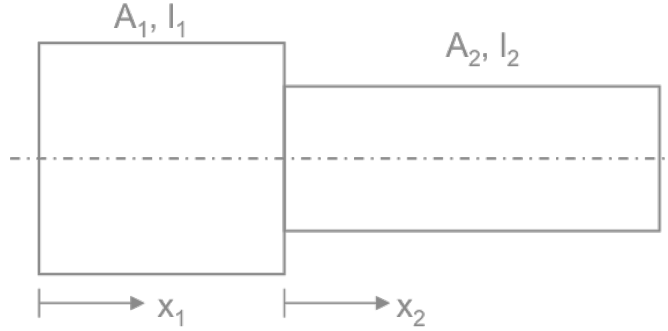


Figure 2.12: (a) Half wavelength stepped horn (b) Commercial booster (*Courtesy: Edison Welding Institute*).

2.3.1.1 Temperature Effects

Heating of the transducer changes the resonant frequency. The temperature effect is important from the standpoint of (1) frequency control systems, and (2) the undesired possibility of excitation of nearby modes. Theory and experiment have shown that expansion of the compression bolt is a major contribution to the lowering of resonant frequency [7].

2.3.1.2 Transducer Efficiency

Measurement of acoustic power and electro-acoustic efficiency of high power ultrasonic transducers has been studied by Lin et al. [16]. The operating efficiency of a transducer depends on the mechanical and electrical loads and losses.

2.3.1.3 Vibration Analysis

Three dimensional vibration effects are important considerations in resonators and transducers. Finite element methods have been applied to the composite design in understanding the mode shapes, temperature effects and the effect of adhesive layer.

2.3.1.4 Ceramic Location

The fundamental design procedure for transducers begins with the placement of the displacement node at the center of the ceramics. This, however, may not always be practical or desirable (Neppiras et al. [21]) The effects of variable ceramic location have been studied by LeMaster et al. [14]. Figure 2.13 shows a family of transducers with different ceramic locations.



Figure 2.13: Family of transducers with variable ceramic location.

2.3.1.5 Machining Finish

The importance of good machining finish at the interface between the ceramic and metal components has been emphasized for good performance characteristics. Due to

high frequency vibrations, significant fatigue and wear occurs at the interface. The heat generation also depends on the machining finish. Thus, it is desirable to have a smooth and fine interfacial finish.

2.3.1.6 Power Source and Frequency Control

Solid-state power amplifiers, involving Silicon Controlled Rectifiers (SCRs) or power transistors are the present day power source for ultrasonic transducers. One widely used approach involves a low level power amplifier, and paralleled power transistors.

Typically, the output impedance of solid state amplifiers is low relative to piezoelectric transducers. This results in the need for an impedance matching network between the power supply and transducer, having both transformer and reactive balancing components.

A number of factors can influence the resonant frequency, such as temperature, voltage or load. It becomes imperative for a means of frequency control.

The modern approach of frequency control is based on driving the transducer with a signal derived from the motion of the transducer. Measurement of this motion may be direct or indirect. Use of strain gages or accelerometers would be direct. Indirect measurement involves in the equivalent circuit of transducers. In this technique, an electrical circuit is used to balance out the electrical part of the transducer, leaving only the “motional” component. The electrical and motional components provide the basis for frequency control.

CHAPTER 3

EXPERIMENTAL WORK

3.1 Experiment #1: Low Load, Low Speed

3.1.1 Objective

This experiment is designed for low loads up to 10 N and low sliding velocities up to 0.068 m/s. It has been reported that tangential ultrasonic vibrations can reduce the average friction force at the interface. There are two primary objectives of this experiment. Firstly, to demonstrate the potential of tangential ultrasonic vibrations in alleviating dry sliding friction by quantifying the percentage reduction in friction force in the presence of ultrasonics. Secondly, to study the effect of load on friction reduction. Most sliding mechanisms in automotive systems see a wide range of loads during their operation. For a given input ultrasonic power, the ability of ultrasonic vibrations in reducing friction has a parametric dependence on load. By quantifying this, the performance envelope of ultrasonic systems is defined.

3.1.2 Design of Ultrasonic Transducer

The ultrasonic transducer employed in this study is designed using a hollow PMN-PT (Lead Magnesium Niobium- Lead Titanate) stack manufactured by EDO Corporation. The stack is placed between two conical waveguides and preloaded by a #6-32

through bolt and Belleville washers. This stack requires an optimum preload of 500-600 N. The ends of the transducer remain the points of contact with the base surface during the experiment. Since the washers are an order of magnitude stiffer than the bolt, most of the stacks displacement is transmitted to the shells.

The operating frequency of the ultrasonic transducer is determined based on the half wavelength mode shape. Th transducer is modeled as a thin free rod performing longitudinal vibrations. The wave equation in a thin rod is given by Equation 2.10 and the vibration modes are given by Equation 2.11.

The natural frequency of the rod corresponding to the first mode shape is given by

$$\omega_0 = \frac{\pi c_0}{l}, f_n = \frac{c_0}{2l}. \quad (3.1)$$

The velocity of wave propagation in PMN-PT, c_0 is calculated as

$$c_0 = \sqrt{\frac{E}{\rho}} \quad (3.2)$$

where \mathbf{E} is the Young's modulus and ρ is the material density.

For PMN-PT, \mathbf{E} is 120 GPa and ρ is 7900 kg/m^3 . Hence the velocity of wave propagation in PMN-PT is approximately 3900 m/s.

The length of the transducer, l is 1.92 inches or 0.04876 m. Thus, the operating frequency in first mode is found to be 40,000 Hz.

Table 3.1 shows the specifications of the transducer. Upon application of a sinusoidal voltage (1 V to 10 V) at an ultrasonic frequency (40 kHz), the transducer vibrates ultrasonically. In the presence of ultrasonic oscillations superimposed on the macroscopic motion of the transducer, a reduction in friction is measured. The

amount of friction reduction depends on the voltage, frequency, preload and the velocity ratio. The velocity ratio is defined as the ratio of the sliding velocity of the transducer (v_{sliding}) to the velocity of the ultrasonic vibrations (v_{vib}).

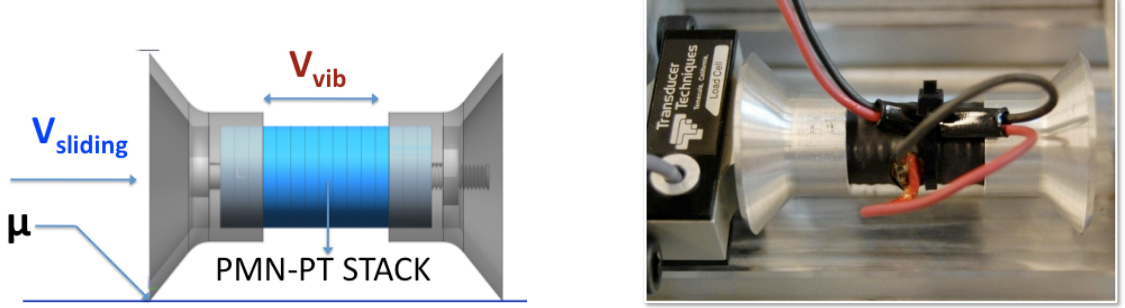


Figure 3.1: PMN-PT stack ultrasonic transducer.

3.1.3 Design of Experimental Setup

An experimental apparatus similar to the one developed by Littmann et al. [18] is designed as shown in Figure 3.2. A pneumatic cylinder pushes an aluminum slider carriage at different velocities. The slider carriage slides on aluminum guide rails. The ultrasonic transducer is attached to the carriage at one end. The ends of the transducer remain in contact with the guide rail surface throughout the test.

An adapter bracket connects one end of the transducer (#6-32 bolt) to the (1/4 - 28) hole of a load cell (MPL-50-T). The load cell measures the average frictional force at the contact interface as the transducer moves. The function of the slider carriage is to transfer motion from the pneumatic actuator to the transducer. The carriage consists of a lever arm designed to apply external load on the transducer. Adjusting the flow of air into the cylinder controls the sliding velocity of the carriage

Table 3.1: Transducer Specifications

Number of discs in stack, n	62
d_{33} of PMN-PT	730×10^{-12} m
Required displacement, ΔL	0.7×10^{-6} m
Voltage (maximum), V_{max}	$\Delta L / (d_{33} \times n) = 15.466$ V
Frequency, f	40 kHz
Preload, F	150 lbs = 670 N
Capacitance, C	300 nF
Current (maximum), I_{max}	$2\pi f C V_{max} = 1.75$ Amps
Impedance, Z	$1/\omega C = 8.84$ Ω
Stiffness of stack, K_{stack}	3.14×10^8 N/m
Stiffness of bolt, K_{bolt}	3.7×10^7 N/m
Deflection in stack due to preload, ΔL_{stack}	$F / K_{stack} = 2.133$ μ m
Nominal displacement of stack, ΔL_0	36 μ m
Maximum displacement possible, ΔL	$\Delta L_0 (K_{stack} / (K_{stack} + K_{bolt})) = 32.2$ μ m

and transducer. For these tests, the voltage/frequency of excitation is set at 6 V peak-to-peak, at 40 kHz. At this frequency, the transducer operates with maximum displacement at its ends. A range of loads (1-10 N) is applied by placing static weights on the lever arm.

The load cell, which measures the average frictional force between the transducer and guide rail, is connected to a signal conditioner to eliminate high frequency noise. Data Physics ACE is used as the data acquisition system. It is set to record data at a frequency span of 80 Hz and block size of 256. The voltage and current driving the piezoelectric stack are monitored. By adjusting the flow valves on the air cylinder, the desired speeds are obtained. The velocity of the transducer (assumed constant) is measured by dividing a known distance by the time taken to traverse it. The velocity

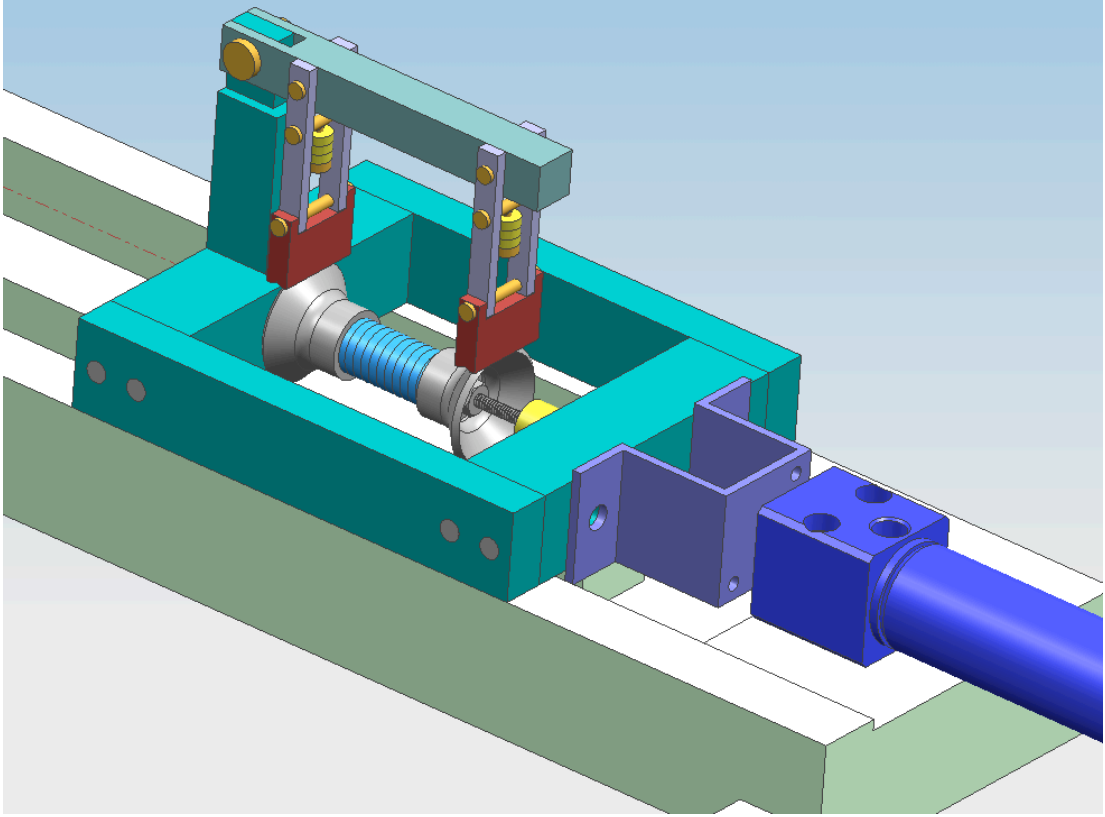


Figure 3.2: Rendering of experimental setup.

of the ultrasonic vibrations is measured using a laser displacement sensor. Figure 3.3 shows the fabricated experimental setup.

3.1.4 Experimental Results

Tests are conducted for two different sliding velocities (0.038 m/s and 0.068 m/s) in order to assess the sensitivity of friction control to velocity ratio. The voltage applied to the stack is 6 V peak-to-peak at constant current amplitude of 2 A peak-to-peak. The frequency of the excitation signal is 40 kHz. The friction force is measured at no load and at loads of 1 N, 2 N, 5 N and 10 N.

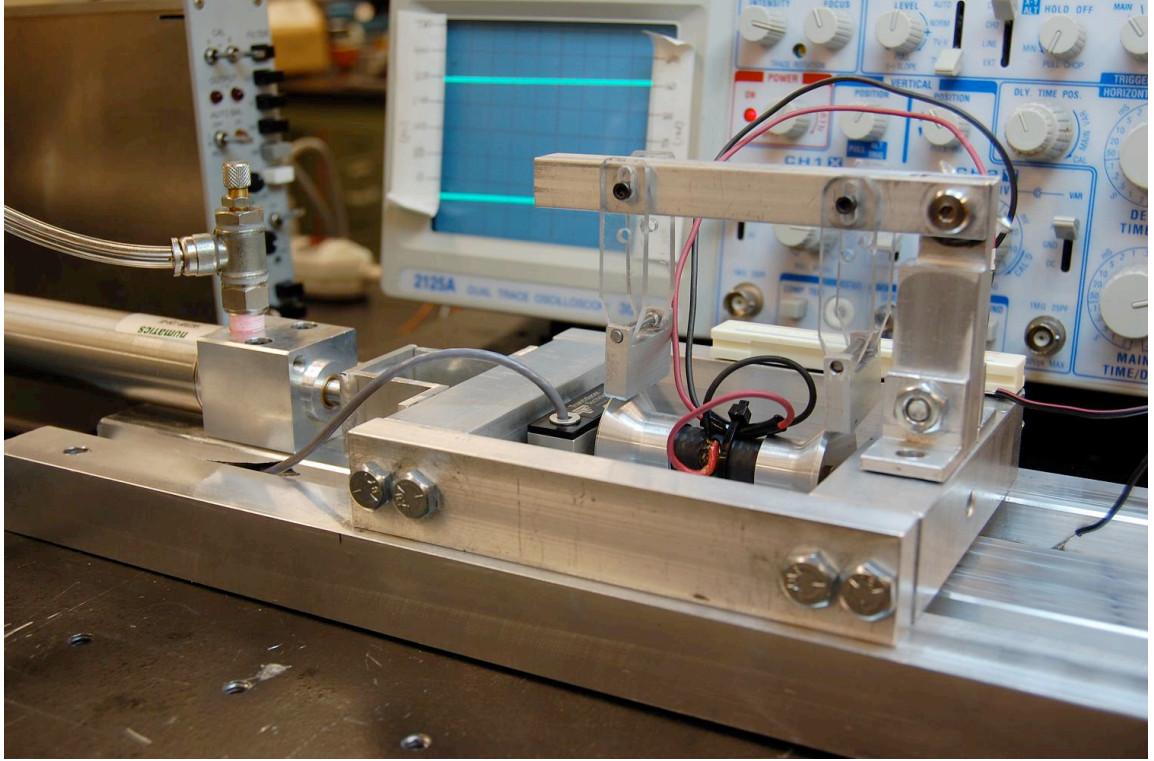


Figure 3.3: Experimental setup for measuring the average frictional force with and without ultrasonic vibrations at various sliding velocities.

Two sets of tests are conducted in order to quantify the effect of friction reduction. First, the actuator is run without the application of any excitation signal (OFF state). Next, the transducer is excited at $t=3$ sec to $t=5$ sec for case 1-low speed, and $t=1.5$ sec to 2.5 sec for case 2-high speed, using an external burst trigger mode (OFF/ON state). The results obtained are shown in Figure 3.4 and Figure 3.5.

3.1.5 Discussion

Friction force in the OFF state is the dry friction between the transducer and guide rails. The load cell initially does not experience any force when the transducer is at rest. Once motion is initiated, there is a compressive force (represented by

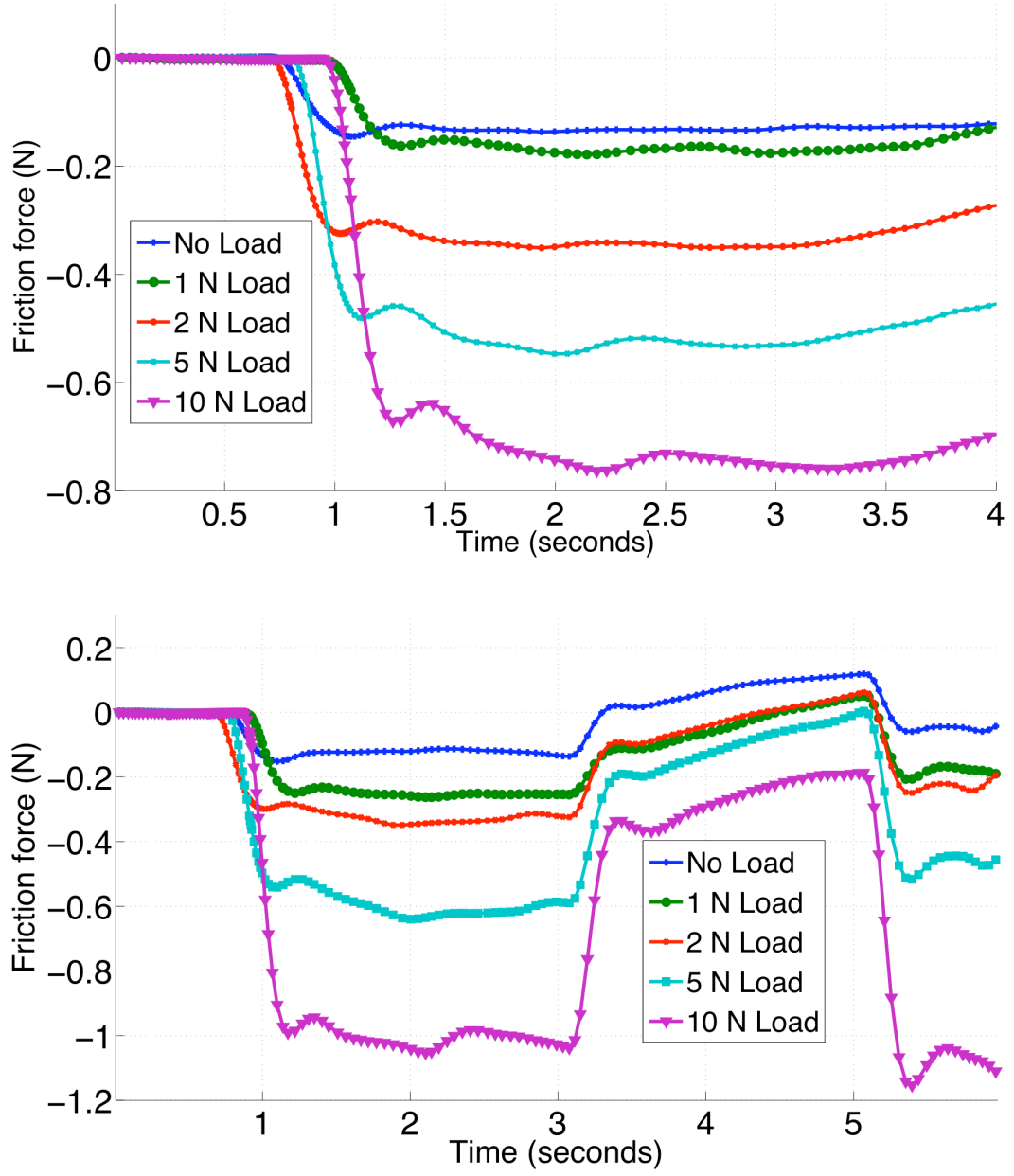


Figure 3.4: Friction force measured at transducer velocity of 0.038 m/s in (a) OFF state and (b) OFF/ON state.

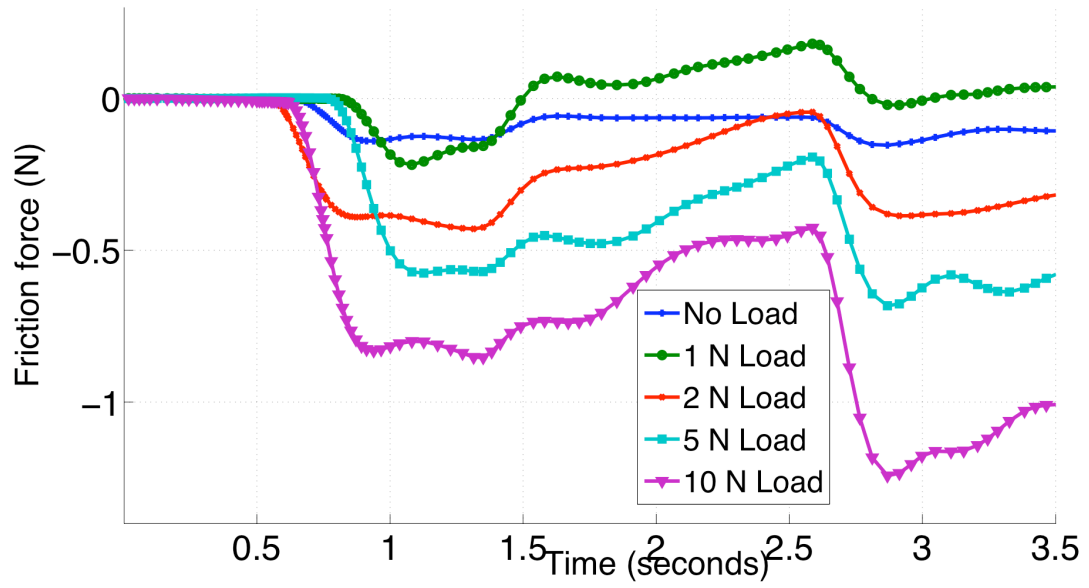
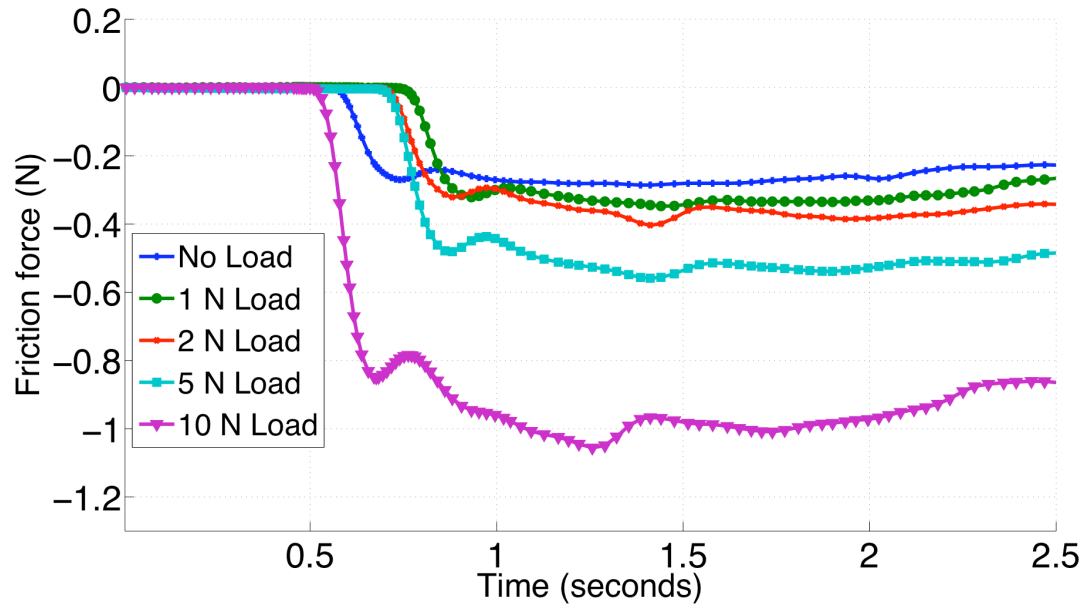


Figure 3.5: Friction force measured at transducer velocity of 0.068 m/s in (a) OFF state and (b) OFF/ON state.

negative sign) on the load cell. This is the static friction force to be overcome to sustain relative motion. The compressive force measured by the load cell thereafter is the kinetic friction force. As the normal reaction ($N=mg$) increases with load (W), the friction force (μmg) also increases.

In the OFF/ON state, i.e., when the PMN-PT stack is energized, ultrasonic vibrations along the direction of motion reduce the friction force at the interface. This creates a decrease in the compressive force on the load cell in Figure 3.4(b) and Figure 3.5(b). This trend is observed at both sliding speeds. However, the extent of reduction is observed to be greater in the case of low speeds. As the velocity ratio (ξ) increases, the effect of friction reduction decreases.

The experimental data at high transducer velocities shows inconsistencies, which are most likely due to fluctuations arising from the experimental setup. The aluminum shells and guide rail abrade during sliding, thus slightly changing the frictional properties after each test run. At high velocities, the assumption of constant transducer velocity may not necessarily hold. Since a pneumatic cylinder is used to drive the transducer, there is a brief period when the cylinder accelerates and reaches a steady-state velocity. Over a short distance, obtaining a constant high velocity is therefore a challenge with this setup.

3.2 Experiment #2: High Load, Low Speed

3.2.1 Objective

In experiment #1, the loads applied are low (up to 10 N) and hence, a low power transducer was sufficient to obtain significant friction reduction. However, in an automotive seat belt system, the maximum load seen by a seat belt during a crash is around 700 N at the interface of the D-ring and seat belt. Experiment #1 confirms that the effect of friction reduction decreases with increasing load and thus there is a need for high power ultrasonics to achieve a similar friction reduction.

Commercial high power ultrasonic welders are available with a capacity of 2.5 kW. Superimposition of out-of-plane normal vibrations on the sliding velocity also results in a reduction in friction force. This phenomenon is different from experiment #1 where the vibrations are superimposed tangential to the sliding velocity.

The objective of experiment #2 is to validate the use of out-of-plane normal vibrations using a Dukane ultrasonic welder for the purpose of friction reduction. These out-of-plane vibrations modulate the normal contact deflection at the interface in a sinusoidal manner about an average value. This reduces the effective area of contact and hence the friction force. The friction force is measured during motion of the seat belt with and without ultrasonic vibrations and the percentage decrease is quantified. By changing the normal load, the effect of load on the friction reduction is determined. Additionally, the duration of the ultrasonics ON time and the amplitude of the vibrations is varied for different tests to understand their effect on friction reduction.

3.2.2 Design of Experimental Setup

The experimental setup shown in Figure 3.6 consists of an automotive seat belt retractor assembly connected to a load cell. The load cell is fixed to a pneumatic cylinder using a connector bracket. The load cell measures the pull force exerted on the belt. The pneumatic cylinder retracts at a steady speed of 0.025 m/s for a distance of 12 inches. The Dukane 220 ultrasonic plastic welder has a 2.5 kW capacity and can generate ultrasonic vibrations up to an amplitude of 85 microns at full power. The operating frequency of the transducer is 20 kHz. It is capable of applying normal loads up to 1500 N on the substrate using pneumatic pressure. The load is calculated by multiplying the air pressure with the area of the cylinder inside the ram. In this experiment, with a pressure of 60 psi, a normal load up to 670 N is applied. The double acting pneumatic cylinder is controlled using a mechanical toggle switch. The maximum load is limited by the force generated by the pneumatic cylinder to pull the belt and sustain steady state motion. Table 3.2 shows specifications of the Dukane ultrasonic transducer.

Table 3.2: Dukane Ultrasonic Transducer Specifications

Operating frequency, f	20,000 Hz
Maximum normal load	1500 N
Power	2.5 kW
Horn material	Heat treated steel
Maximum amplitude	85 microns
Half wavelength	5 inches
Air pressure for pneumatic cylinder	14-45 psi

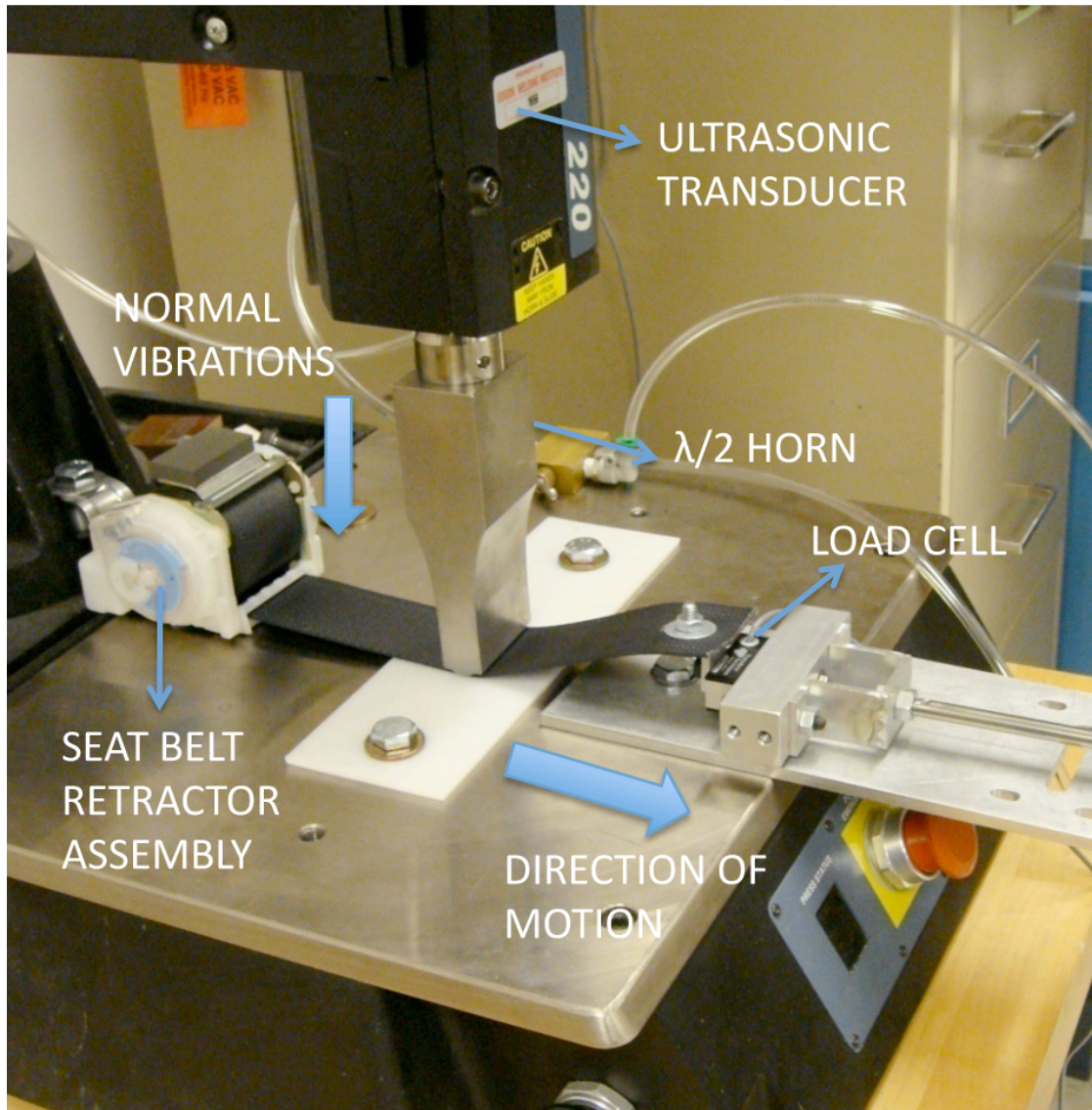


Figure 3.6: Experimental setup.

3.2.3 Experimental Results

The following four set of tests are conducted and results are recorded:

1. Friction force in the OFF state at different loads
2. Friction force in the OFF/ON state with different durations of ON time
3. Friction force in the OFF/ON state at different loads
4. Friction force in the OFF/ON state at different vibration amplitudes

3.2.3.1 Effect of Duration of Ultrasonics ON Time

It is possible to delay the generation of vibrations using the Dukane ultrasonic transducer. The duration of the ON time can be set depending on the application. In this experiment, the ultrasonic ON time is set at 0.5, 1, 2, and 2.5 seconds. During this ON time, friction reduction is observed at the interface.

However, a prolonged duration of ultrasonic energy may not be necessarily beneficial. The maximum possible friction reduction depends on the velocity of the belt , load and coefficient of friction. Further energy supplied into the belt will not result in friction reduction . Thus, duration is a key parameter to be determined based on the normal load and belt velocity. Figure 3.7 shows the effect of duration of the ultrasonics ON time on the extent of friction reduction.

It is found that for 0.5 and 1 second of ON time, the friction force does not bottom out. Further increase in duration to 2 seconds results in a 58% reduction in friction force. Additional increase in duration does not cause any further significant reduction. One of the key concerns while using these ultrasonic transducers at high loads is the possibility of plastic welding. In the event of the belt ceasing to move,

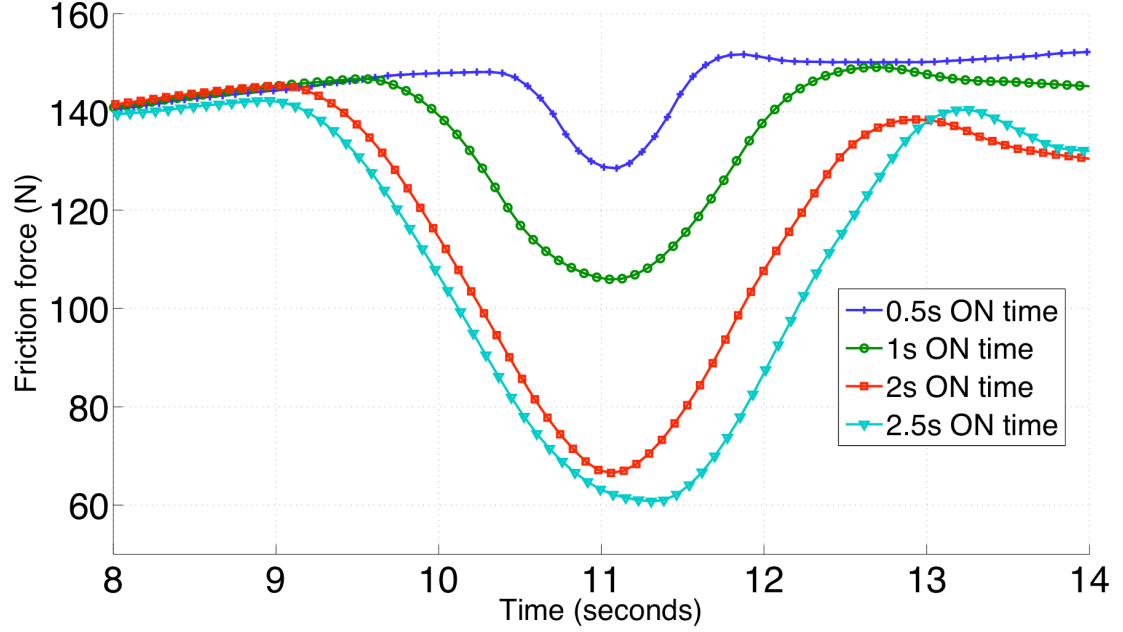


Figure 3.7: Effect of duration of ultrasonics ON time on friction reduction.

the energy from the transducer is sufficient to weld the belt to the substrate, since the belt is made of nylon polymer. Hence it is critical to ensure that the belt is in motion all the time.

3.2.3.2 Effect of Load at Different Amplitudes

Three different load values are selected: 270 N, 450 N and 670 N. Since the belt is held between the ultrasonic horn and the base, initial application of normal load prevents the motion of the belt. To maintain belt velocity, the air pressure into the pneumatic cylinder is adjusted. At all loads, in the OFF state, the pressure is adjusted so that the belt moves at 0.025 m/s. Figure 3.8 shows the friction force at different loads in the OFF state.

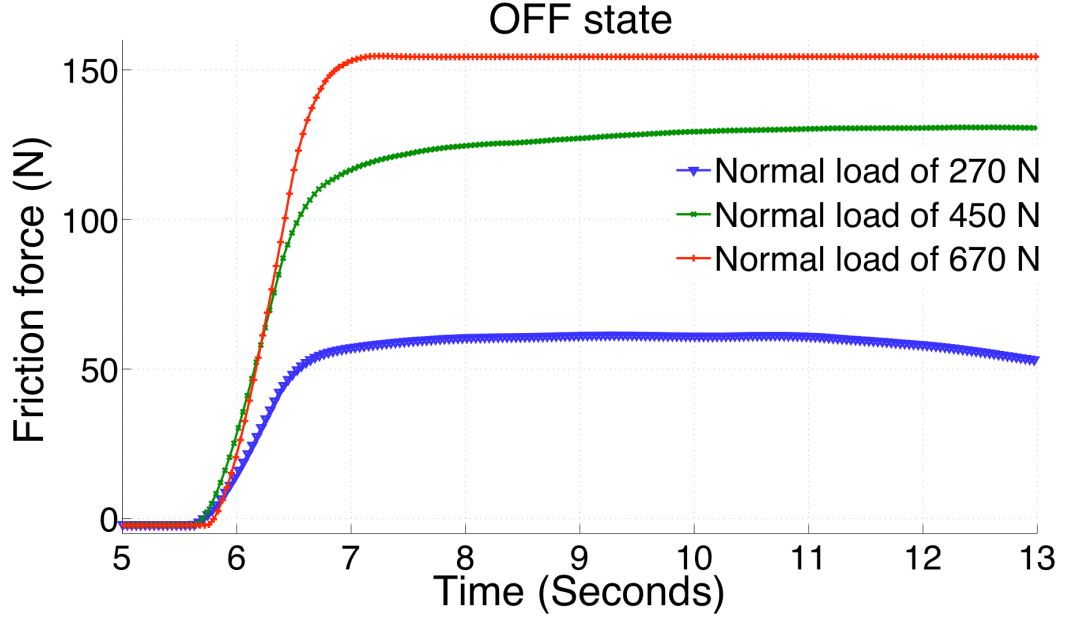


Figure 3.8: Effect of load on friction force in the OFF state.

Flow valves restrict the air flow into the cylinder and as a result, there is a delay due to the air filling time. This is resolved by removing the valves and controlling the air pressure at the source. With a steady state motion in the OFF state, ultrasonic vibrations are now applied at two different amplitudes - 50% and 70% of the maximum 85 microns. The amplitude corresponds to the ultrasonic energy fed into the system.

From Figure 3.9 and Figure 3.10, it is found that the extent of friction reduction decreases with an increase in load. This is expected since higher energy is required to overcome the friction force with the same input energy. Thus, at high loads, higher amplitudes are required to obtain the same extent of friction reduction.

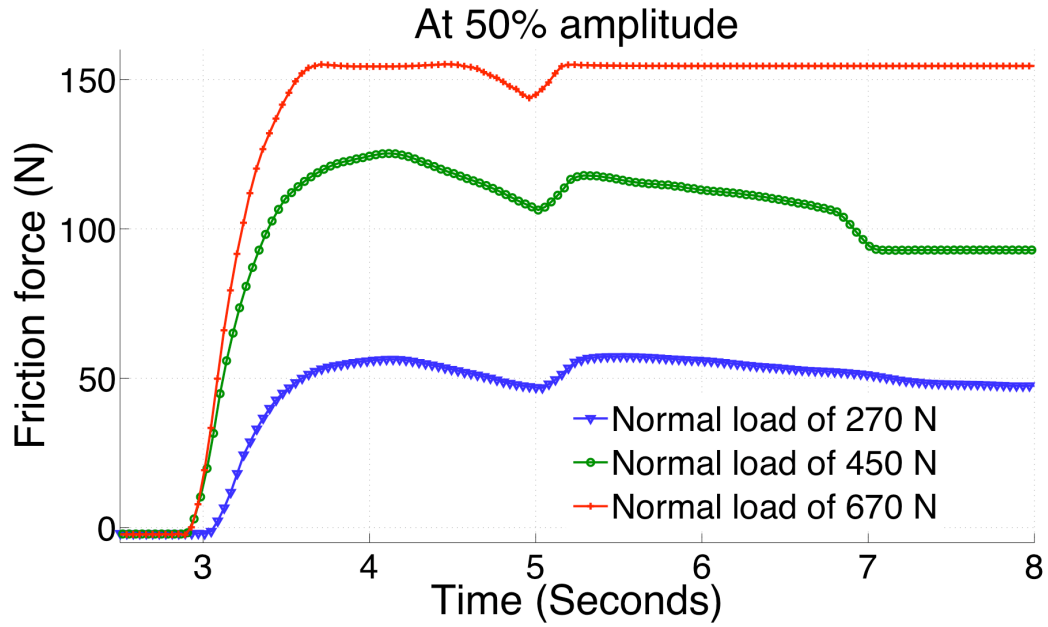


Figure 3.9: Effect of load on friction reduction at 50% amplitude.

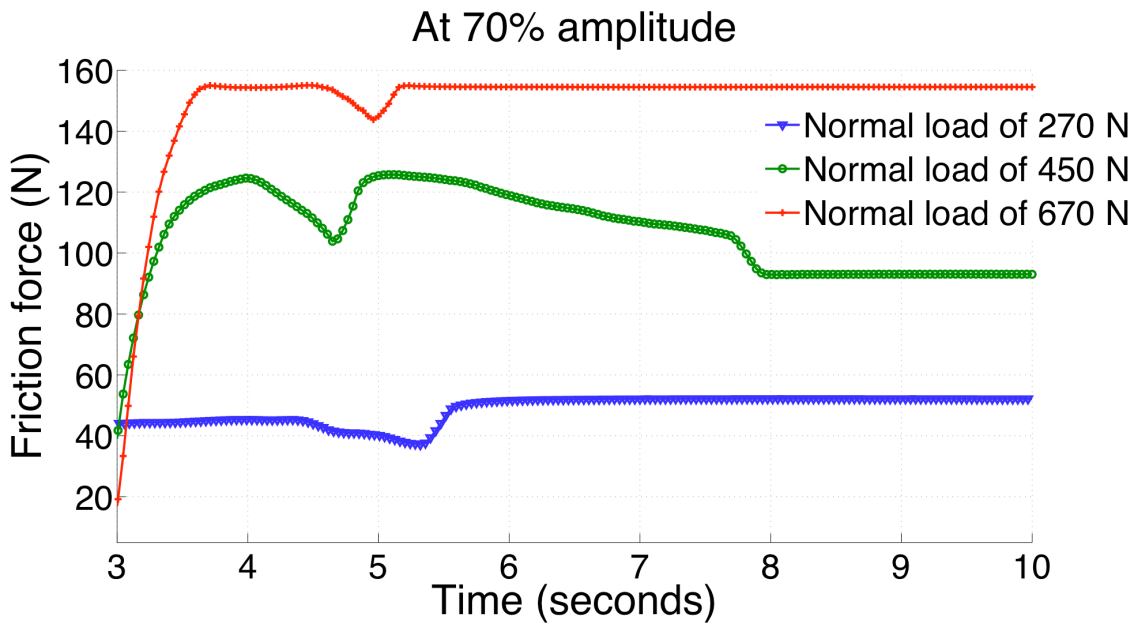


Figure 3.10: Effect of load on friction reduction at 70% amplitude.

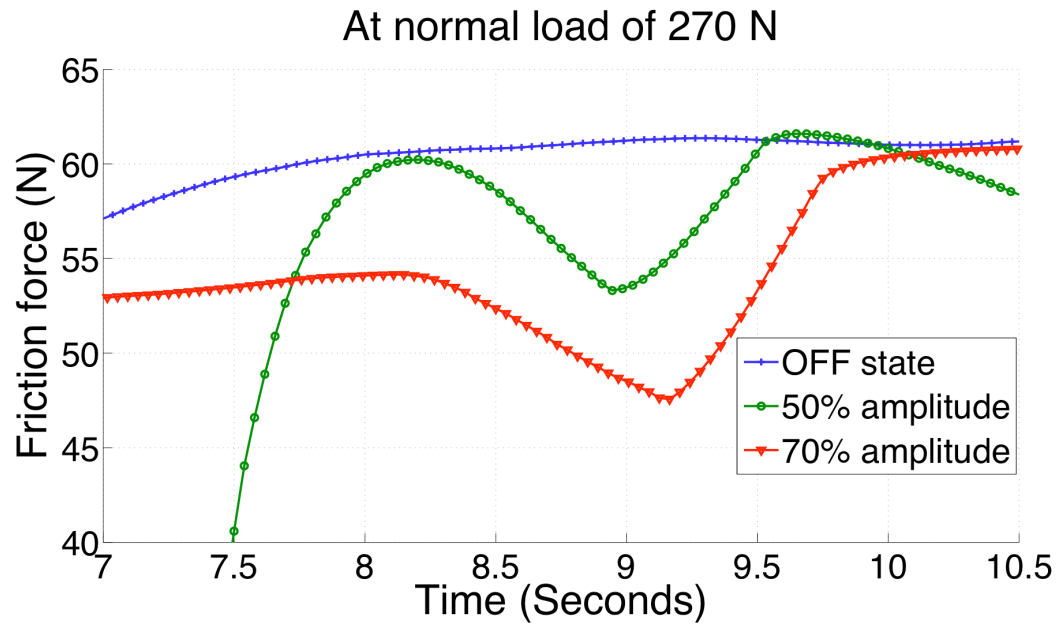


Figure 3.11: Effect of vibration amplitude on friction reduction at 270 N.

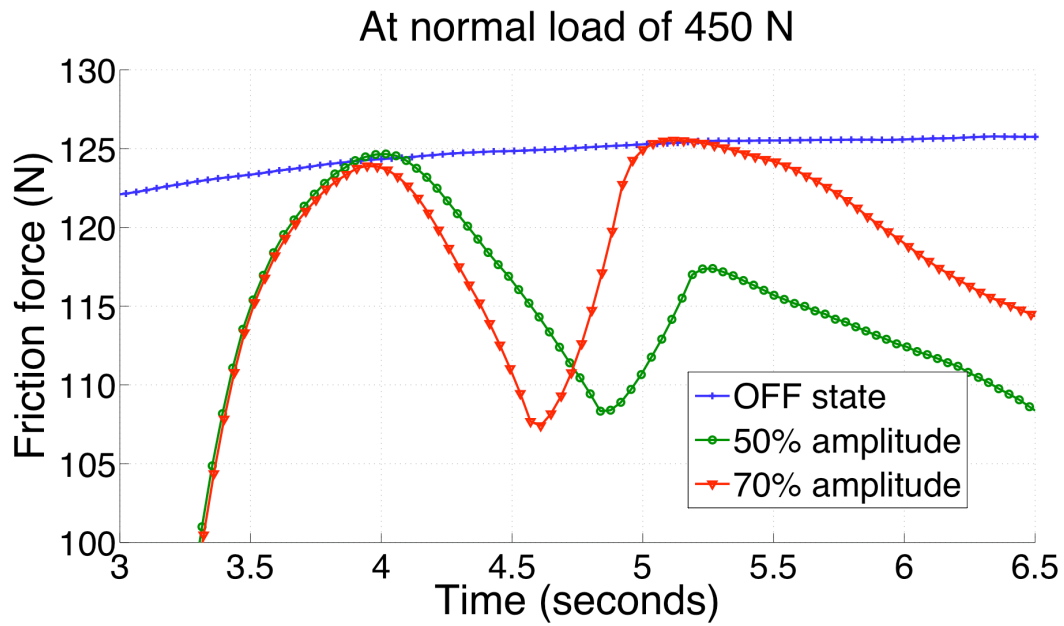


Figure 3.12: Effect of vibration amplitude on friction reduction at 450 N.

3.2.3.3 Effect of Vibration Amplitude at Different Loads

In Figure 3.11 and Figure 3.12, it is evident that higher amplitudes of vibration result in higher friction reduction. At 270 N normal load, the percentage reduction in friction is higher at 70% amplitude than at 50% amplitude. However, as the normal load is increased to 450 N, there is no significant change in the friction force between the 50% and 70% vibration amplitude states. This implies that at higher loads, higher ultrasonic energy is required to obtain friction reduction. These results conform with results from experiment #1 where the effect of friction reduction decreases with increasing normal load.

3.2.4 Discussion

This experiment demonstrates the application of out-of-plane normal vibrations in active friction reduction. In this setup, the limited stroke of 12 inches for the pneumatic actuator. There is a finite time lag between the time of trigger and ultrasonics activation. The constant sliding velocity can be assumed only at a constant normal load and pneumatic pressure. However, in the presence of ultrasonic vibrations, the friction at the interface reduces which in turns accelerates the belt. The inertia due to pneumatics is significant in this setup. The friction does not drop to its reduced value instantaneously but gradually reaches the “lubricated” state. The obtained friction reduction is not the maximum possible reduction. The belt velocity is maintained low in these tests (0.025 m/s) to allow sufficient time for data acquisition. There is a need for a continuous setup to eliminate delays due to inertial effects and allow steady state data acquisition.

CHAPTER 4

ANALYTICAL MODELING

4.1 Friction Models

4.1.1 Coulomb Model

Classical models of friction consist of different components, each of which address certain properties of the friction force. With the assumption that friction is independent of the velocity and area of contact, it is described as,

$$F = F_T \text{sgn}(V), \quad (4.1)$$

where F_T is proportional to the normal load i.e. $F_T = \mu F_N$. This static model is known as Coulomb friction (Figure 4.1). The Coulomb model however does not specify the friction force at zero velocity. Stiction or static friction describes the frictional force at rest. This force is higher than the Coulomb friction level. Static friction counteracts external forces below a certain level and prevents an object from moving.

In [17], [18] and [25] and , the Coulomb friction model has been used to define the friction force, and analytical expressions relating the friction reduction ratio with the

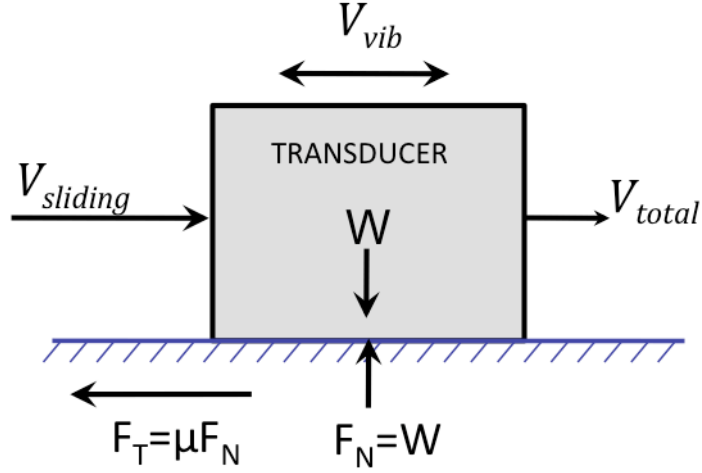


Figure 4.1: Coulomb friction model.

velocity ratio have been presented. In Figure 4.1, the total velocity, \mathbf{V}_{total} is given by

$$V_{total} = V_{sliding} + V_{vib} \cos \omega t \quad (4.2)$$

where $V_{sliding}$ is the sliding velocity and V_{vib} is the velocity of vibration.

The instantaneous friction force given by Equation 4.1 is

$$F = F_T \operatorname{sgn}(V_{sliding} + V_{vib} \cos \omega t), \quad (4.3)$$

The percentage reduction in friction using the Coulomb model is independent of all system parameters such as mass, stiffness, coefficient of friction, tangential contact stiffness and frequency of excitation. It solely depends on the velocity ratio- the ratio of the sliding velocity to the vibration velocity.

4.1.2 Dahl Model

Representation of the discontinuity at zero slip velocity has been a concern, since a real-life physical friction process is continuous. To address this issue, more involved and complex models have been proposed. A micro-slip model such as the Iwan model [12] considers the Coulomb friction element connected to a spring. When the force in the spring reaches a magnitude, it reverses direction. However, such models have not been able to differentiate between the static and kinetic friction coefficients. More sophisticated friction models classified as state variable friction laws use differential equations to describe the friction force. These models are hysteretic in nature and have internal dynamics. Dahl friction is one such example [4]. In the Dahl model, the contact asperities are modeled as micro-springs. The effective contact stiffness is taken into consideration, and the product of the stiffness and the elastic displacement of the asperities gives rise to the friction force (Figure 4.2).

According to Dahls model, the total displacement \mathbf{x} of the rigid body can be broken down-an elastic \mathbf{z} and plastic \mathbf{w} component,

$$\mathbf{x} = \mathbf{z} + \mathbf{w}. \quad (4.4)$$

The elastic component is related to the elastic deflections of the asperities in the tangential direction. The friction force \mathbf{F}_D is then given by,

$$\mathbf{F}_D = \mathbf{K}_t \mathbf{z}, \quad (4.5)$$

in which \mathbf{K}_t is the tangential contact stiffness.

The deflection is described with a differential equation,

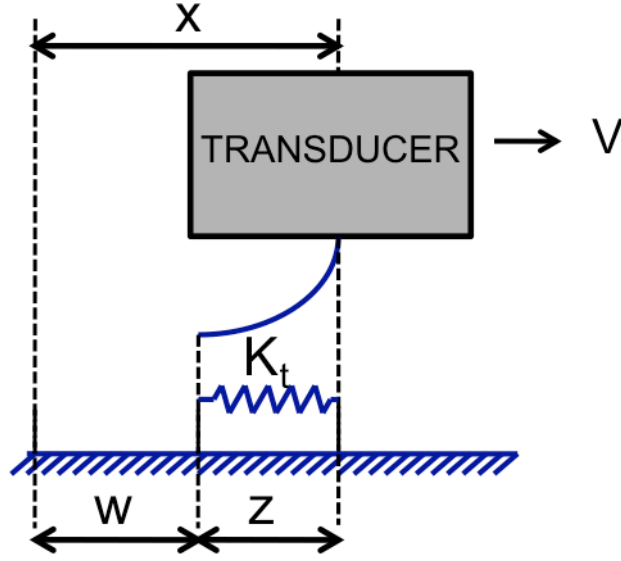


Figure 4.2: Dahl friction model.

$$\frac{dz}{dt} = V[1 - \frac{K_t z}{\mu mg} \text{sgn}(V)]^\alpha. \quad (4.6)$$

Here, α is a parameter that defines the shape of a curve describing the dependence of the tangential deflections. For brittle materials, $\alpha < 1$ and for ductile materials, α is ≥ 1 [27]. α is assumed to be unity.

Correlation between theoretical and experimental results reveal that there is dependence on the contact stiffness at the interface [15],[27]. Using numerical analysis [15], it was shown that Dahl friction can better explain the experimental results. It was suggested that the tangential contact stiffness be considered in analysis.

4.1.3 LuGre Model

Researchers at the Lund Institute of Technology, Sweden, and the University of Grenoble, France developed the LuGre friction model [22]. Here, the contact asperities are modeled as bristles that deflect like a spring when subject to a tangential force (Figure 4.3). This model incorporates the phenomenon that the surfaces are pushed apart by the lubricant, and models the Stribeck effect [26]. This model includes many of the observed features of frictional behavior in experiments.

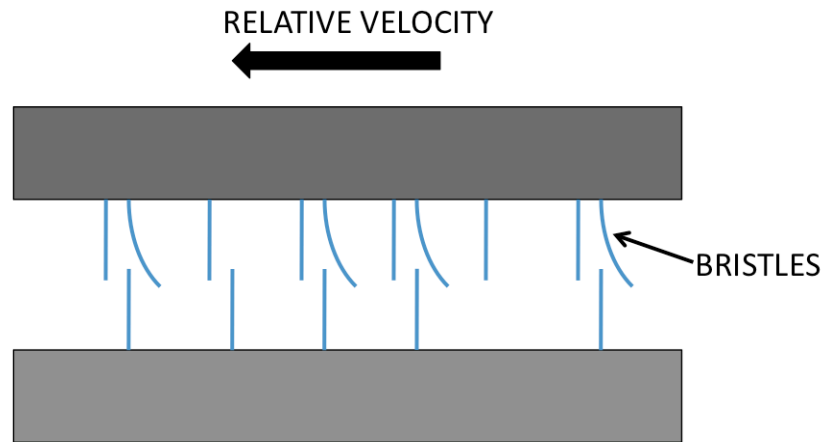


Figure 4.3: LuGre friction model.

The LuGre friction model is used to represent the friction force at the sliding interface. LuGre friction is based on representing the contact interface as spring-like bristles. The deflection in the springs gives rise to the friction force.

Although the deflections of each bristle are random and different, the average deflection, \mathbf{Z} , is defined by a first order differential equation:

$$\dot{\mathbf{Z}} = \mathbf{V} - \frac{|\mathbf{V}|}{\mathbf{G}(\mathbf{V})}\mathbf{Z}, \quad (4.7)$$

where \mathbf{V} is the relative velocity. The first term gives a deflection that is proportional to the integral of the relative velocity. The second term implies that the deflection \mathbf{Z} approaches the steady state value:

$$\mathbf{Z}_{ss} = \frac{\mathbf{V}}{|\mathbf{V}|}\mathbf{G}(\mathbf{V}) = \mathbf{G}(\mathbf{V})\text{sgn}(\mathbf{V}), \quad (4.8)$$

i.e. when \mathbf{V} is constant. The function $\mathbf{G}(\mathbf{V})$ is a positive function defined as,

$$\mathbf{G}(\mathbf{V}) = \frac{1}{\mathbf{K}_t}\{\mathbf{F}_c + (\mathbf{F}_s - \mathbf{F}_c)e^{-(\mathbf{V}/\mathbf{V}_s)^2}\}, \quad (4.9)$$

where \mathbf{K}_t is the tangential stiffness of the bristles, \mathbf{F}_s is the static friction force, \mathbf{F}_c is the kinetic friction force, and \mathbf{V}_s is the Stribeck velocity.

The LuGre friction is given by,

$$\mathbf{F}_L(\mathbf{V}, \mathbf{Z}) = \mathbf{K}_t\mathbf{Z} + \sigma_1\dot{\mathbf{Z}} + \sigma_2\mathbf{V}, \quad (4.10)$$

where σ_1 is the damping coefficient and σ_2 accounts for viscous friction.

For piezoelectrically driven systems at low velocities, viscous friction and the Stribeck effect can be ignored. Then, the LuGre friction reduces to

$$\mathbf{F}_L(\mathbf{V}, \mathbf{Z}) = \mathbf{K}_t\mathbf{Z}. \quad (4.11)$$

$$\dot{\mathbf{F}}_L(\mathbf{V}, \mathbf{Z}) = \mathbf{K}_t\{\mathbf{V} - \frac{|\mathbf{V}|}{\mathbf{G}(\mathbf{V})}\mathbf{Z}\}. \quad (4.12)$$

Since the Stribeck velocity is very small compared to the relative velocity, the function $\mathbf{G}(\mathbf{V})$ reduces to $\mathbf{F}_c / \mathbf{K}_t$. Thus, the LuGre friction becomes

$$\dot{\mathbf{F}}_L(\mathbf{V}, \mathbf{Z}) = \mathbf{K}_t \mathbf{V} \left\{ 1 - \frac{\text{sgn}(\mathbf{V})}{\mathbf{F}_c} \mathbf{F}_L \right\} = \mathbf{F}_D. \quad (4.13)$$

Hence, the LuGre friction reduces to the Dahl friction in the absence of internal damping and Stribeck effect.

4.2 System Model

Assuming that internal damping and viscous friction are negligible, the LuGre friction can be simplified to Dahl friction. This assumption is justified since damping is minimal in piezoelectric systems typically utilized in ultrasonic transduction. Additionally, since the range of displacements is very small, viscous friction does not affect the system dynamics. Thus, the ultrasonic transducer can be modeled as a single degree-of-freedom system with Dahl friction acting at the sliding interface and subjected to a harmonic excitation, as shown in Figure 4.4.

The governing equations of motion for the SDOF model and Dahl friction are given by:

$$\mathbf{m}\ddot{\mathbf{x}} + \mathbf{K}_s \mathbf{x} = \mathbf{F}_e \cos \omega t - \mathbf{F}_D(\mathbf{t}), \quad (4.14)$$

where \mathbf{m} is the mass of the sliding body, \mathbf{K}_s is the system stiffness, \mathbf{F}_e is the piezo control force generated due to an applied voltage and, ω is the excitation frequency.

\mathbf{F}_D is the Dahl friction force given by

$$\dot{\mathbf{F}}_D(\mathbf{t}) = \mathbf{K}_t \mathbf{V}(\mathbf{t}) \left\{ 1 - \frac{\text{sgn}(\mathbf{V}(\mathbf{t}))}{\mu \mathbf{m} \mathbf{g}} \mathbf{F}_D(\mathbf{t}) \right\}, \quad (4.15)$$

where \mathbf{K}_t is the tangential contact stiffness and, μ is the coefficient of friction.

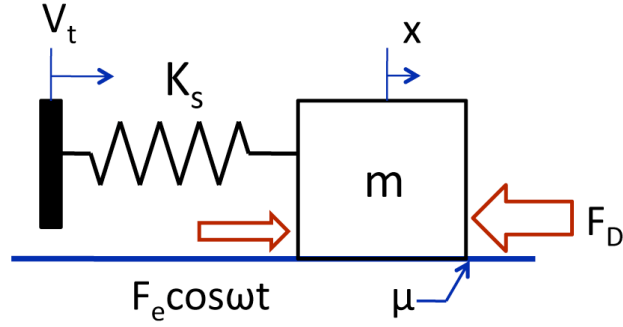


Figure 4.4: Single degree-of-freedom model of ultrasonic transducer.

Since \mathbf{V} is the relative velocity and is equal to $\mathbf{V}_t - \dot{\mathbf{x}}$, equation 4.15 may be written as,

$$\dot{\mathbf{F}}_D(t) = \mathbf{K}_t(\mathbf{V}_t - \dot{\mathbf{x}}) \left\{ 1 - \frac{\text{sgn}(\mathbf{V}_t - \dot{\mathbf{x}})}{\mu \mathbf{m} \mathbf{g}} \mathbf{F}_D(t) \right\}. \quad (4.16)$$

The frictional force is solved for, by numerical integration using the explicit fixed time step solver, fourth order Runge-Kutta method. The nonlinearity due to the signum function entails piecewise integration. Figure 4.5 shows the Simulink block diagram.

This SDOF model, commonly known as the mass-on-a-moving-belt problem, is prone to friction induced self-excited oscillations [19]. This effect is evident in many mechanical systems, and is called “chatter” in servomechanisms. These oscillations give rise to undesirable noise and vibrations. By adjusting the ratio of the excitation frequency to the natural frequency, such systems may be made free from these friction induced oscillations and instability [19] .

One of the objectives of this research is to design an optimal ultrasonic lubrication system. The extent of friction reduction depends on a number of parameters. By determining this parametric dependence of friction, the effectiveness of such ultrasonic systems can be improved.

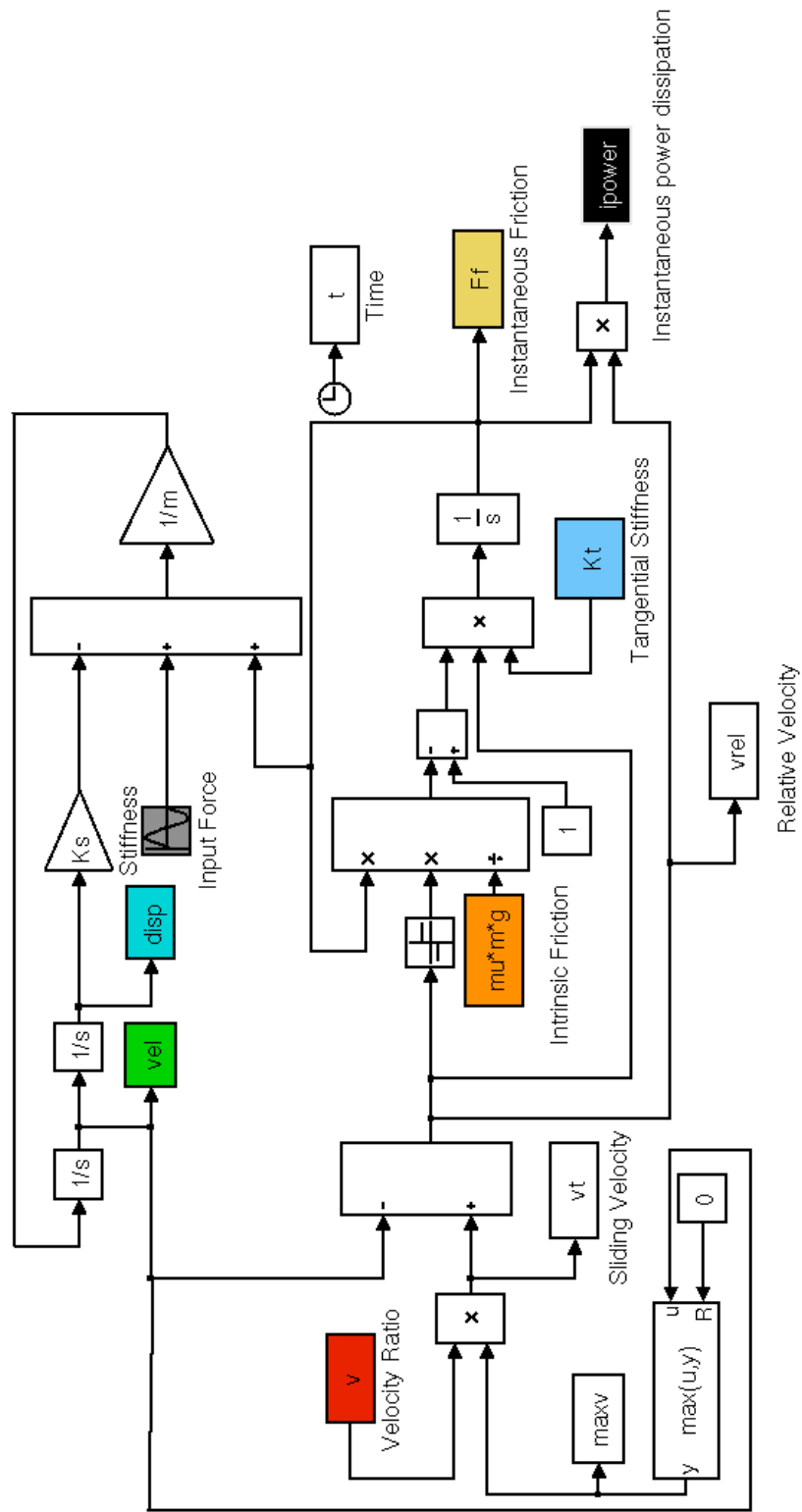


Figure 4.5: Simulink block diagram for system model with LuGre Friction.

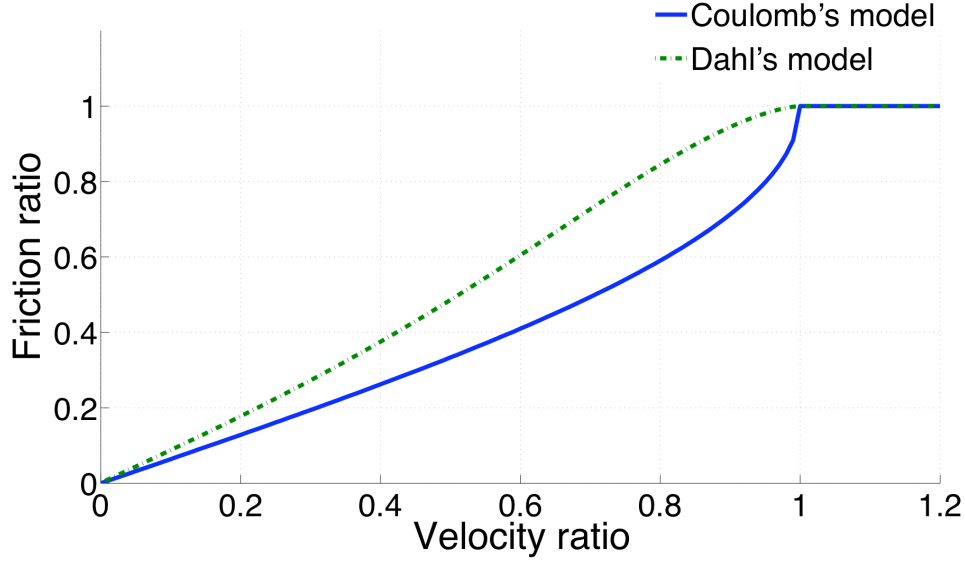


Figure 4.6: Comparison of Coulomb and Dahl model-Friction ratio versus velocity ratio.

4.3 Simulation Results

To characterize the friction reduction, two dimensionless ratios, namely friction ratio and power dissipation ratio, are plotted as a function of the velocity ratio. Friction ratio is defined as the ratio of the friction force in the presence of ultrasonic vibrations to the friction force in the absence of ultrasonic vibrations. Power dissipation ratio is the ratio of the power dissipated due to friction in the presence of ultrasonic vibrations to the power dissipated due to friction in the absence of ultrasonic vibrations. Velocity ratio is defined as the ratio of the sliding velocity to the velocity of the ultrasonic vibrations.

$$\text{Friction ratio} = \frac{\text{Frictional force with ultrasonics}}{\text{Frictional force without ultrasonics}}. \quad (4.17)$$

Table 4.1: Simulation Parameters

Parameter	Value
Mass, \mathbf{m}	0.02 kg
System stiffness, \mathbf{K}_s	133×10^6 N/m
Excitation frequency, ω	$2\pi \times 60,000$ rad/s
Piezo control force, \mathbf{F}_e	0 to 1920 N
Tangential stiffness of bristles, \mathbf{K}_t	0.056×10^6 N/m
Coefficient of friction, μ	0.1
Solver	Fourth order Runge – Kutta method
Time step size	1.667×10^{-8} s (Fixed)

$$\text{Power dissipation ratio} = \frac{\text{Frictional power dissipated with ultrasonics}}{\text{Frictional power dissipated without ultrasonics}}. \quad (4.18)$$

$$\text{Velocity ratio} = \frac{\text{Velocity of sliding}}{\text{Velocity of ultrasonic vibrations}}. \quad (4.19)$$

Table 4.1 shows values for the system parameters used in these simulations.

Plotting friction ratio versus velocity ratio using Coulomb and Dahl equations, without taking into account the system dynamics, it is found that the Coulomb model shows a higher percentage reduction in friction compared to the Dahl model (Figure 4.6).

In addition to the velocity ratio, the percentage reduction according to Dahl's model depends on the mass, coefficient of friction, and tangential stiffness. In Coulomb's model, the instantaneous friction force is discontinuous and has a pulse-like waveform.

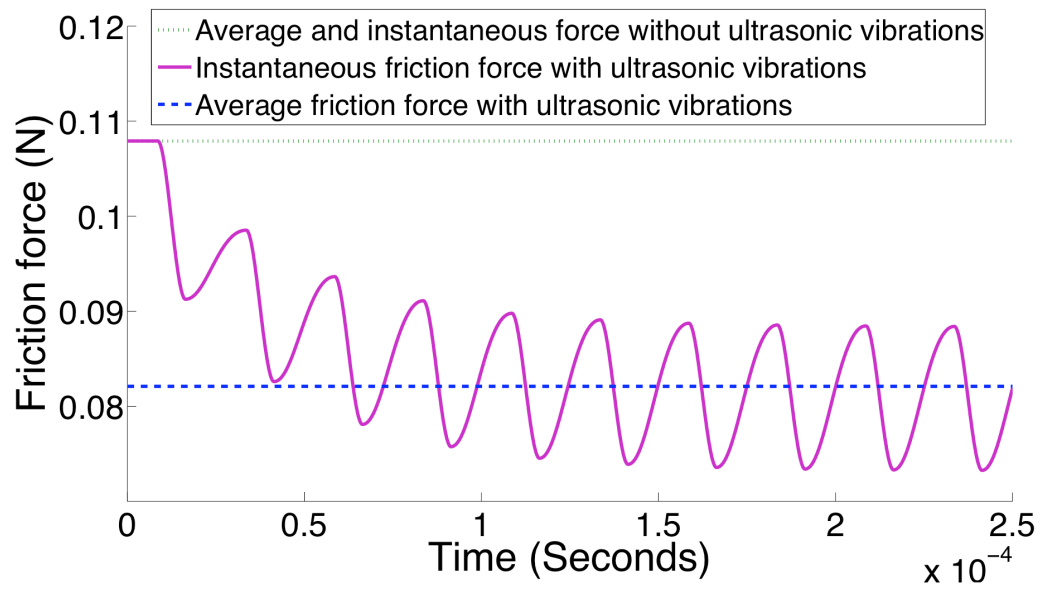
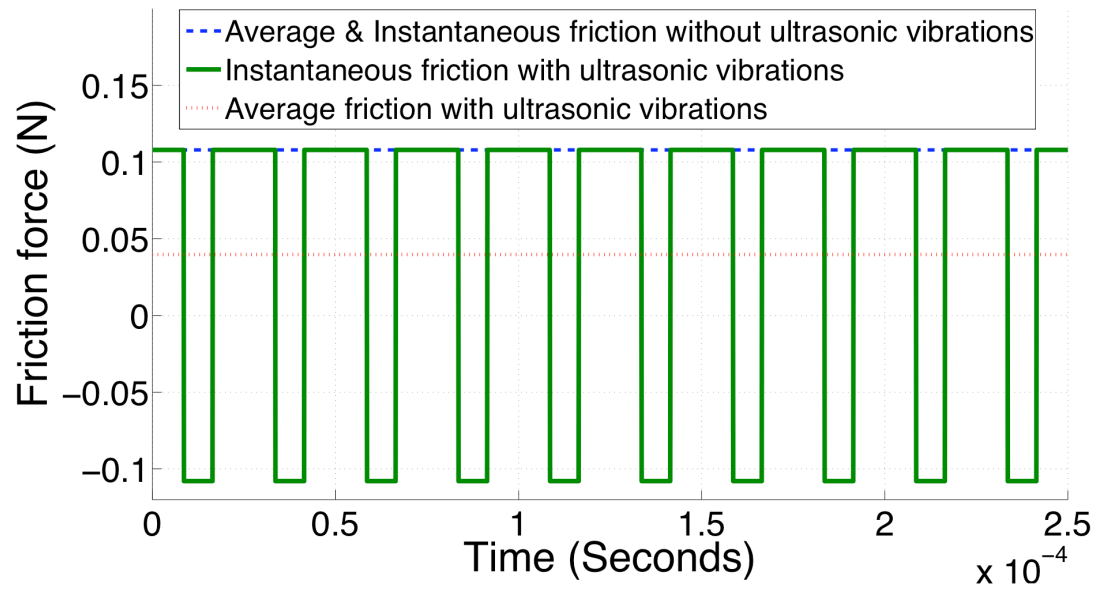


Figure 4.7: Instantaneous friction force vs. time using (a) Coulomb model (b) Dahl model.

In the case of Dahl's model, the force is a continuous function and oscillatory as seen in Figure 4.7.

4.3.1 Time and Frequency Domain Plots

At a velocity ratio of 0.5, piezo control force of 384 N and excitation 60 kHz, simulations are performed. Time domain plots of displacement, velocity, instantaneous friction force, and instantaneous power dissipated are shown in Figure 4.8 and Figure 4.9.

Stability analysis for such systems using the Stribeck and decreasing friction laws has been reported [19]. The displacement, velocity and friction force gradually decrease with time and tends towards a steady state value. Although the peak displacement and velocity decreases, the average displacement and velocity remains the same. From Figure 4.8, it is seen that the displacement and velocity are not sinusoidal, despite a harmonic excitation. This is because there are two frequency components. One component corresponds to the excitation frequency and the other component corresponds to the natural frequency of the system, ω_n , given by $\sqrt{k_s/m}$. As a result, the resultant displacement or velocity may be written as a sum of two frequency components. This is evident from Figure 4.10(a) which shows the Fast Fourier Transform (FFT) plot of the velocity. Thus, analytical models by Coulomb and Dahl which model the vibration velocity as a single sinusoid, do not incorporate the effect of the system's natural frequency. Due to the nonlinearity in the friction force, a number of peaks are exhibited in the FFT. In Figure 4.10(b), the FFT of friction force shows a number of frequency components, which arise from individual harmonics as well as harmonics of the sum and difference of the two frequencies. For systems driving low

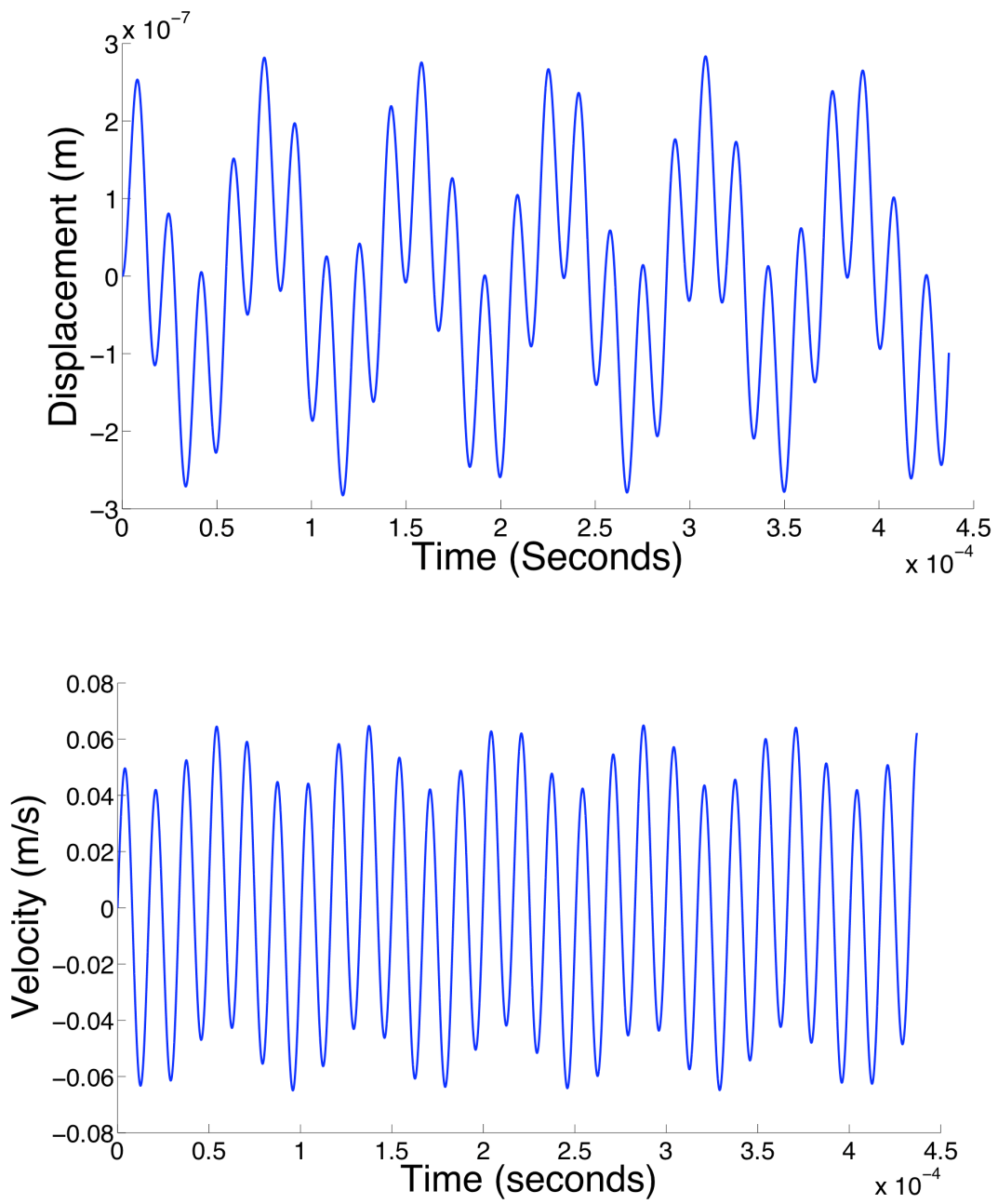


Figure 4.8: (a) Displacement vs. time (b) Velocity vs. time.

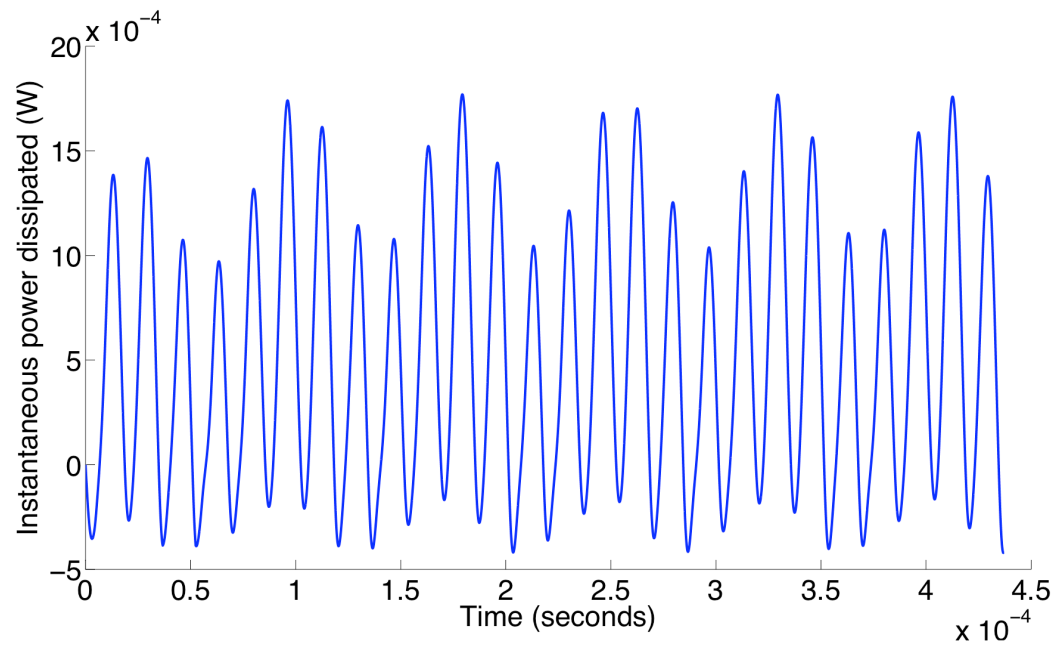
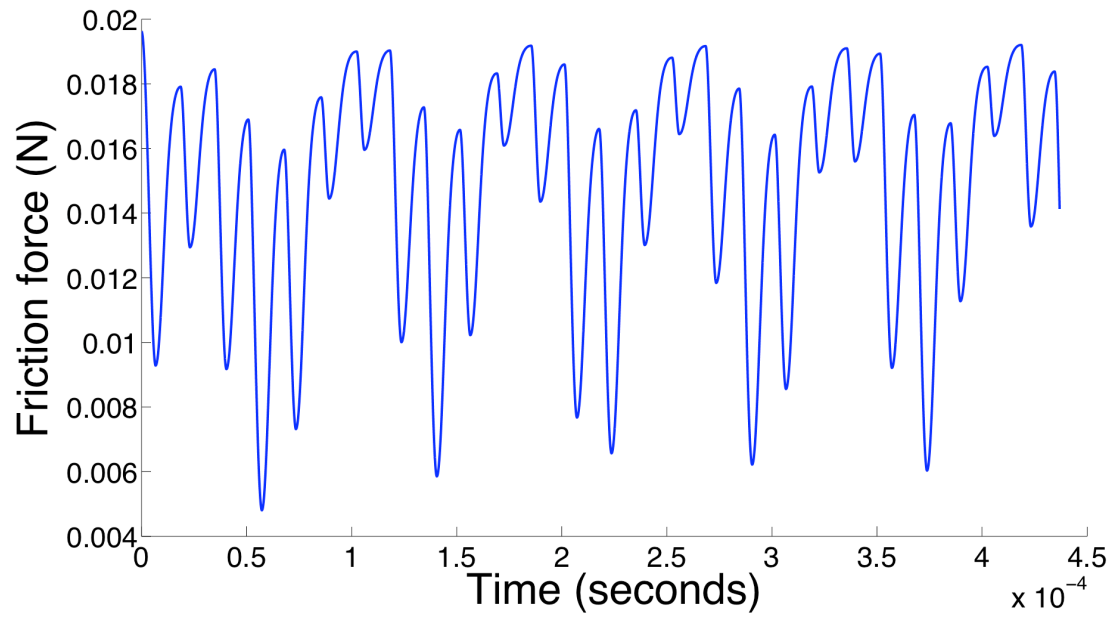


Figure 4.9: (a) Instantaneous friction force vs. time (b) Instantaneous power dissipation vs. time.

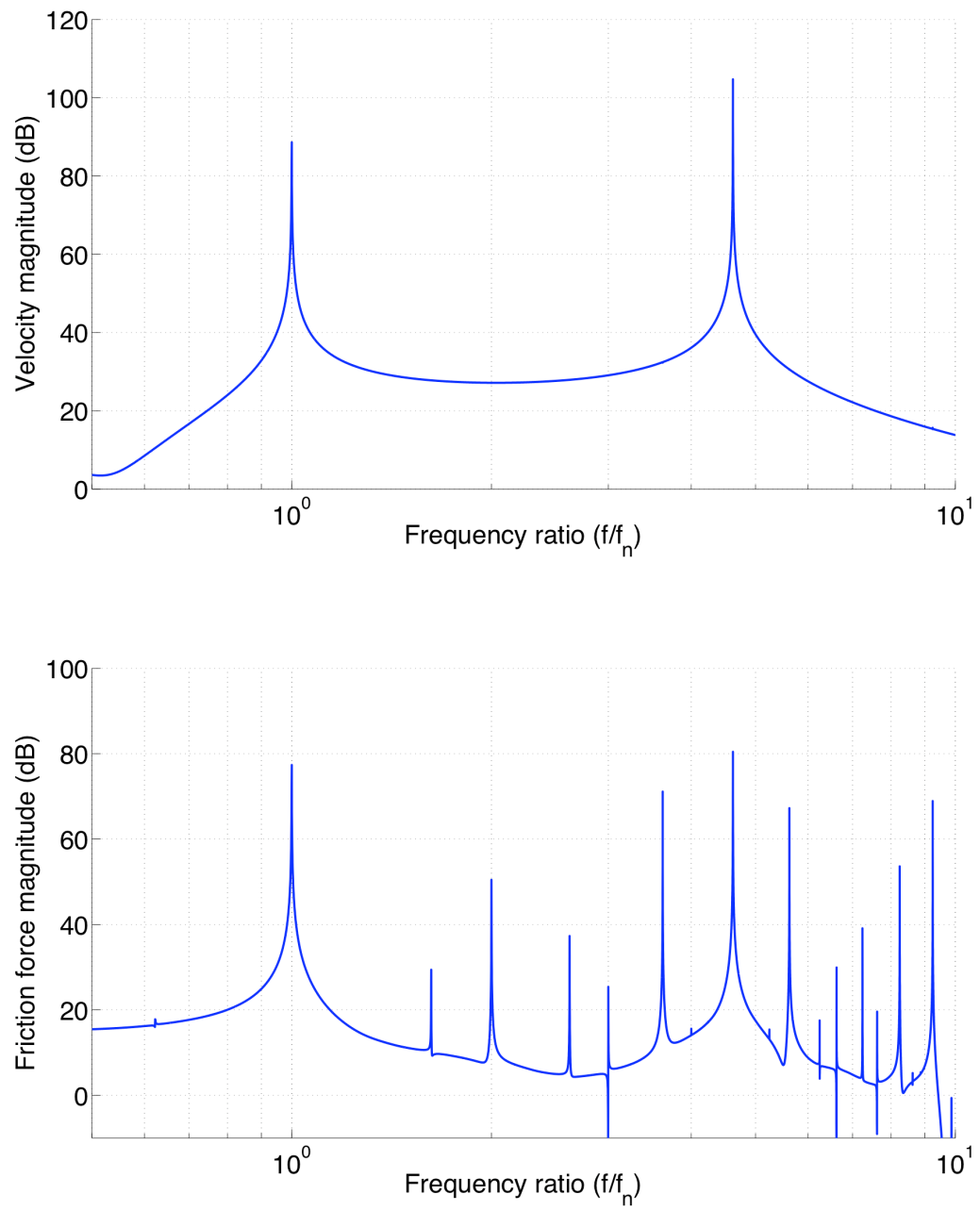


Figure 4.10: Fast Fourier Transform of (a) Velocity (b) Friction force.

masses, the natural frequency can hover around the ultrasonic excitation frequency. Vibrations occurring at the natural frequency are called friction-induced oscillations and give rise to undesired effects such as ‘squeal’ and ‘chatter’ in physical systems. When the frequency of excitation is very high compared to the natural frequency, these friction-induced oscillations can be suppressed. A ‘positive’ role of these friction induced oscillations is their tendency to lower the true frictional force. In the absence of an external excitation, the only force acting on the system is the friction force which induces self-excited oscillations. These vibrations are sinusoidal and give rise to a finite velocity ratio, corresponding to which there will be a theoretical friction reduction. However, in most practical systems, the magnitude of these oscillations are very small and hence may not contribute to the friction reduction.

4.3.2 Energy Considerations

The ultrasonic transducer is modeled using a SDOF system shown in Figure 4.4. The friction ratio provides information about the velocity considerations whereas the power dissipation ratio relates the input, stored and dissipated energy.

Considering the case without any ultrasonics, energy must be supplied to the mass for it to slide with velocity, \mathbf{V}_t . Let this input force be F_i . Then, the energy E_i required to slide the mass over a time period, T is given by

$$E_i = F_i V_t T. \quad (4.20)$$

A part of this energy is converted to kinetic energy and a part of it is dissipated due to friction. The kinetic energy is given by

$$E_k = \frac{1}{2} m V_t^2, \quad (4.21)$$

and frictional energy dissipated is

$$E_f = F_n V_t T, \quad (4.22)$$

where F_n is the intrinsic friction force in the absence of any ultrasonic vibrations.

Thus,

$$F_i V_t T = \frac{1}{2} m V_t^2 + F_n V_t T. \quad (4.23)$$

In the presence of ultrasonics, besides the input energy to slide the mass, energy must be provided for generating ultrasonic vibrations. For a piezoelectric system, this energy is in the form of electrical power. The voltage generates a piezoelectric control force, F_e that vibrates the mass. This force is a time varying function since the excitation is a function of time. The total input energy into the system in time T is given by:

$$\begin{aligned} E_{input} &= F_i V_t T + \int_0^T F_e(t) \dot{x}(t) dt \\ &= \frac{1}{2} m V_t^2 + F_n V_t T + \int_0^T F_e(t) \dot{x}(t) dt. \end{aligned} \quad (4.24)$$

This energy is converted partly to kinetic energy, partly to spring potential energy and the remaining is dissipated due to friction.

The average kinetic energy during time T is given by:

$$\begin{aligned} E_{ku} &= \frac{1}{T} \int_0^T \frac{1}{2} m (V_{rel}(t))^2 dt \\ &= \frac{1}{T} \int_0^T \frac{1}{2} m (V_t + \dot{x}(t))^2 dt. \end{aligned} \quad (4.25)$$

The average energy stored in the spring in time T is

$$E_{pu} = \frac{1}{T} \int_0^T \frac{1}{2} K_S(x(t))^2 dt. \quad (4.26)$$

The frictional energy dissipated during time T is given by

$$E_{fu} = \int_0^T F_f(t)(V_t + \dot{x}(t))dt. \quad (4.27)$$

Thus,

$$\begin{aligned} \frac{1}{2}mV_t^2 + F_nV_tT + \int_0^T F_e(t)\dot{x}(t)dt &= \frac{1}{T} \int_0^T \frac{1}{2}m(V_{rel}(t))^2dt + \frac{1}{T} \int_0^T \frac{1}{2}K_S(x(t))^2dt \\ &+ \int_0^T F_f(t)(V_t + \dot{x}(t))dt. \end{aligned} \quad (4.28)$$

$$\begin{aligned} F_nV_tT + \int_0^T F_e(t)\dot{x}(t)dt &= \frac{1}{T} \int_0^T \frac{1}{2}m(\dot{x}(t))^2dt + \frac{1}{T} \int_0^T mV_t\dot{x}(t)dt \\ &+ \frac{1}{T} \int_0^T \frac{1}{2}K_S(x(t))^2dt + \int_0^T F_f(t)(V_t + \dot{x}(t))dt. \end{aligned} \quad (4.29)$$

Let

$$E_{su} = \frac{1}{T} \int_0^T \frac{1}{2}m(\dot{x}(t))^2dt + \frac{1}{T} \int_0^T mV_t\dot{x}(t)dt + \frac{1}{T} \int_0^T \frac{1}{2}K_S(x(t))^2dt, \quad (4.30)$$

and

$$E_{iu} = \int_0^T F_e(t)\dot{x}(t)dt. \quad (4.31)$$

By dividing equation 4.29 throughout by F_nV_tT and using equations 4.22 , 4.27 , 4.30 and 4.31, the following equation is obtained:

$$1 + \frac{E_{iu}}{E_f} = \frac{E_{su}}{E_f} + \frac{E_{fu}}{E_f}. \quad (4.32)$$

$$\frac{E_{fu}}{E_f} = 1 + \frac{E_{iu}}{E_f} - \frac{E_{su}}{E_f}. \quad (4.33)$$

Thus, E_{fu} is the energy dissipated due to friction in the presence of ultrasonics;

E_f is the energy dissipated due to friction in the absence of ultrasonics;

E_{iu} is the ultrasonic energy input into the system;

E_{su} is the system energy and comprises of the kinetic and potential energies.

In terms of energy per unit time or power, equation 4.33 as,

$$\frac{P_{fu}}{P_f} = 1 + \frac{P_{iu}}{P_f} - \frac{P_{su}}{P_f}, \quad (4.34)$$

where the notation P denotes power and all subscripts the same as defined earlier.

Thus, the power dissipation ratio is given by,

$$\phi_{ru} = 1 + \phi_{iu} - \phi_{su}, \quad (4.35)$$

where ϕ_{ru} is the power dissipation ratio, ϕ_{iu} is the ratio of the ultrasonic input power to the frictional power dissipated with no ultrasonics, and ϕ_{su} is the ratio of the power used by the system to the frictional power dissipated with no ultrasonics.

The term ϕ_{iu} represents the input power to be provided to the system, and ϕ_{su} represents the power consumed by the system in the form of potential and kinetic energy.

The power dissipation ratio varies depends on system parameters namely, mass, system stiffness, contact stiffness, piezo control force and coefficient of friction.

4.3.3 Effect of Controlling System Parameters

From equations 4.14 and 4.16, independent parameters which contribute to the system behavior and friction reduction are identified. The mass, system stiffness, contact stiffness, piezo control force, relative velocity, and coefficient of friction are parameters which characterize the frictional behavior of the system. Parametric analysis of frictional force with focus on friction reduction at a system level is a novel and unique approach. The effect of load [6], velocity ratio and tangential stiffness [7] have been analyzed using Coulomb and Dahl equations. The contribution of system dynamics has been incorporated in this research. The goal is to analyze how each of these system parameters affect the friction reduction phenomenon. The velocity, displacement, friction force and power are not pure sinusoids as proposed by the Coulomb and Dahl models due to the effect of the natural frequency of the system.

The simulation results presented here correspond to a chosen set of parameter values (Table 4.1) which are based on existing experimental and computational data in the literature [15], [18] and [27].

4.3.3.1 Effect of Control Force

In a typical ultrasonic system, the control force is generated by piezoelectric elements when excited with a voltage. The relationship between the force generated and the applied voltage is assumed linear. This control force acts as an external excitation to a SDOF model at a given ultrasonic frequency. Figure 4.11(a) shows the effect of control force on the friction ratio. An increase in control force decreases the friction ratio. With higher control force, the velocity of vibration increases, which in turns decreases the velocity ratio. By providing higher energy into the system increases

the effect of friction reduction. The power dissipation ratio correlates to the amount of input power required to obtain a desired velocity ratio and corresponding friction ratio. For lower velocity ratios, much higher power is required. As the control force is increased, the term E_{iu} increases. Thus, the power dissipation ratio increases with increase in control force (Figure 4.11(b)).

4.3.3.2 Effect of Coefficient of Friction

The coefficient of friction determines the resistance offered to the sliding and vibratory motion of the mass. When the coefficient of friction is low, friction reduction is achieved more easily than in the case of high friction coefficient. Figure 4.12(a) shows that the friction ratio increases with increase in friction coefficient. E_f is affected by the value of the friction coefficient. A high coefficient of friction implies a lower ϕ_{iu} and ϕ_{su} . As a result, the power dissipation ratio decreases with increase in friction coefficient as shown in Figure 4.12(b).

4.3.3.3 Effect of Load

An increase in load reduces the effect of friction reduction. Fig. 4.13(a) shows that the friction ratio curve begins to flatten as load increases. This implies that for a given control force, the maximum possible friction reduction is limited by the mass of the sliding body. An increase in normal load increases frictional force which will need higher ultrasonic energy to be overcome. In Fig. 4.13(b), the power dissipation ratio dips as load increases. The system energy increases, implying that at low velocity ratios, the power dissipated with ultrasonic vibrations is very low. The potential energy in the spring is much smaller in magnitude compared to the input

energy. The effect of mass shows significantly in the term ϕ_{su} , which increases with increasing load.

4.3.3.4 Effect of Friction Induced Oscillations

A single degree-of-freedom system acted upon by friction gives rise to self-excited friction induced oscillations. The amplitude of these vibrations depends on the magnitude of the friction force. The friction force in case of Dahl model is the product of the tangential contact stiffness and the elastic displacement of the asperities. Thus, a high contact stiffness implies higher friction acting on the system. To understand the effect of these oscillations, the system is studied in the absence of an excitation force for different values of the contact stiffness. In Figure 4.14(a), it is evident that as the tangential contact stiffness is increased, friction reduction is more pronounced. From a design stand point, surfaces in contact should be as hard as possible for friction reduction to take advantage of these friction induced oscillations. However, these oscillations occur at the natural frequency of the system. For optimum performance, the natural frequency should be as high as possible to reduce squeal and chatter. In Figure 4.14(b), the power dissipation is always less than unity since ϕ_{iu} is zero. The ratio drops with increasing contact stiffness. By increasing contact stiffness, the system energy increases and hence the power dissipation ratio decreases with K_t .

4.3.3.5 Effect of System Stiffness

The rigid Coulomb model and Dahl models do not take the system stiffness into consideration. These analyses are based on assuming an infinitely stiff spring to which a mass is connected. However, the friction reduction is affected due to compliance in the system. An interesting case of this system stiffness occurs when the excitation

frequency is set at the natural frequency of the system. When this occurs, the displacement and hence velocity of vibration increases by virtue of the system properties. An increase in the vibration velocity reduces the velocity ratio which in turn lowers friction ratio (Figure 4.15(a)). At higher vibration velocities, the power dissipation due to friction is also high. For lower values of K_S , the power dissipation ratio is not affected significantly (Figure 4.15(b)). Thus, it is desirable to operate systems at their natural frequency to maximize the effect of friction reduction.

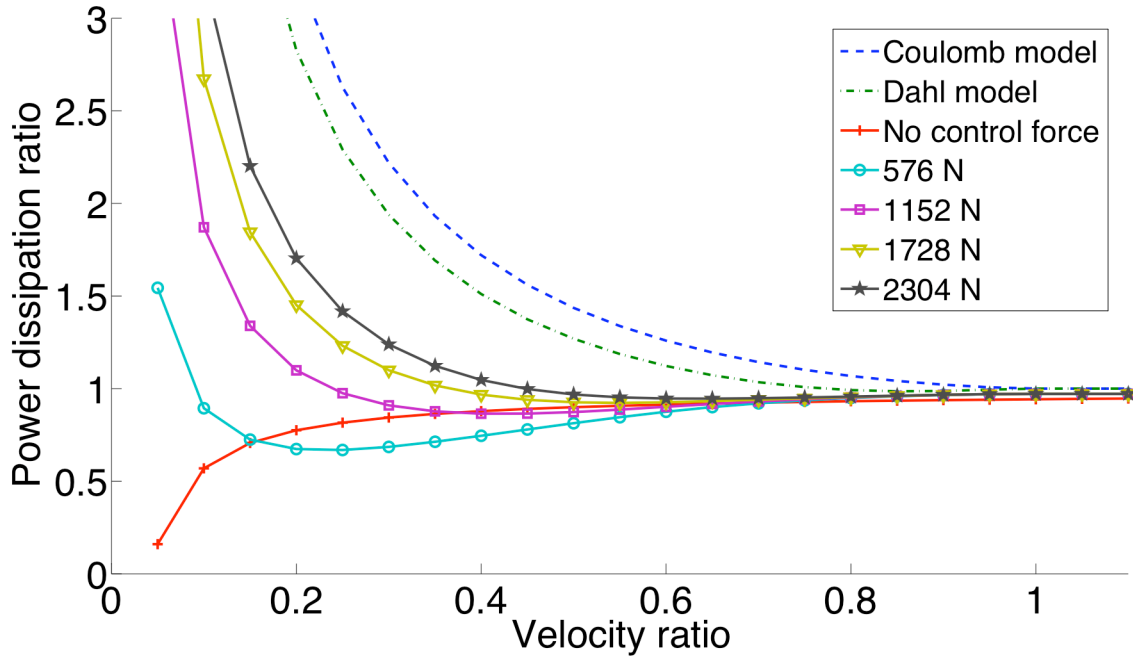
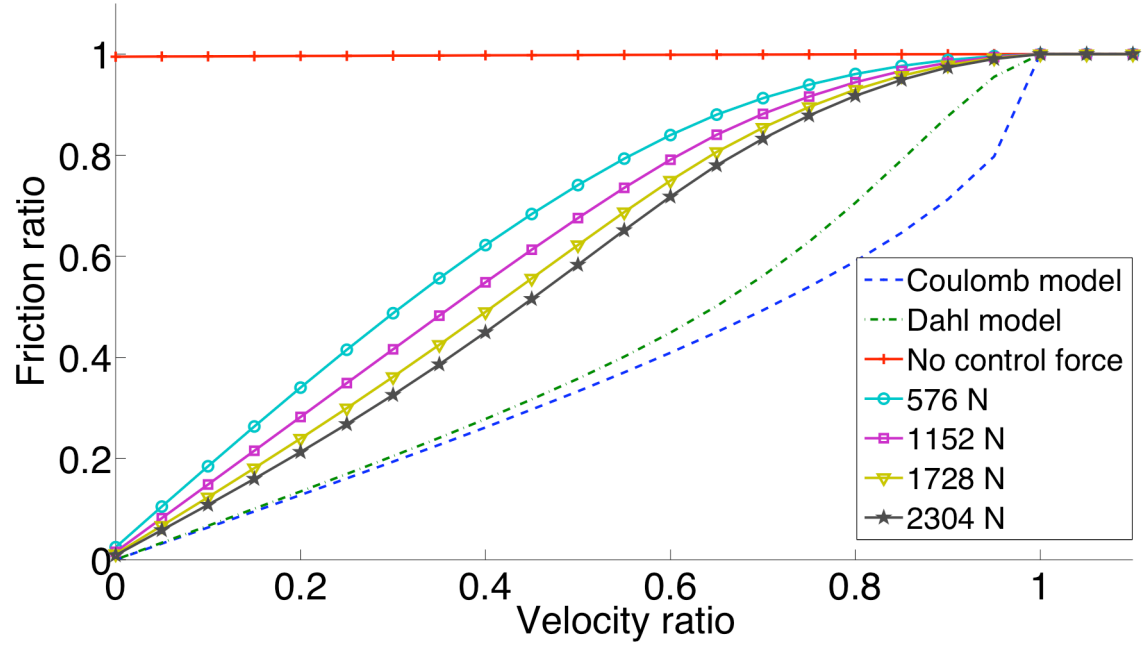


Figure 4.11: Effect of control force on (a) Friction ratio vs. velocity ratio (b) Power dissipation ratio vs. velocity ratio.

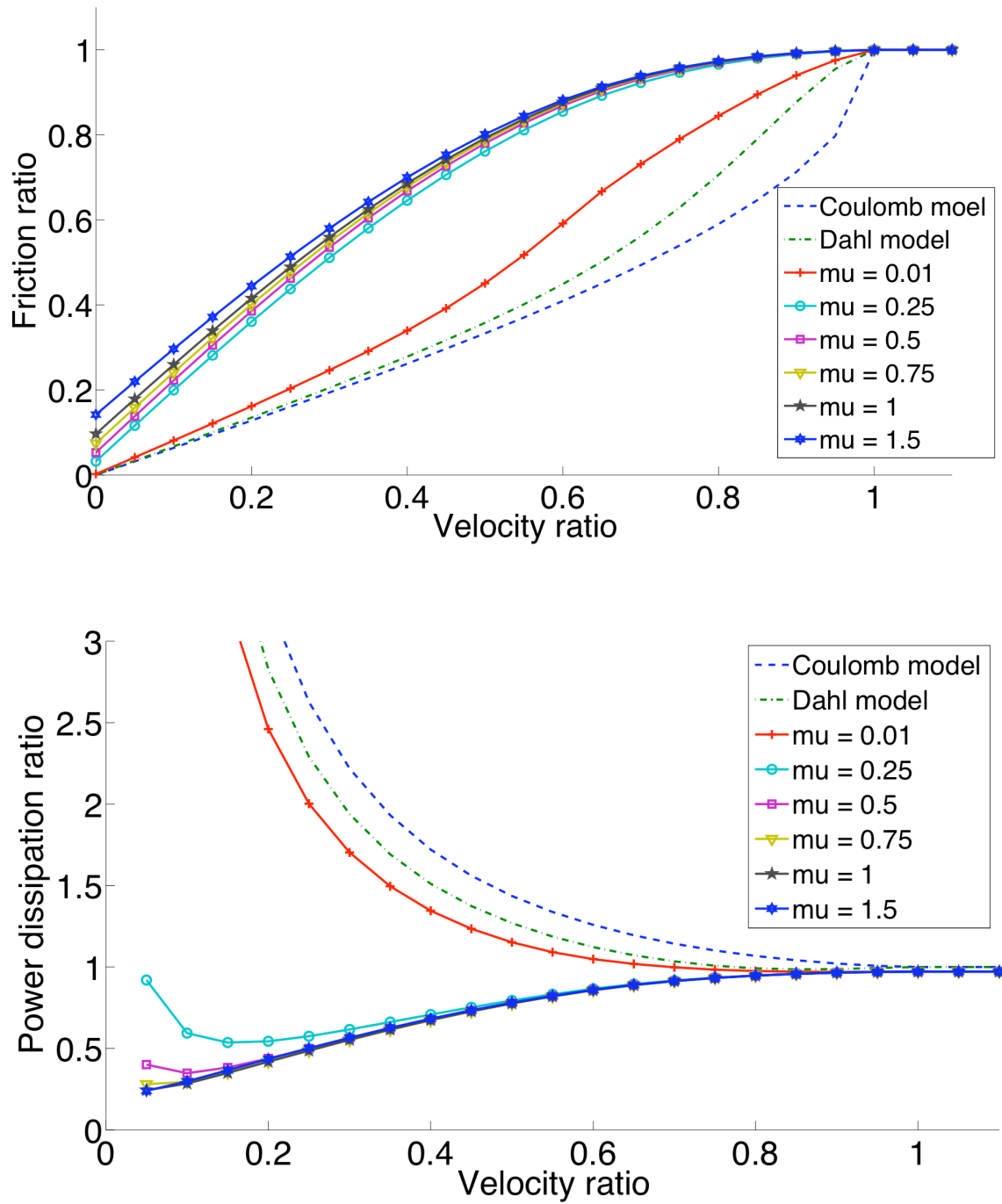


Figure 4.12: Effect of coefficient of friction on (a) Friction ratio vs. velocity ratio (b) Power dissipation ratio vs. velocity ratio.

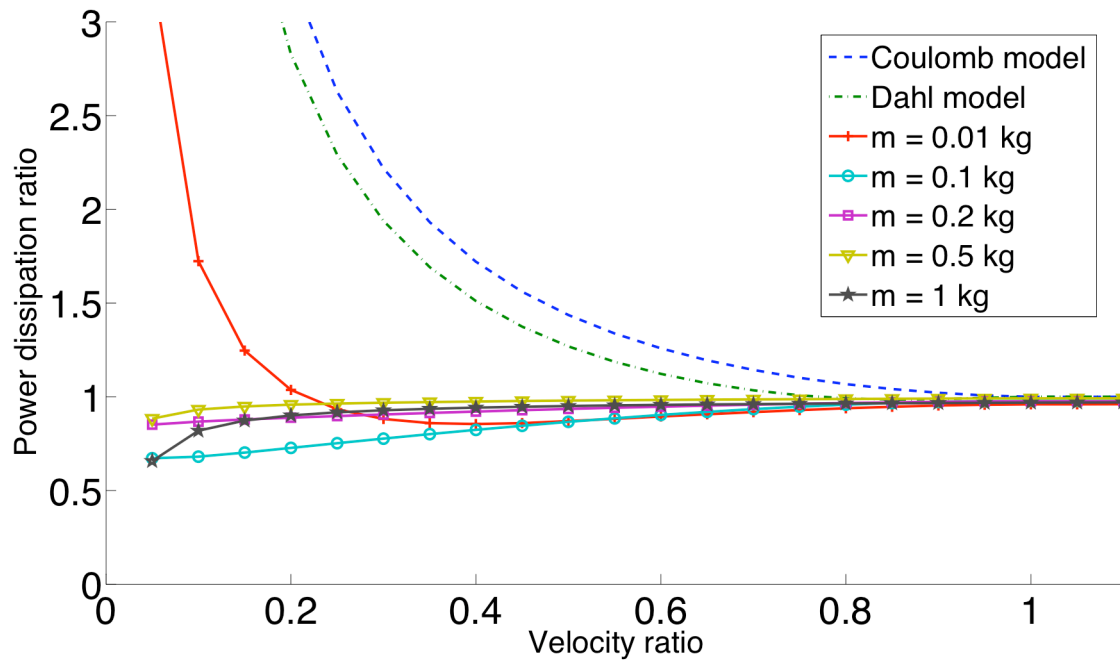
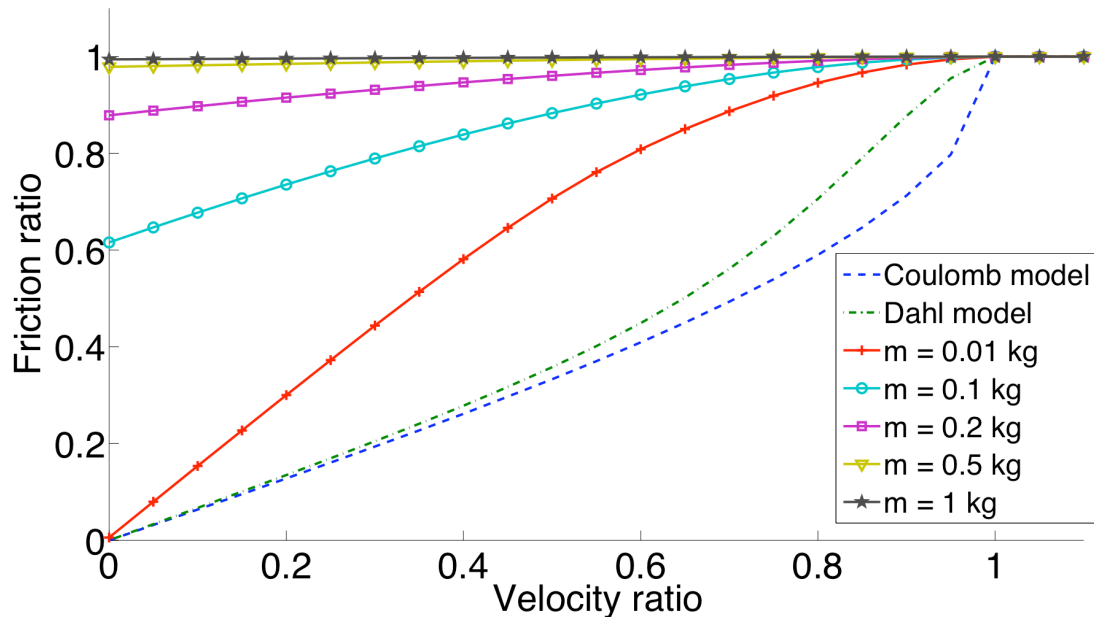


Figure 4.13: Effect of load on (a) Friction ratio vs. velocity ratio (b) Power dissipation ratio vs. velocity ratio.

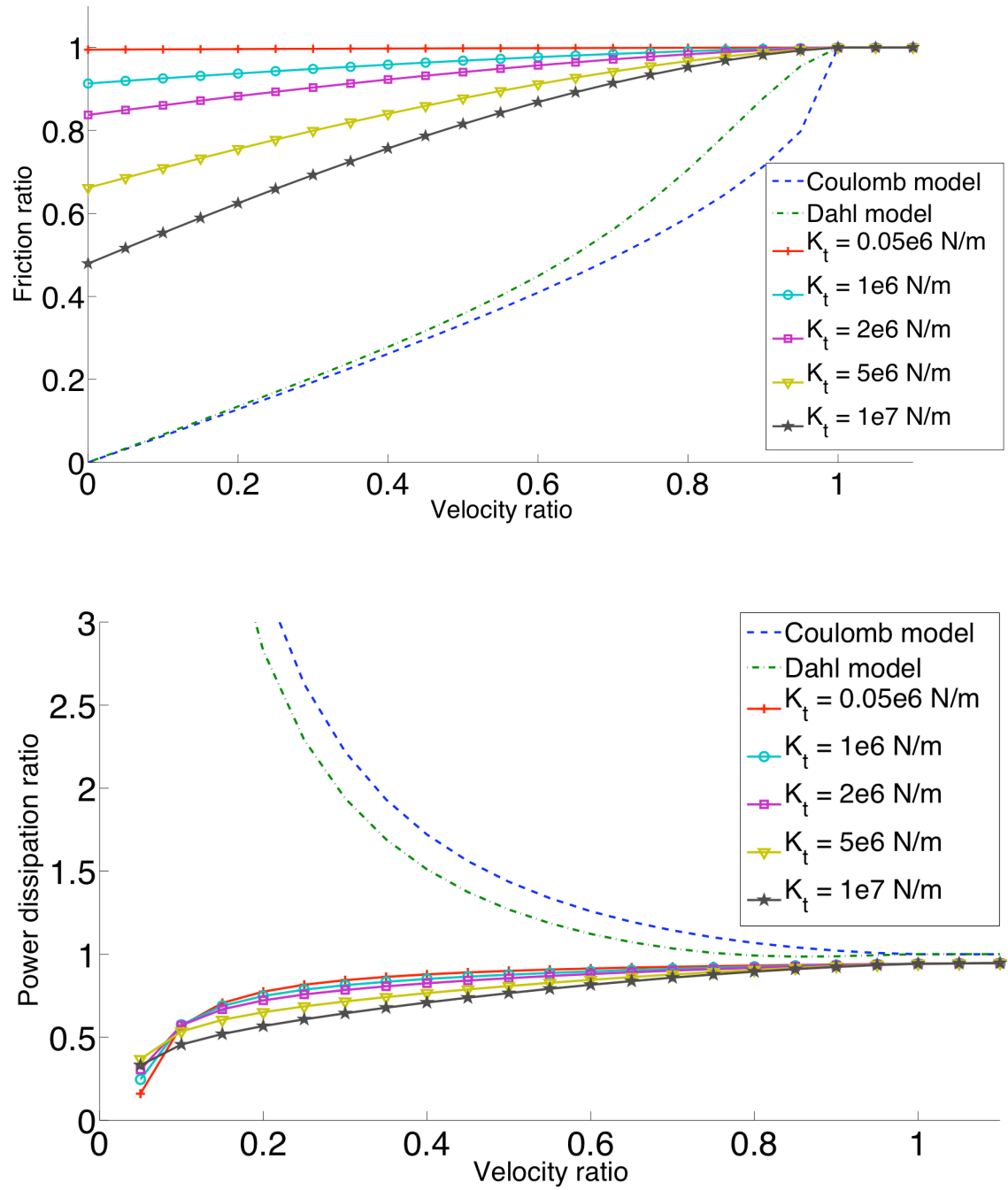


Figure 4.14: Effect of friction induced oscillations on (a) Friction ratio vs. velocity ratio (b) Power dissipation ratio vs. velocity ratio.

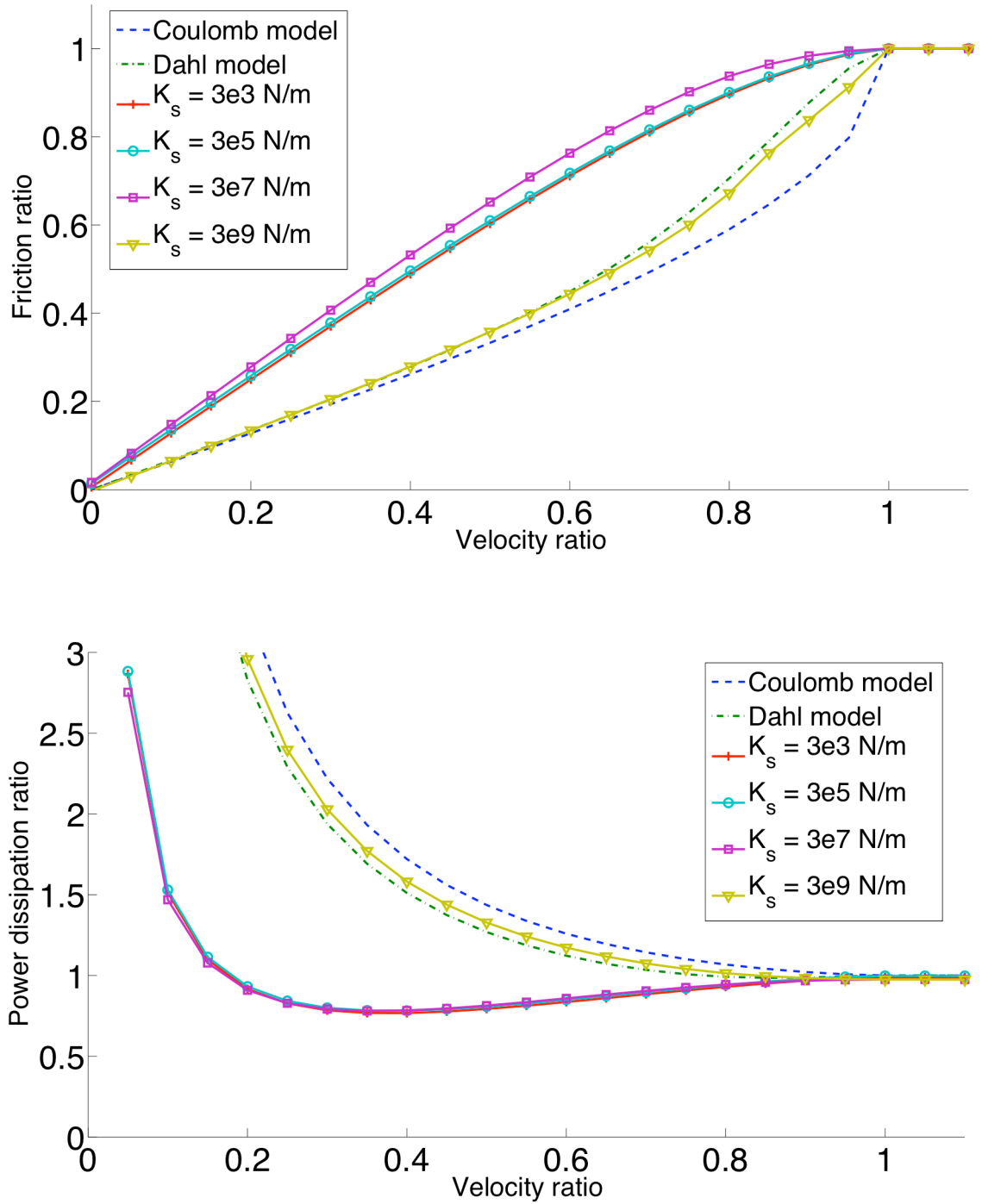


Figure 4.15: Effect of system stiffness on (a) Friction ratio vs. velocity ratio (b) Power dissipation ratio vs. velocity ratio.

4.3.4 Correlation with Experimental Data

The system model described above is compared with experimentally obtained results by Littmann et al. [17], [18], [25] based on specified values for mass, tangential stiffness, and coefficient of friction [15], [17],[18], [25] and [27]. From Figure 4.16, it is seen that the system model appears to conform much better to the experimental data. At low velocity ratios, experiments have reported a higher friction ratio than the theoretical model prediction. Due to inertial effects of load, coefficient of friction, and friction induced oscillations, it is not possible to attain zero friction ratio, as predicted by the Coulomb and Dahl models. As a result, higher ultrasonic energy will need to be supplied into the system. The dynamic model selected for this analysis is a simple SDOF model capable of capturing most aspects of active friction reduction. Other complicated models to include damping and viscous effects, or continuous models are possible at the cost of computational effort.

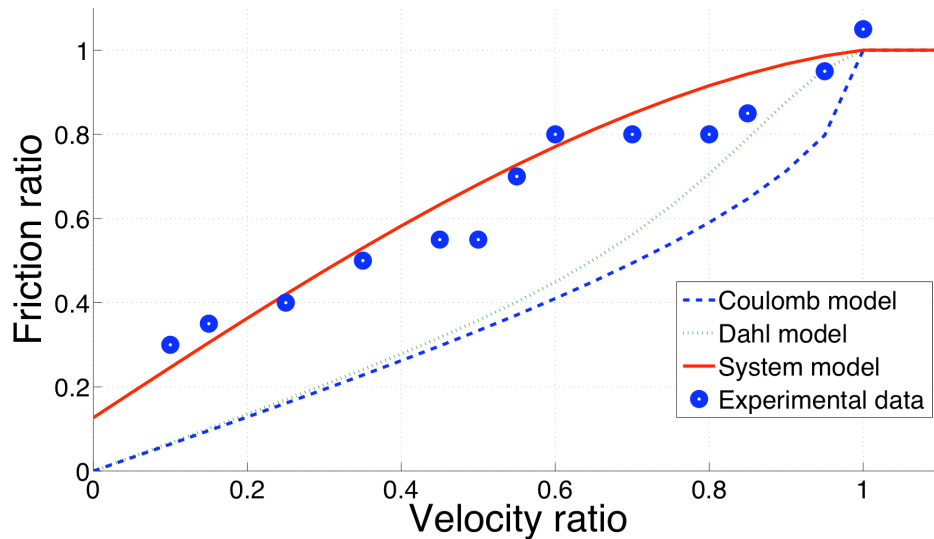


Figure 4.16: Comparison of various models with experimental data.

4.4 Influence of Tangential Excitation Waveforms

It is also of interest to understand how different excitation waveforms affect the extent of friction reduction. With digital function generators, it is possible to generate most of these waveforms physically. The governing equations of motion for the SDOF model is

$$\mathbf{m}\ddot{\mathbf{x}} + \mathbf{k}_s\mathbf{x} = \mathbf{F}_e(t) - \mathbf{F}_D, \quad (4.36)$$

where \mathbf{m} is the mass of the sliding body, \mathbf{k}_s is the system stiffness, \mathbf{F}_0 is the control force generated to drive the system, and ω_e is the excitation frequency.

\mathbf{F}_D is the Dahl friction force which is given by equation 4.16.

$\mathbf{F}_e(t)$ may be represented using linear or nonlinear functions depending on the analysis. From these equations, the friction force is solved for, using different waveforms of excitation. Table 4.1 shows the various simulation parameters used for this model.

The waveforms used in the simulations are square, sawtooth, random, chirp and sine.

4.4.1 Effect of Excitation Waveforms on Dahl Equation

For a velocity ratio of 0.5 and an excitation frequency of 60 kHz, the following results are obtained. For the chirp signal, the initial frequency is set at 20 kHz, and the final frequency to be attained at the end of the simulation time is 200 kHz.

In Figure 4.17, the time domain plot of friction force varies with different excitation waveforms. Theoretically, the square wave may be represented a series of step functions. This response resembles Coulomb's friction law.

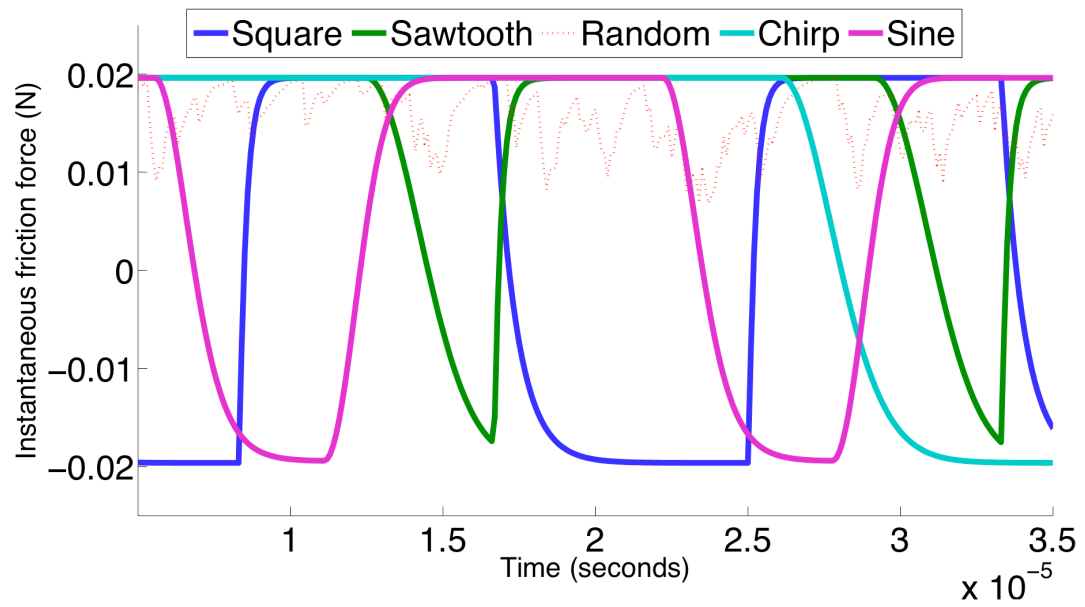


Figure 4.17: Dahl friction force vs. time.

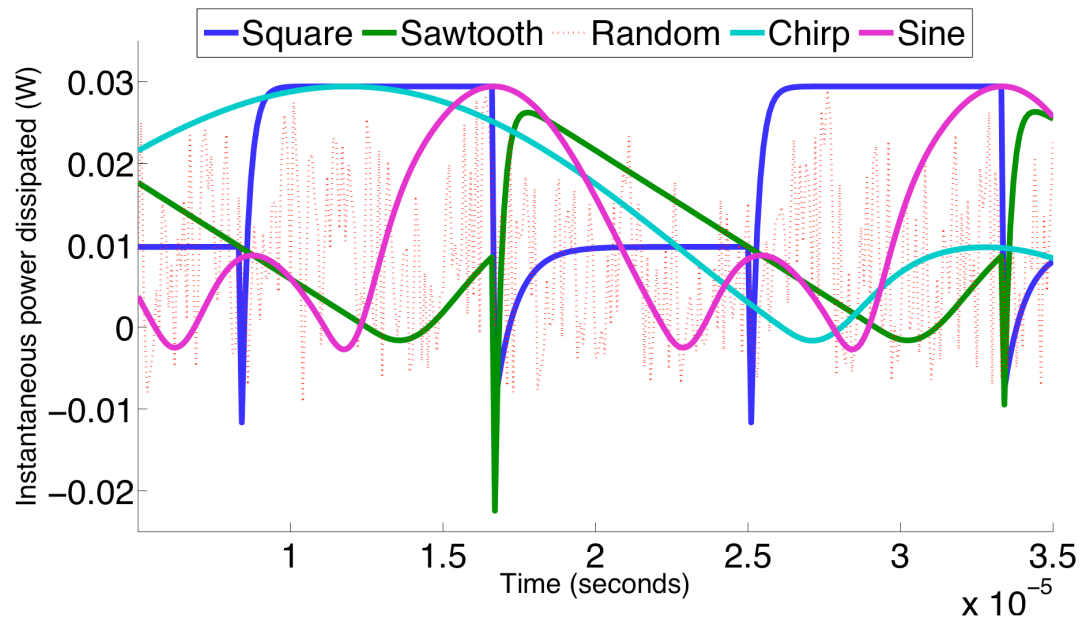


Figure 4.18: Instantaneous power vs. time.

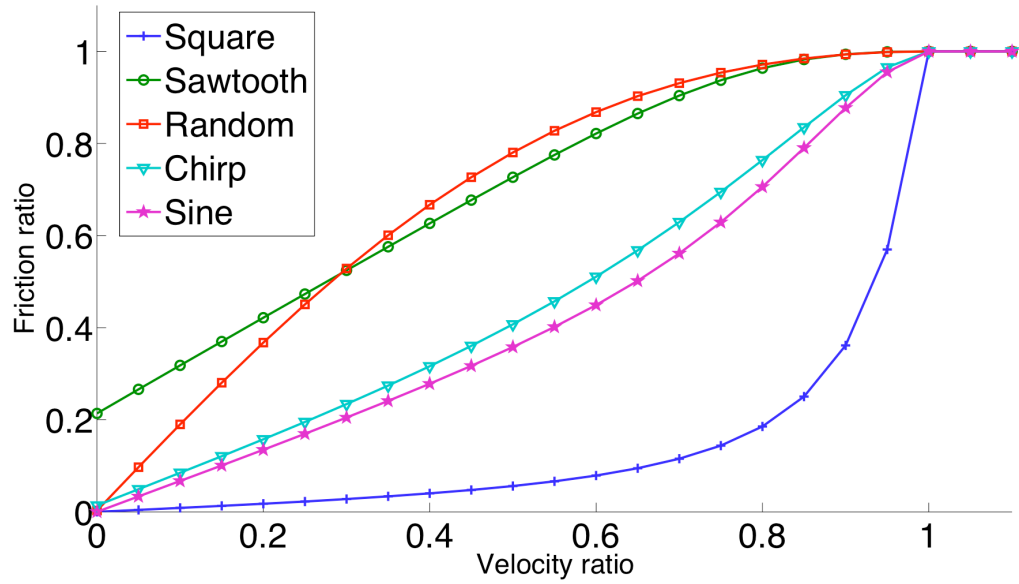


Figure 4.19: Friction ratio versus velocity ratio.

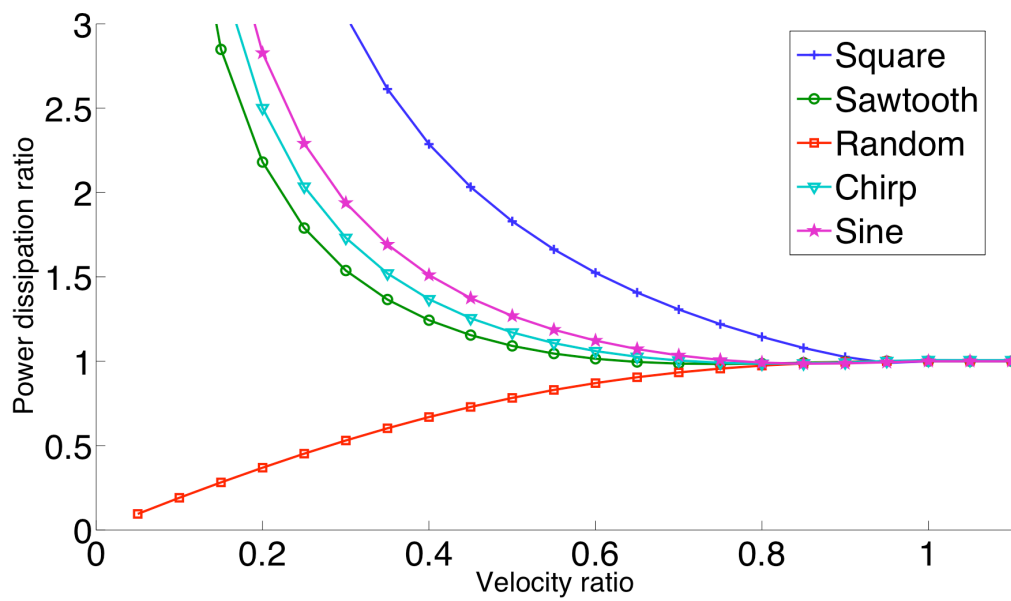


Figure 4.20: Power dissipation ratio versus velocity ratio.

The sawtooth signal produces a more or less triangular wave in response. Since the duration of the signal bottoming out at a negative friction force is low, the mean friction force is higher. Depending on the time resolution, a very high frequency sine wave may be approximated by a triangular wave.

The chirp signal is a special type of excitation where the frequency of excitation varies with time. As a result, such signals are nonstationary in nature. In response to a chirp signal, the friction force also varies in frequency with time. In order to determine the frequency components of a signal, Fast Fourier Transforms (FFT) are used. However, FFTs are meant for use only for stationary data i.e. when all the frequencies exist at all times. Nonstationary data analysis may be done using Wavelets or Wigner distributions.

Figure 4.18 shows the time plot of the instantaneous power dissipated due to friction. It is evident that there are multiple frequencies present in each waveform.

From Figure 4.19, it is found that the friction reduction is most effective in the case of a square wave excitation. Due to its discontinuous nature, the square wave assists and resists motion within well defined boundaries. A consequence of higher friction reduction is a high power dissipation ratio. Thus, the amount of energy consumed in the case of square wave excitation is also high compared to the other waveforms (Figure 4.20).

4.4.2 Effect of Excitation Waveforms on SDOF Model

In the time domain, it is found that the displacement plot (Figure 4.21) for each excitation waveform is different. While random excitation does not produce significant displacement, the chirp signal produces the highest amplitude of displacement. This

in turn, results in higher velocity amplitudes (Figure 4.22). Since a high vibration velocity assists in reducing friction, the friction force bottoms out at a much lower negative force. As a result, the mean friction force reduces.

The time domain plots for instantaneous power dissipation due to friction shows that the chirp signal peaks higher than other waveforms (Figure 4.24). From the friction ratio vs. velocity ratio plot in Figure 4.25, it is seen that when using a SDOF model, the chirp signal is most effective in reducing friction. Consequently, the power dissipation ratio is highest for the chirp signal as seen in Figure 4.26. Further analysis on the range of frequencies and simulation times can provide valuable information on optimizing the use of chirp in ultrasonic friction reduction.

4.5 Summary

Friction control is a function of many system parameters such as mass, system stiffness, contact stiffness, coefficient of friction, friction induced oscillations, and external excitation. The displacement and velocity of the mass have two frequency components which correspond to the natural and excitation frequencies. Friction force has a number of frequency components, and shows a decrease upon application of ultrasonic excitation. By numerical analysis, the effect of various parameters on friction reduction in presence of ultrasonic vibrations is addressed. The inertial effects of load in addition to coefficient of friction, and friction induced oscillations, prevents achieving a zero friction state. For practical applications involving friction control, design of ultrasonic systems can utilize these results and be optimized for ideal performance.

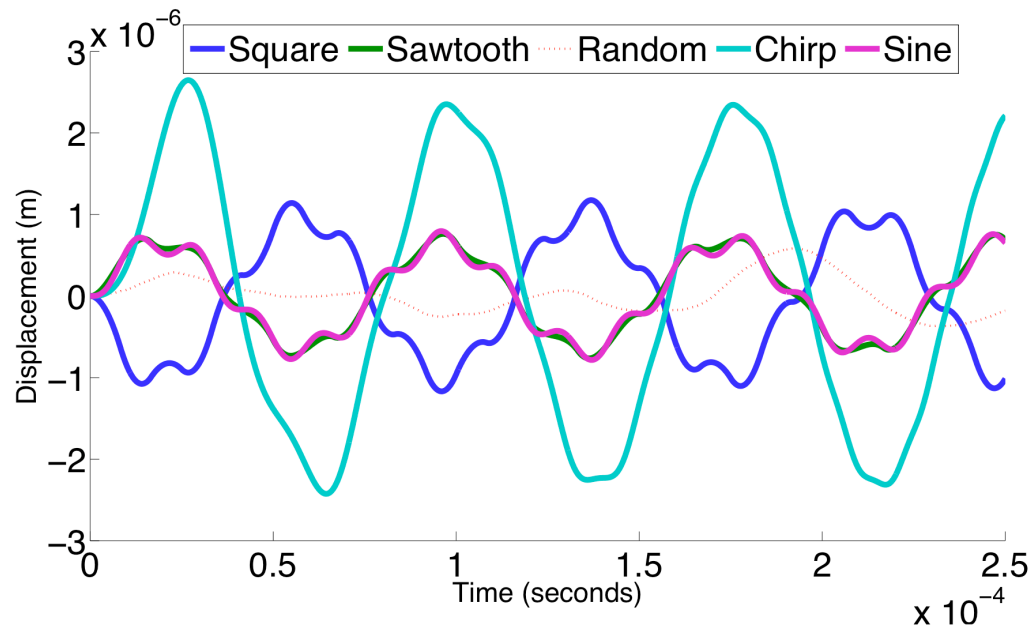


Figure 4.21: Displacement vs. time.

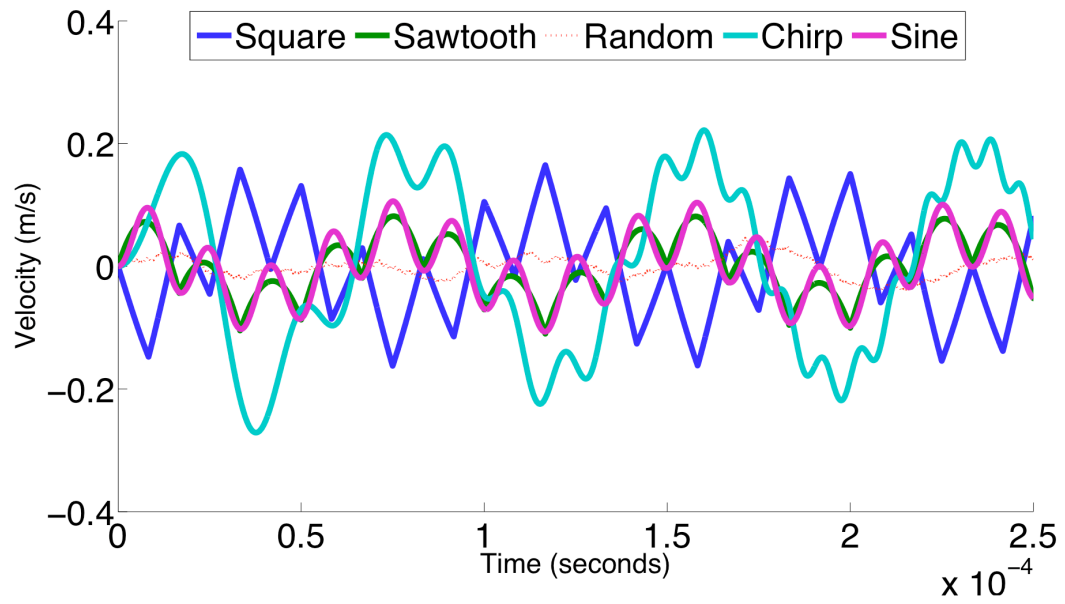


Figure 4.22: Velocity vs. time.

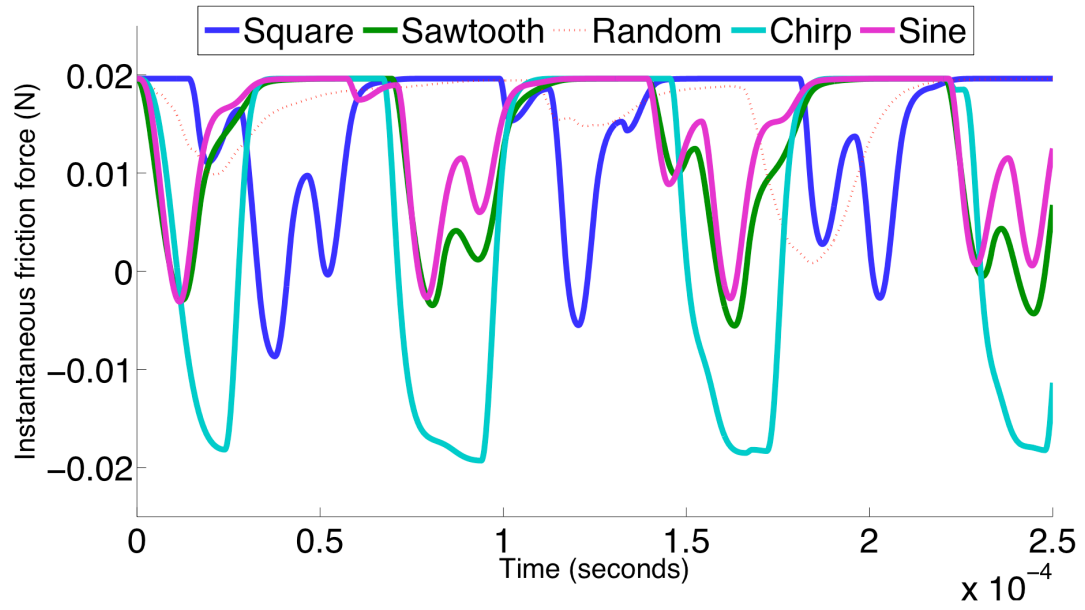


Figure 4.23: Friction force vs. time.

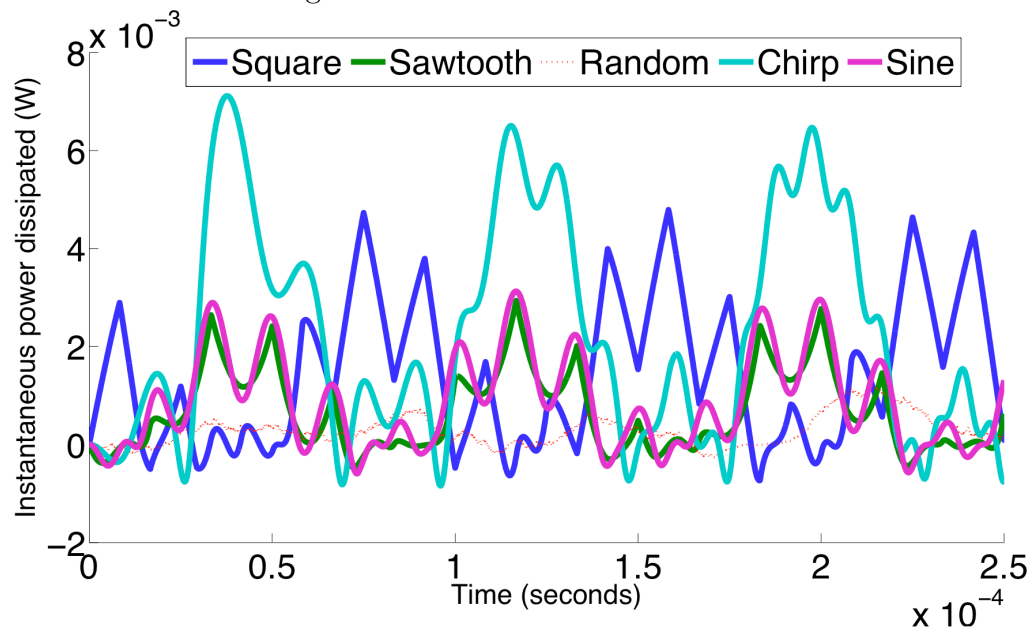


Figure 4.24: Instantaneous power dissipated vs. time.

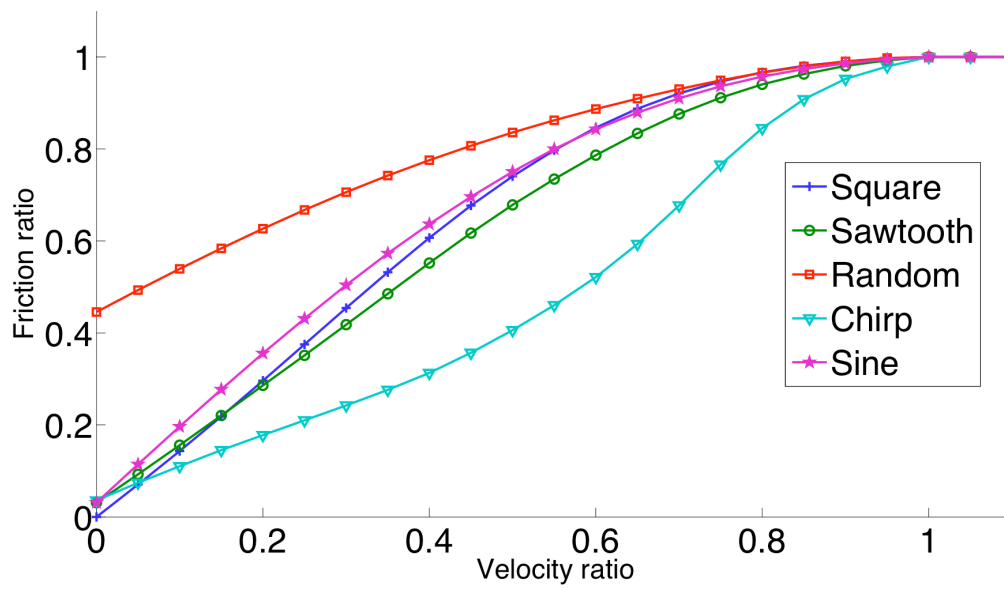


Figure 4.25: Friction ratio versus velocity ratio.

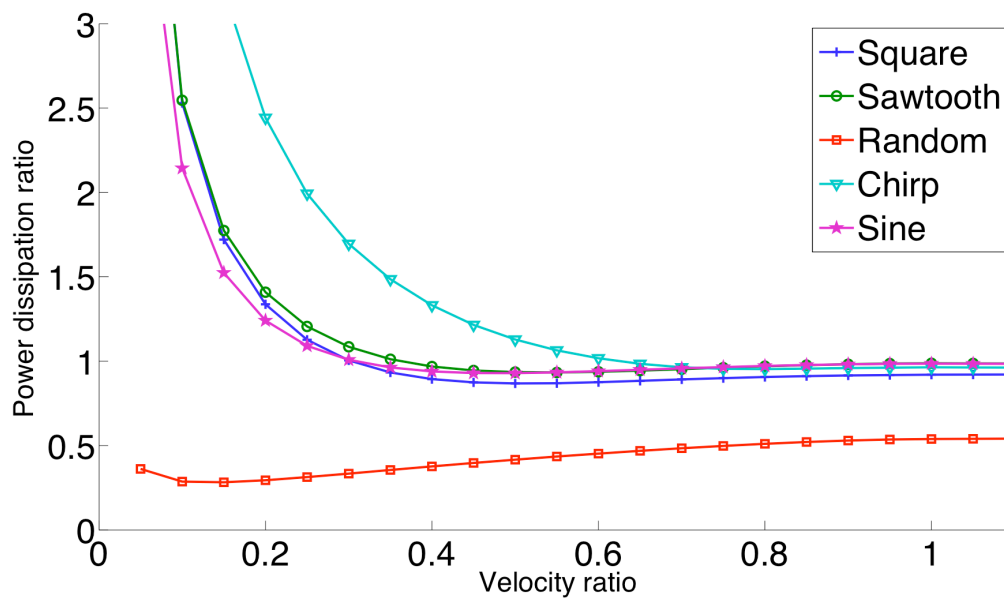


Figure 4.26: Power dissipation ratio versus velocity ratio.

The effect of various excitation waveforms on friction reduction in presence of ultrasonic vibrations is studied. The extent of reduction reported by these waveforms depends on the type of model used. In the case of Dahl's model, simulation results reveal that the square wave can significantly reduce friction. However, when the Dahl friction is coupled with a SDOF system, it is found that in the presence of system dynamics, the chirp signal is most effective. The chirp signal is nonstationary and contains different frequency components at different times. As a result, spectral analysis of the friction response cannot be done using Fourier transforms. In real-life systems, the role of system dynamics such as inertia due to load, system stiffness, etc, cannot be ignored. Thus, nonstationary chirp signals may be used to excite the system and obtain a higher percentage reduction in friction compared to conventional sinusoidal waveforms.

CHAPTER 5

CONCLUSION

5.1 Summary

The goal of this research was to develop an adaptive seat belt system to actively control the friction force at the interface between the D-ring and seat belt webbing. By superimposing ultrasonic vibrations on the sliding velocity, the average friction force at the interface is reduced. To that end, a systematic approach is developed, with the help of experiments and models, to predict and characterize the frictional force between sliding surfaces is the presence of ultrasonic vibrations under various controlling parameters.

Experiment #1 complements previous research showing that ultrasonic vibrations superimposed parallel to the macroscopic motion of a sliding object can reduce friction. The extent of friction reduction depends on the velocity ratio (ratio of the velocity of the sliding body to the velocity of ultrasonic vibrations). The effect is more pronounced at low velocity ratios. As the velocity ratio approaches unity, the effect of friction reduction decreases.

For low loads up to 10 N, a friction reduction up to 68% is obtained. In the presence of normal loads, the friction reduction decreases.

Experiment #2 is designed to determine the potential of out-of-plane normal vibrations in reducing friction in an automotive seat belt interface. Seat belts are highly compliant and textured and frictional properties at the interface are different from solid-solid contacts. Increasing load and velocity decreases the effect of friction reduction, similar to experiment #1. By providing significantly higher energy at the interface, a friction reduction of up to 58% is obtained. These experiments were conducted at low speeds of 0.025 m/s.

Both these experiments demonstrate the application of ultrasonic lubrication in friction reduction at various interfaces. The contact mechanics in a solid-solid interface is different from that in Hertzian contacts. Ongoing experimental work on the design an ultrasonic lubrication system for friction reduction in a high load and high speed environment replicates actual crash conditions in a realistic seat belt system.

The mechanism of active friction control is analyzed using friction models. Coulomb and Dahl models have been used to explain the mechanism. The LuGre friction model is found to incorporate most of the realistic aspects of friction observed in experiments. A novel approach to friction modeling was investigating the role of system dynamics. It was found that active friction control is a function of many system parameters such as mass, system stiffness, contact stiffness, coefficient of friction, friction induced oscillations, and external excitation. Unlike the Coulomb and Dahl models, where the displacement and velocity are assumed to be single frequency sinusoids corresponding to the excitation, the displacement and velocity of the mass have two frequency components which correspond to the natural and applied frequencies. Friction force,

however, has a number of frequency components, and shows a decrease upon application of ultrasonic excitation. Using numerical analysis, the parametric dependence of friction has been addressed.

The effect of tangential excitation waveforms on ultrasonic friction reduction is studied. Reduction depends on the type of model selected for analysis. For Dahl's model, the square wave is most effective for friction reduction. When the Dahl friction is coupled with a SDOF system, it is found that the chirp signal is most effective. Chirp signals contain different frequency components at different times. This entails nonstationary spectral analysis methods of the friction response such as Wavelets or Wigner distributions. Thus, chirp or square signals may be used to excite the ultrasonic lubrication system for maximum effectiveness.

5.2 Conclusions

This research has accomplished several key goals. The concept of ultrasonic lubrication at a macroscopic scale has been demonstrated with the help of experiments and models. The most important parameter that determines a desired friction reduction is the velocity ratio. For a given ultrasonic power, the extent of reduction decreases at higher speeds and loads. In experiment #1, at low loads up to 10 N, the power required to achieve 68% reduction in friction force is 6 W. However, experiment #2 requires nearly 1200 W at high loads of 670 N to obtain a friction reduction of 55%. This imposes a limit on the range of loads and speeds that allow for effective operation of the friction control system. Frictional behavior in the case of seat belt interfaces is complex. It is strongly dependent on the temperature, normal load and texture.

At high velocities, it is expected that local temperatures would rise due to frictional heat dissipation in addition to heat energy generated by ultrasonic vibrations.

Based on the analytical model simulations, some important conclusions are drawn. For maximum effectiveness in friction reduction, the excitation force must be as high as possible. This implies higher ultrasonic input power. The materials in contact must be smooth and the coefficient of friction must be as low as possible. The contacting surfaces must be hard so that the contact stiffness is high. The operating frequency, if set to the natural frequency of the system, leads to greater friction reduction. The design of ultrasonic lubrication systems for friction control may be based on these parameters.

This research has laid the groundwork for the development of adaptive seat belt systems that would lead to an unprecedented degree of occupant safety through active control of shoulder belt forces.

5.3 Future Work

One of the key challenges in applying this technology to an automotive seat belt system is the packaging and integration of the entire mechanism. Ongoing experimental work uses a massive Dukane ultrasonic transducer consuming 1 kW of power. Generation of high power ultrasonics to create a significant reduction in friction and act in a quick and energy efficient manner requires further study and analysis. Application of ultrasonic vibrations in a direction tangential or normal to the sliding motion of the seat belt webbing requires redesign of the D-ring. Using finite element methods, an optimal design for the electromechanical coupling mechanism between the actuator and the D-ring needs to be analyzed.

Of primary interest for further development is an analytical model incorporating the role of viscous damping and Stribeck effect. At high belt velocities, the lubrication at the interface may shift to the hydrodynamic regime with a thin layer of air between the D-ring and seat belt. The model can help predict the behavior of interfacial forces in a dynamic environment and shed light on attainable energy efficiencies.

The concept of active friction control has potential applications in various other automotive applications. This research has created a pathway to the development of smart automotive systems. Ultrasonic lubrication technology is applicable to a number of sliding mechanisms such as sat rails and powertrain components, seat backrest recliners based on joint friction control, and dashboard knobs with haptic feedback.

APPENDIX A

EXPERIMENT # 1 TEST SETUP DRAWINGS

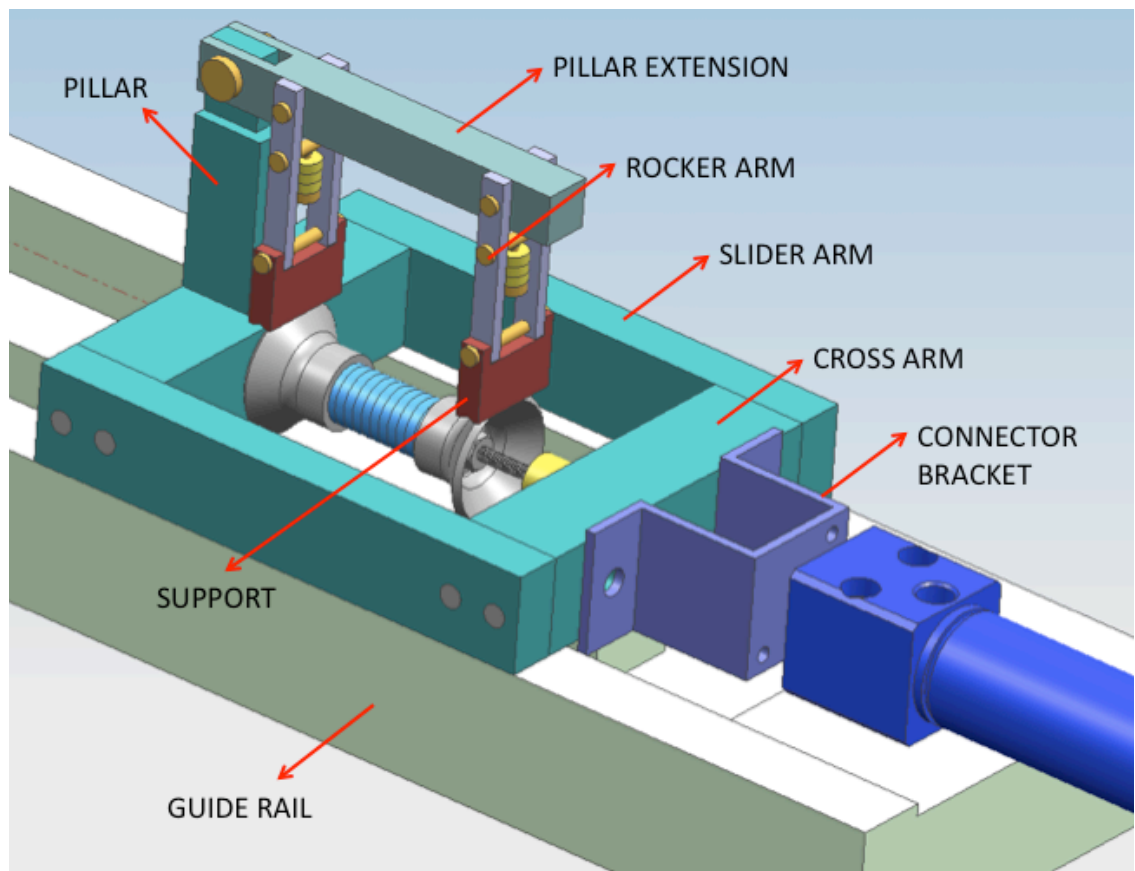


Figure A.1: Experimental #1 setup.

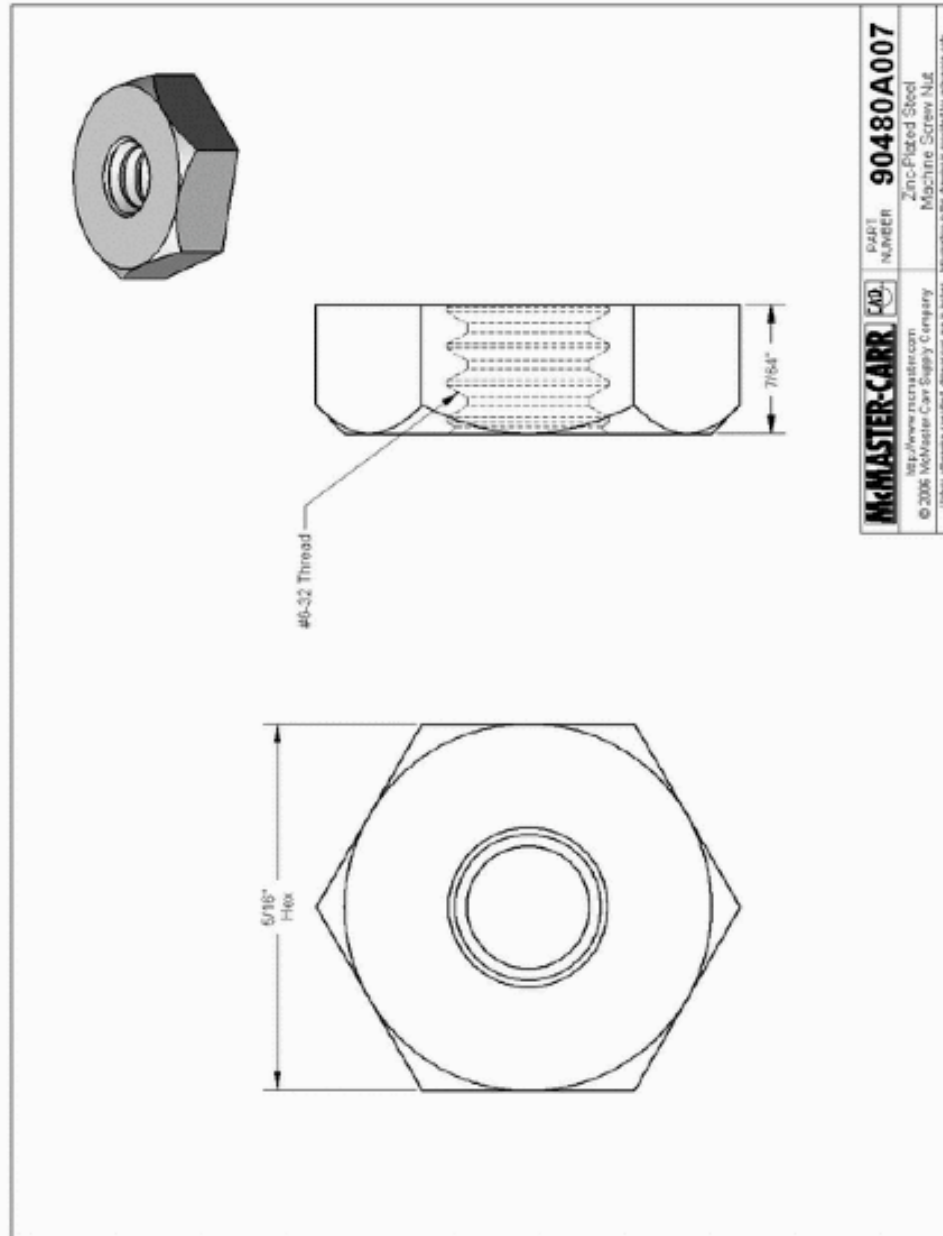


Figure A.2: #6-32 nut.

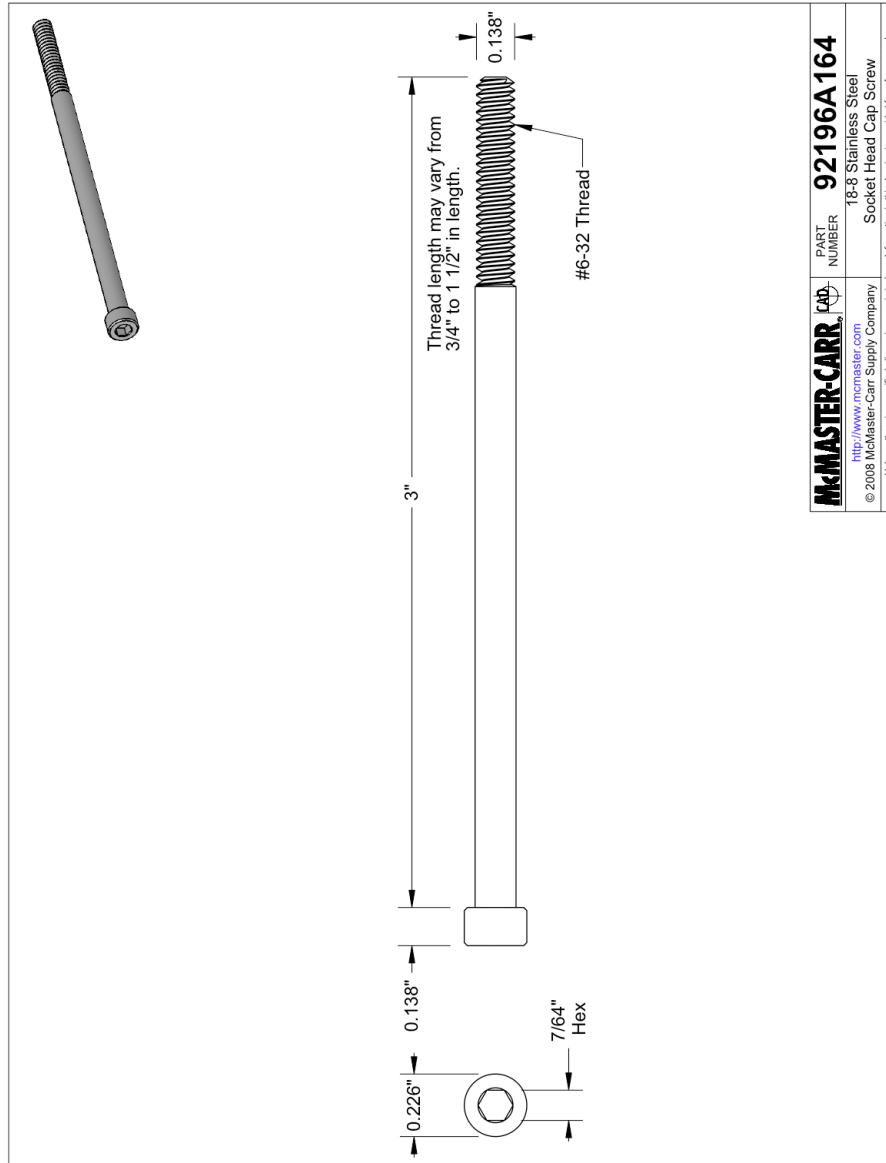


Figure A.3: Preloading screw with #6-32 thread.

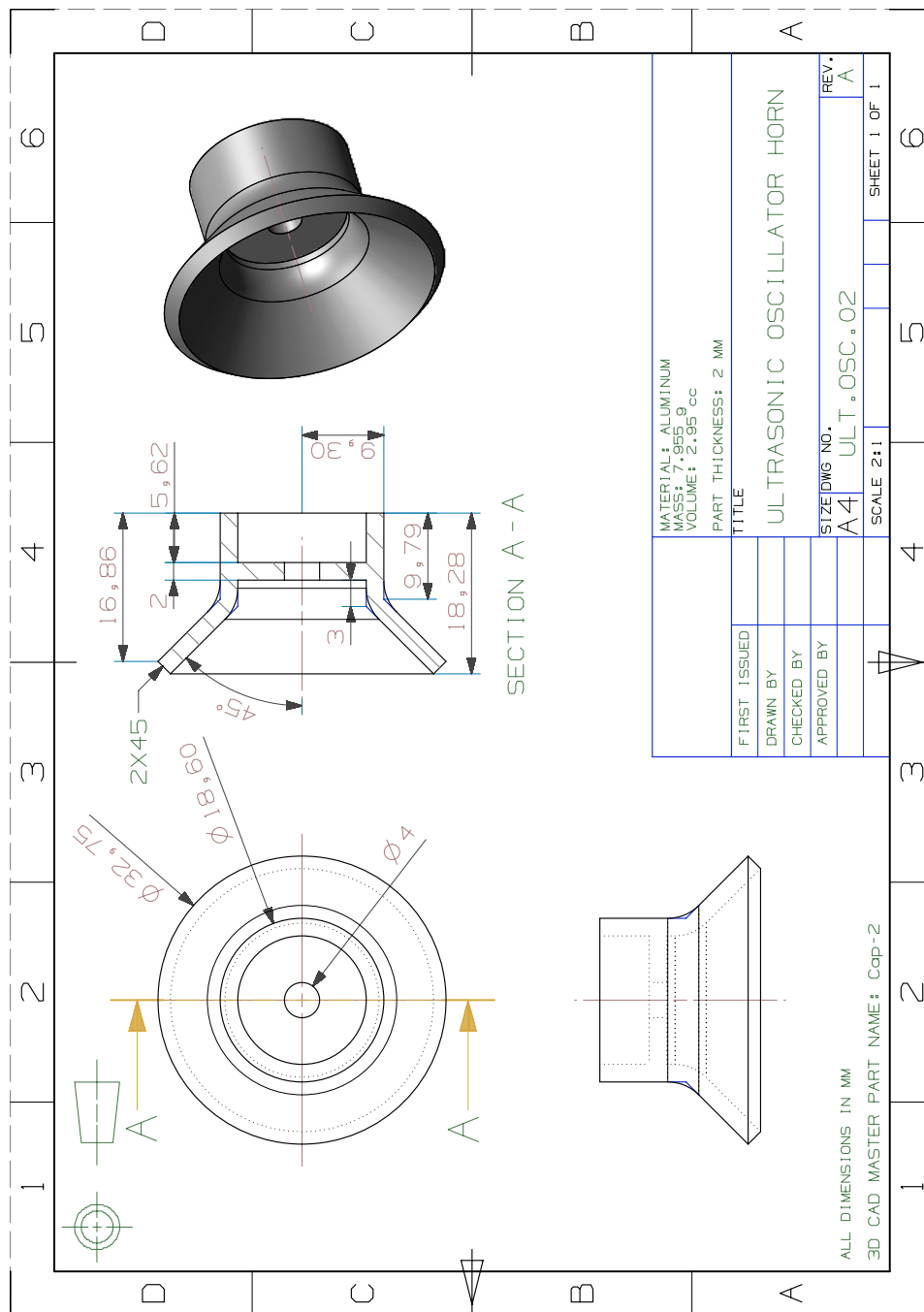


Figure A.4: Aluminum transducer shell.

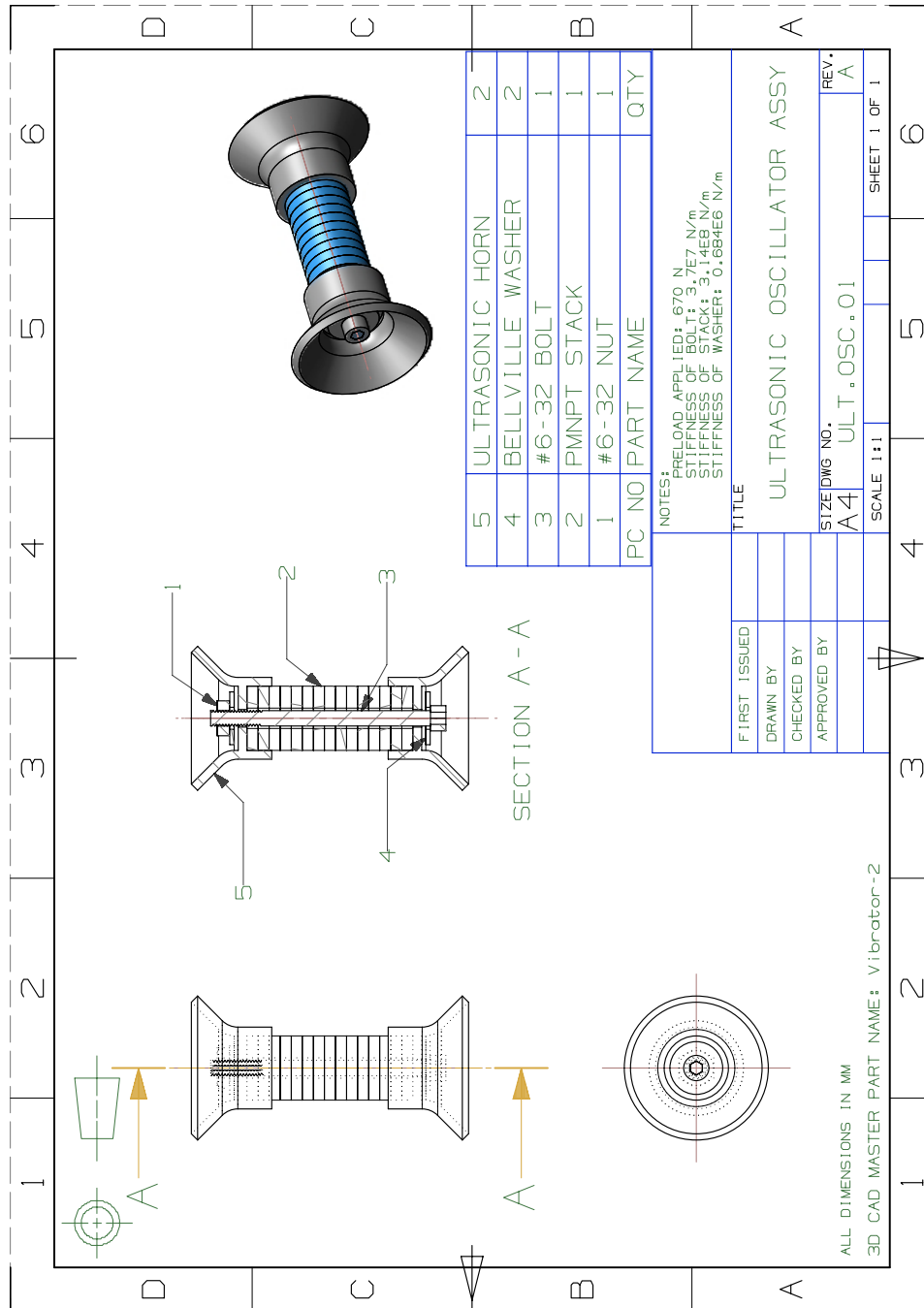


Figure A.5: Aluminum transducer shell.

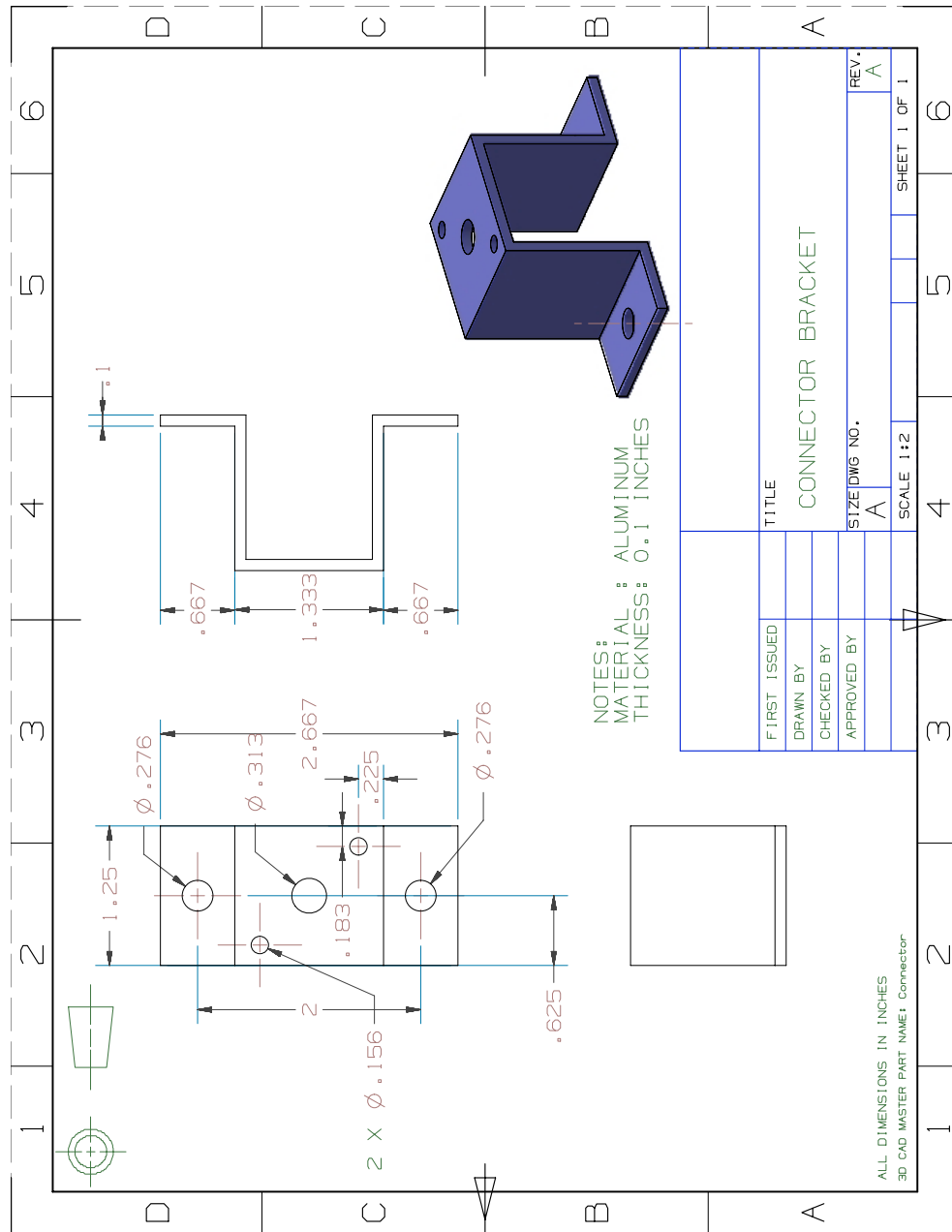


Figure A.6: Connector bracket.

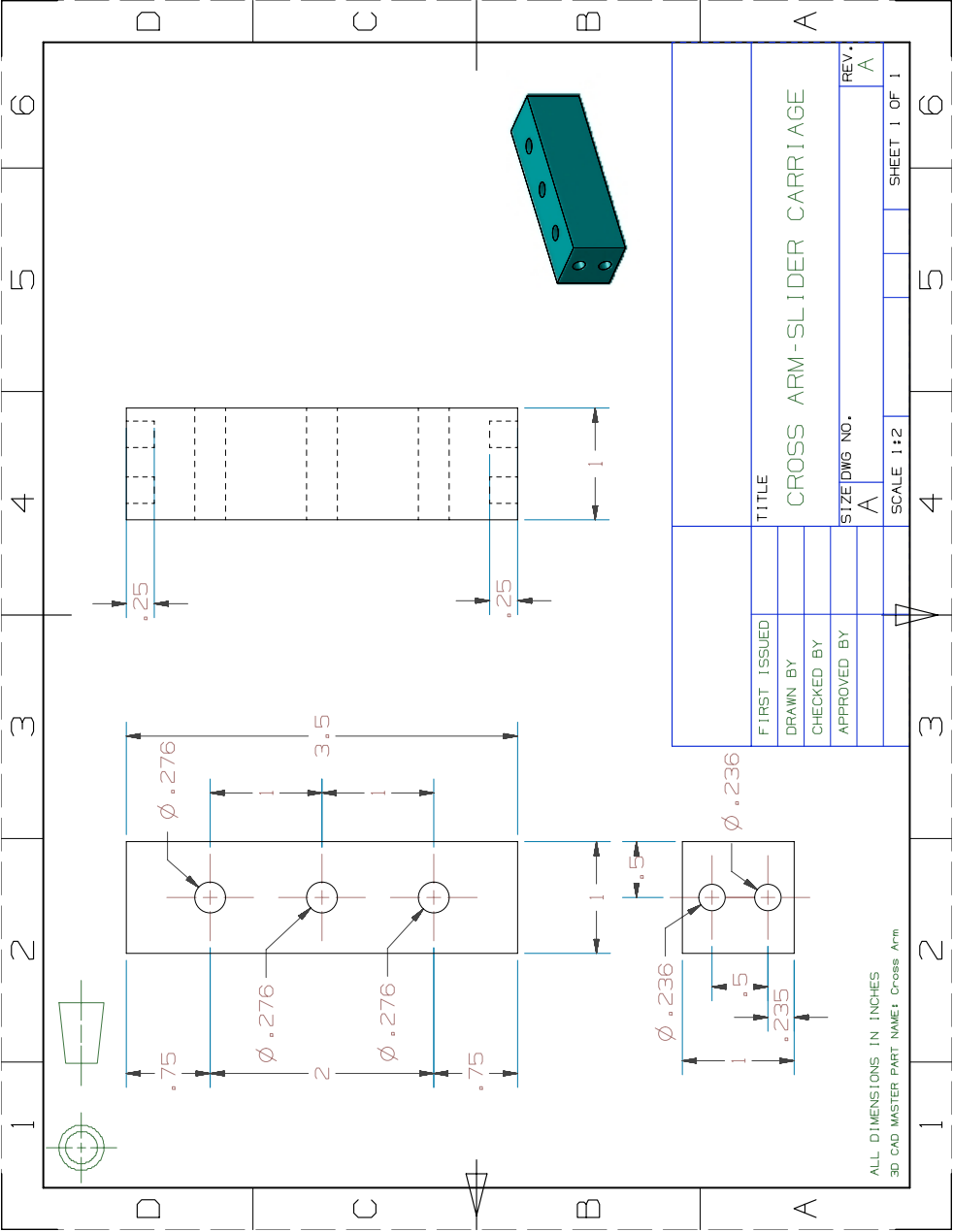


Figure A.7: Cross arm.

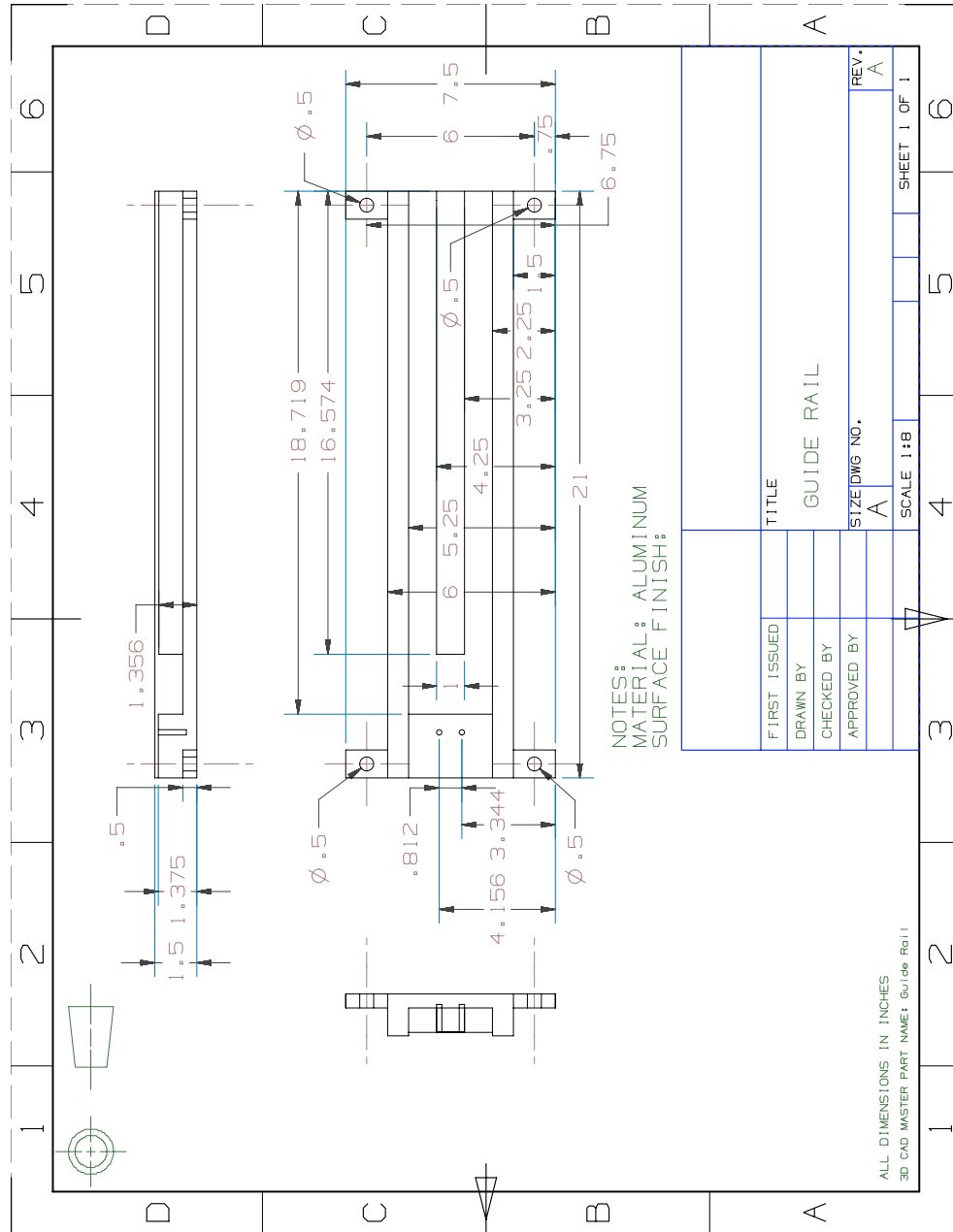


Figure A.8: Guide rail.

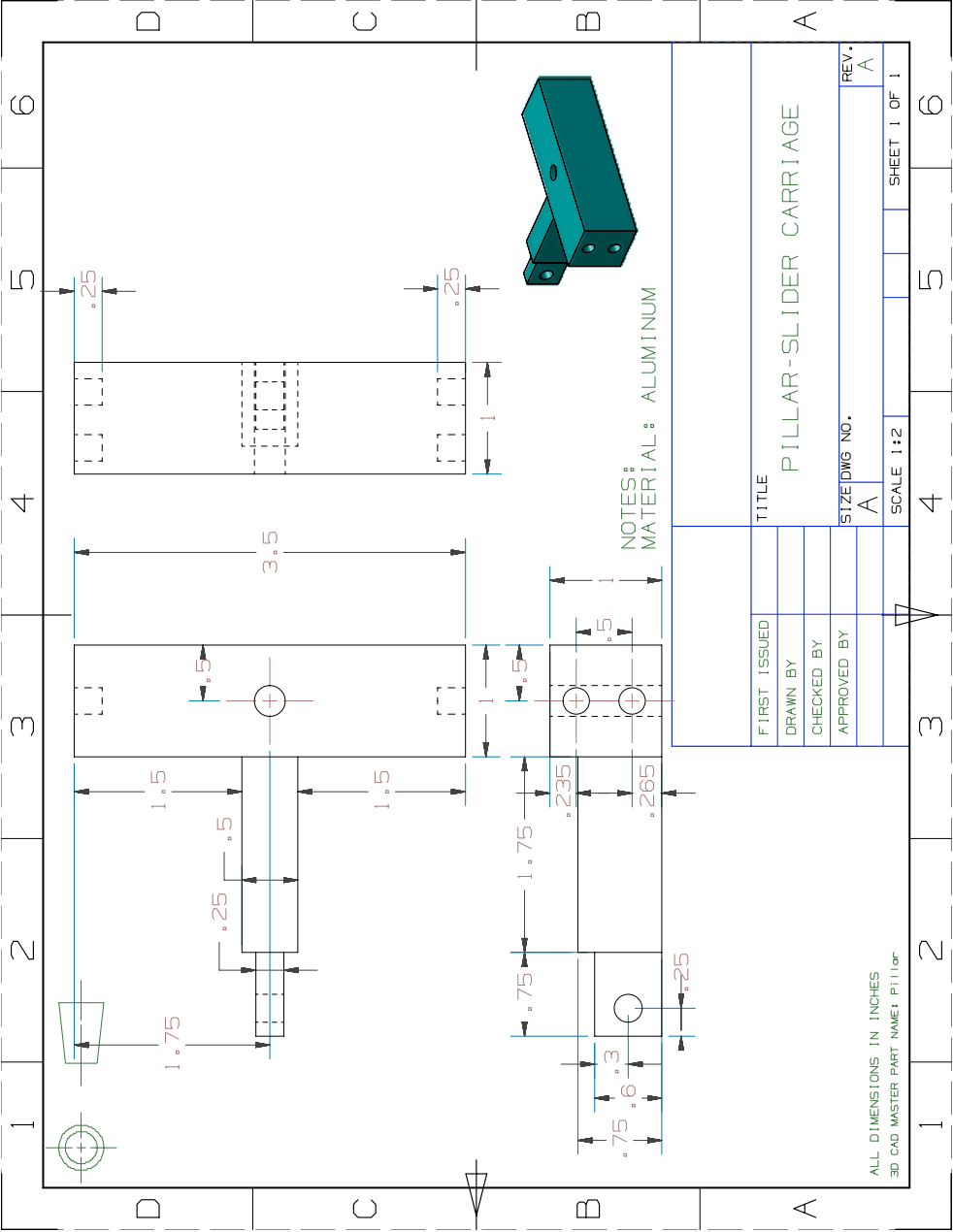


Figure A.9: Pillar.

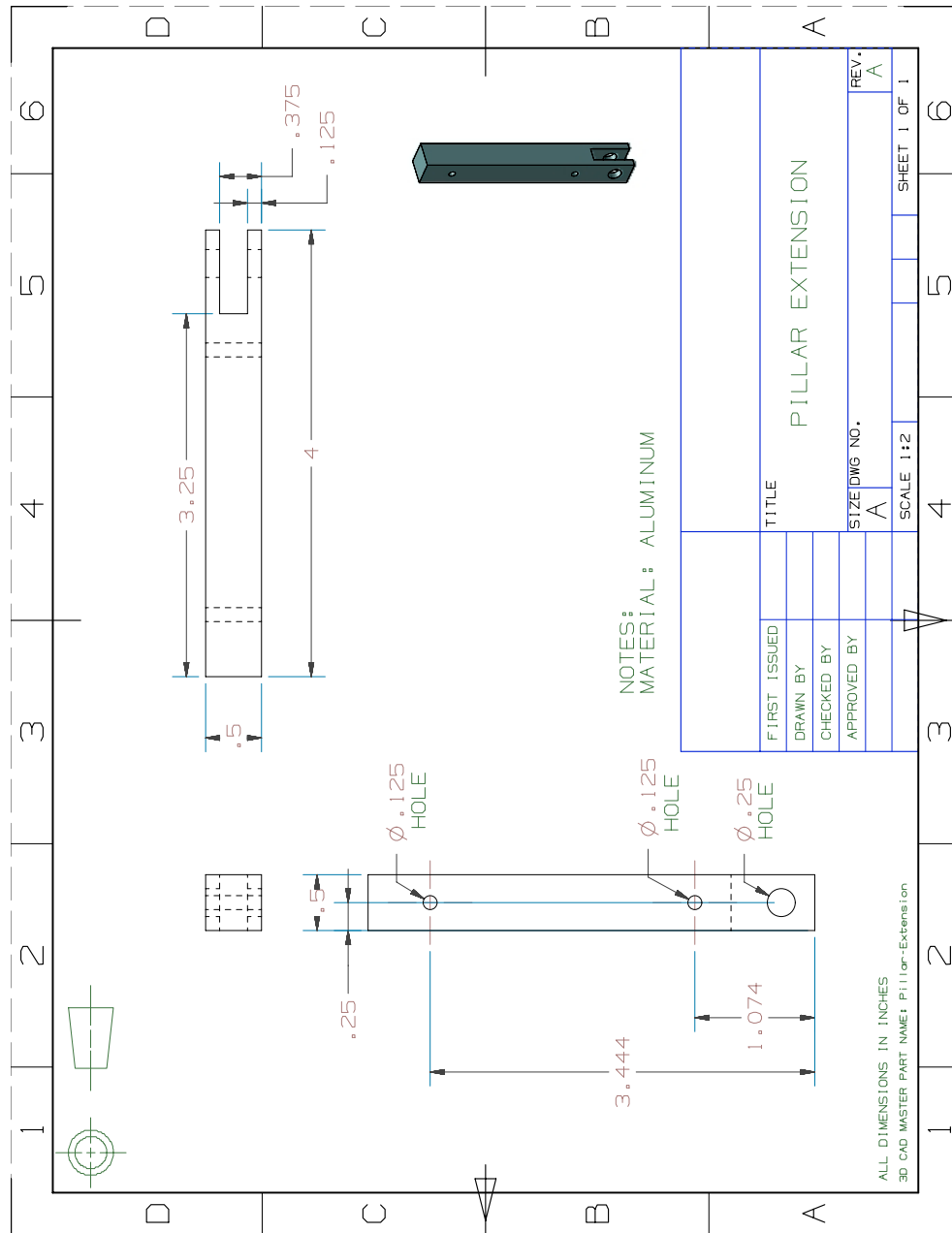


Figure A.10: Pillar Extension.

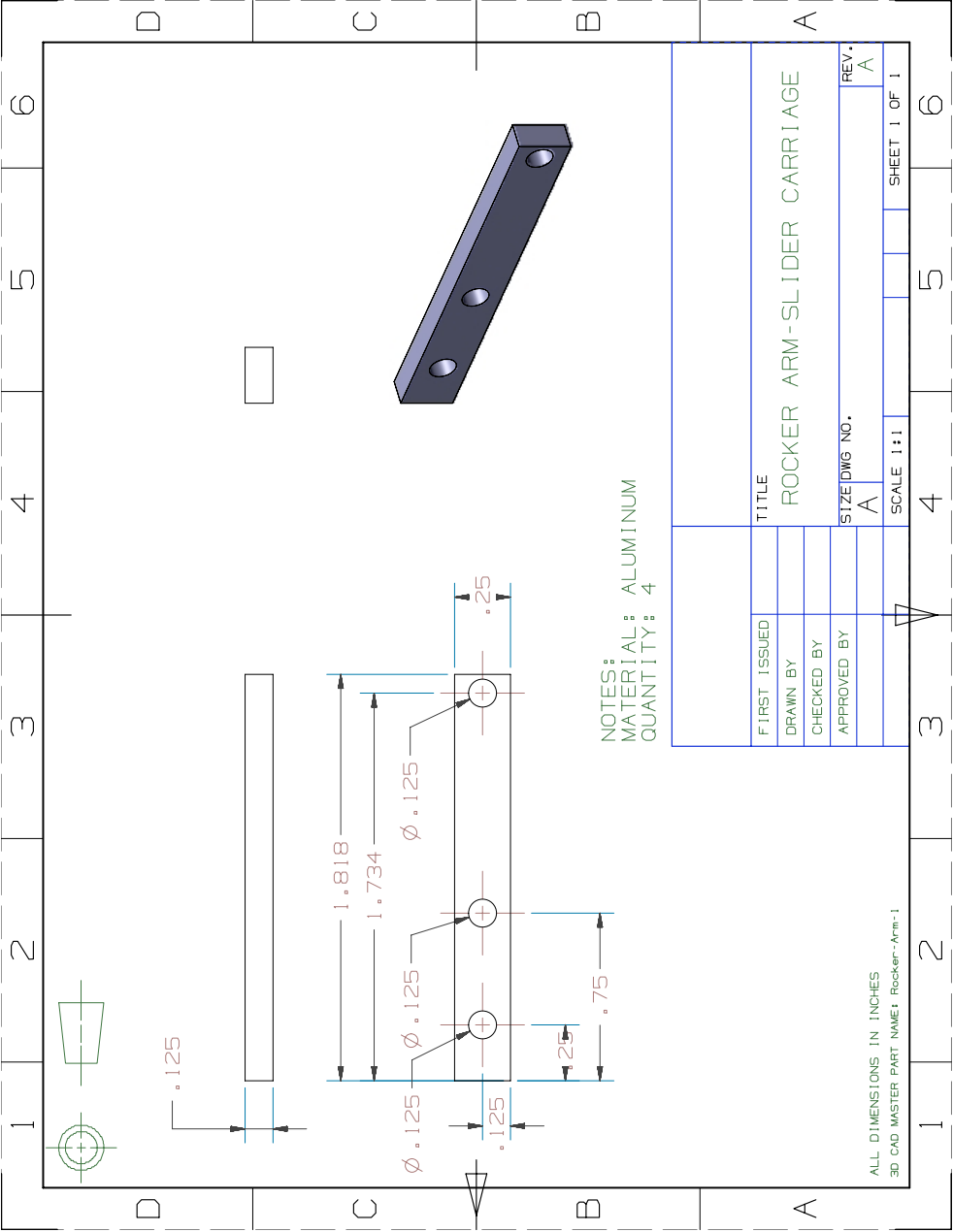


Figure A.11: Rocker arm.

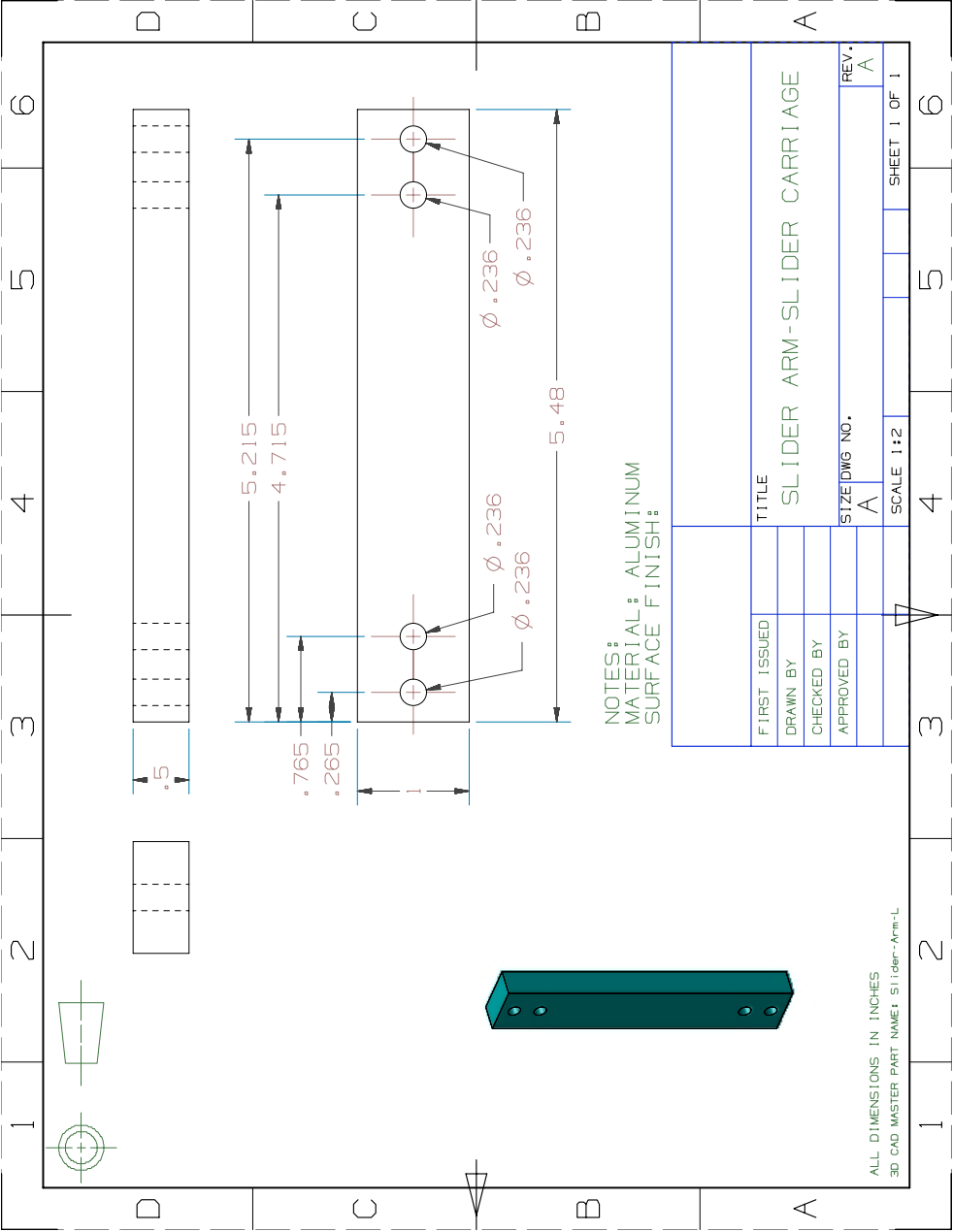


Figure A.12: Slider arm.

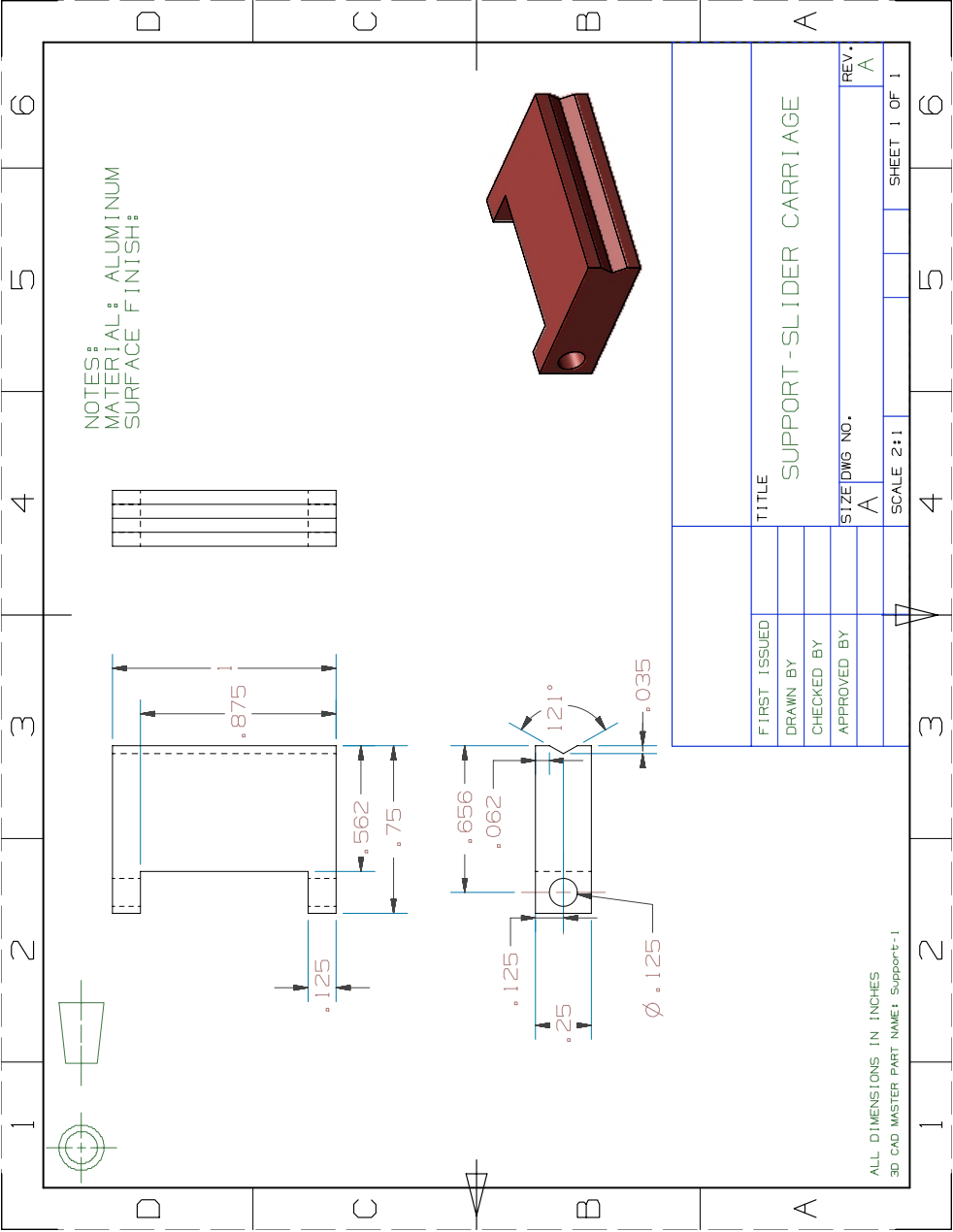


Figure A.13: Support.

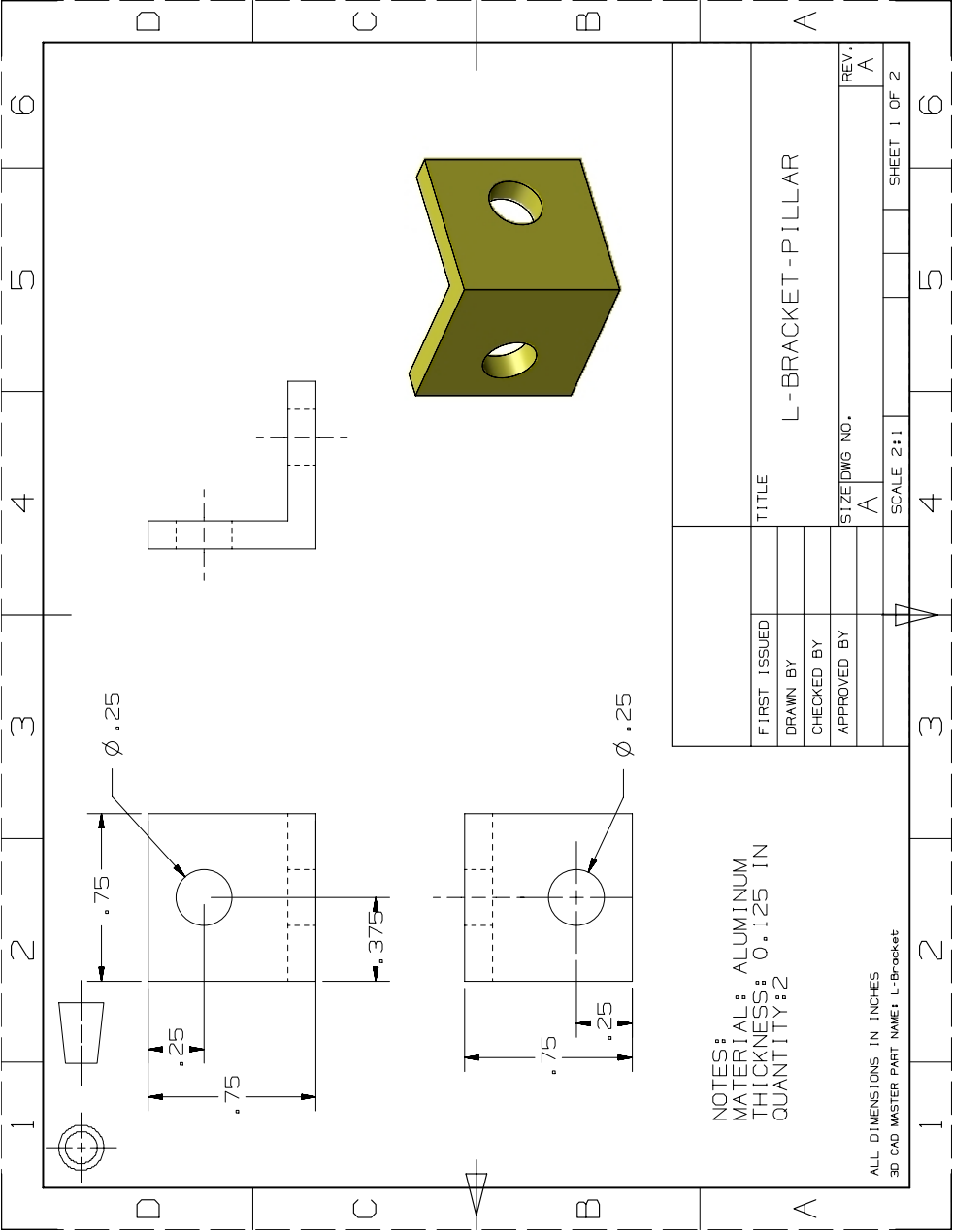


Figure A.14: L-Bracket.

APPENDIX B

DESIGN AND PROTOTYPING OF AN ULTRASONIC MOTOR

B.1 Ultrasonic Motor

A related application of friction and ultrasonic vibrations is the ultrasonic motor (USM). An ultrasonic motor consists of a rotor and a stator ultrasonically excited by piezoelectric elements. Ultrasonic vibrations produced by the piezoelectric elements provide the driving force which are transmitted by friction. USMs have been commercialized and are existent in camera auto-focus mechanisms, nano-positioning and micro-positioning mechanisms. A typical traveling wave ultrasonic motor is shown in Figure B.1. USMs are advantageous because they have a compact design, excellent speed-torque characteristics, silent operation, and accurate due to absence of backlash. Classification of these motors can be based on excitation, construction, or motor function (Figure B.3).

B.2 Mechanism of USMs

A particle at the surface of a transmission bar, in which a flexural travelling wave is guided, moves elliptically. If an object is in contact with the bar, the object will be forced to move by the friction force (Figure B.2).

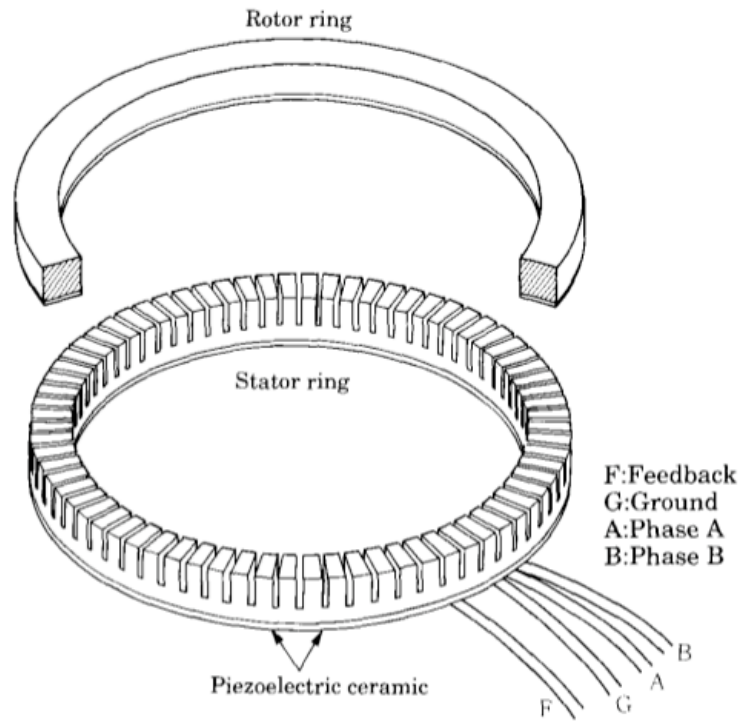


Figure B.1: Ultrasonic motor and parts.

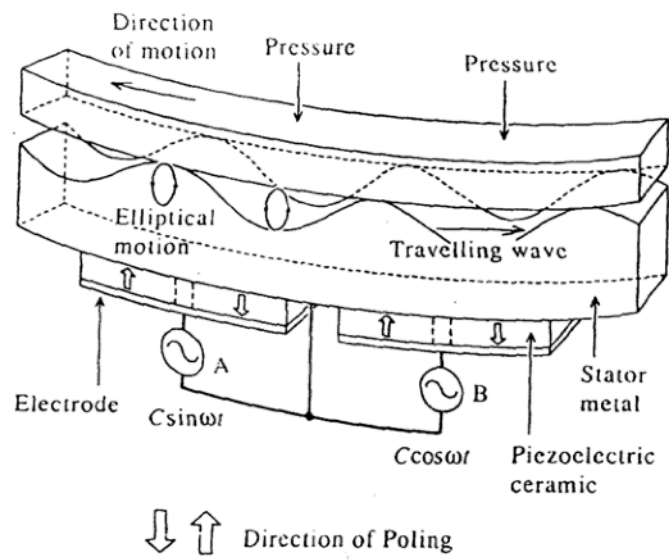


Figure B.2: Principle of traveling wave USM.

ULTRASONIC MOTOR

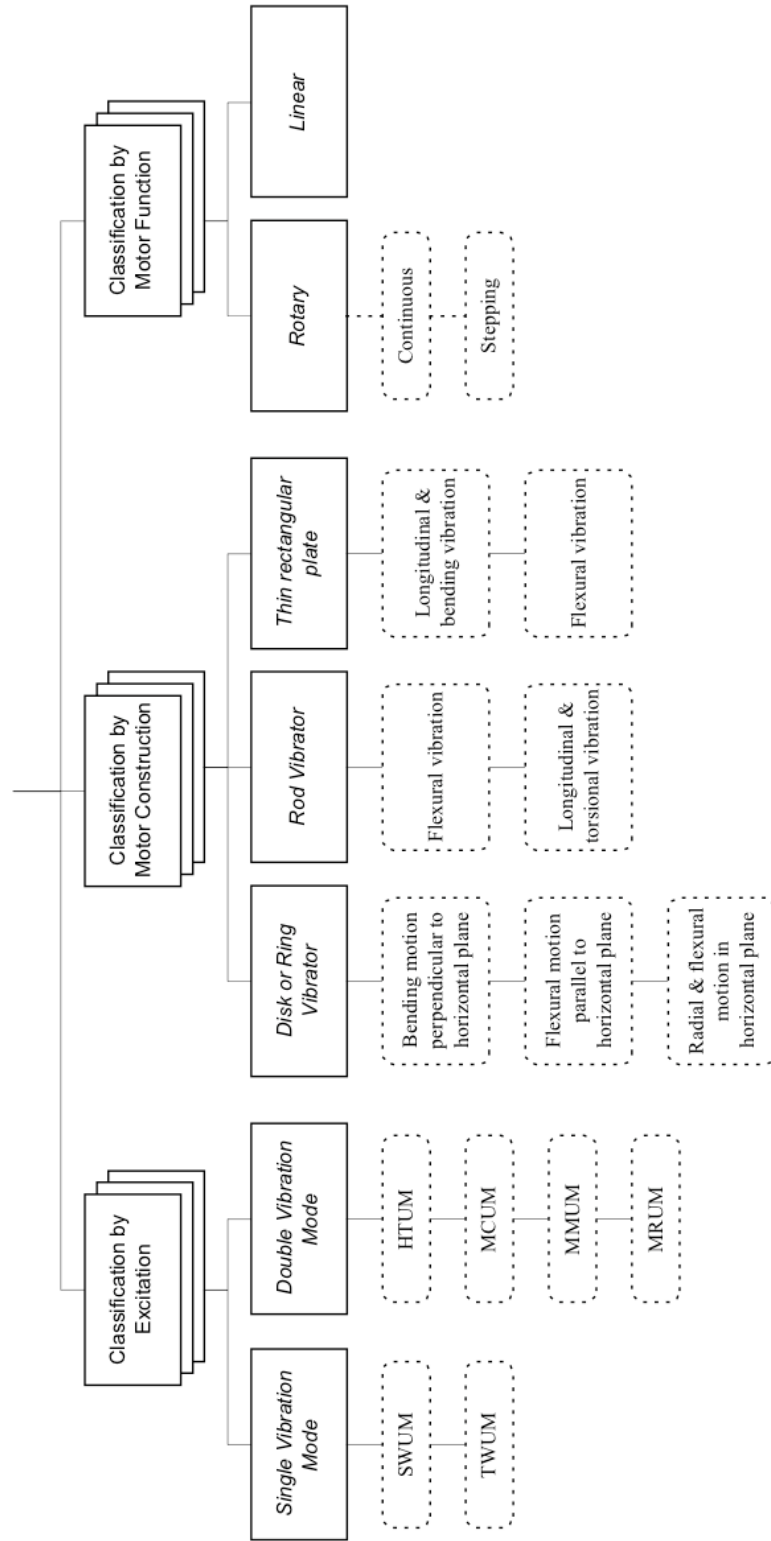


Figure B.3: Classification of USMs.

B.2.1 Equations of Motion

To derive the differential equation of motion for the lateral vibration of beams, forces and moments acting on an element of the beam as shown in Figure B.4. $M(x, t)$ is the bending moment, $V(x, t)$ is the shear force and $f(x, t)$ is the external force per unit length of the beam. The beam in consideration represents the stator.

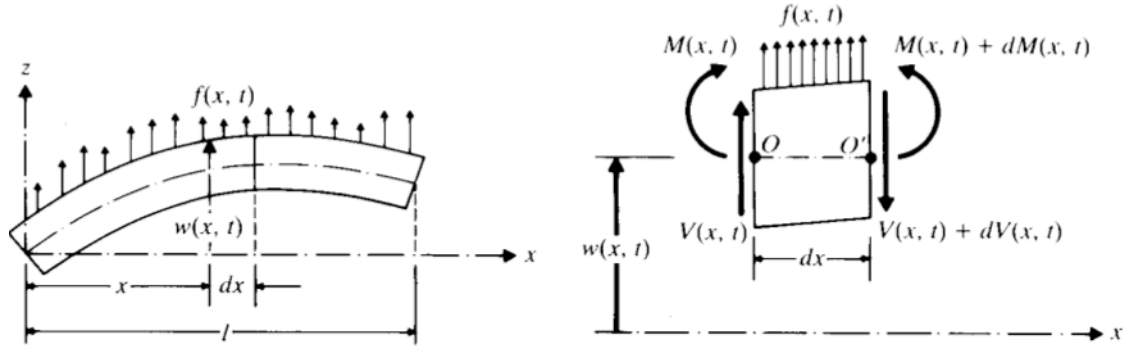


Figure B.4: A beam in bending.

Since the inertia force acting on the element of the beam is,

$$\rho A(x) dx \frac{\partial^2 w}{\partial t^2}(x, t), \quad (\text{B.1})$$

the force equation of motion in the z-direction gives

$$-(V + dV) + f(x, t) dx + V = \rho A(x) dx \frac{\partial^2 w}{\partial t^2}(x, t), \quad (\text{B.2})$$

where ρ is the mass density, and $A(x)$ is the cross-sectional area of the beam. The moment equation about the y axis passing through the point O in Figure B.4 leads to

$$(M + dM) - (V + dV)dx + f(x, t)dx \frac{dx}{2} - M = 0. \quad (\text{B.3})$$

Writing

$$dV = \frac{\partial V}{\partial x} dx \text{ and } dM = \frac{\partial M}{\partial x} dx, \quad (\text{B.4})$$

and omitting terms involving higher order in dx , the above equations can be written as

$$\frac{\partial V}{\partial x}(x, t) + f(x, t) = \rho A(x) \frac{\partial^2 w}{\partial t^2}(x, t). \quad (\text{B.5})$$

$$\frac{\partial M}{\partial x} dx(x, t) - V(x, t) = 0. \quad (\text{B.6})$$

Using the relation $V = \frac{\partial V}{\partial x}$, the following equation is obtained:

$$-\frac{\partial^2 M}{\partial x^2}(x, t) + f(x, t) = \rho A(x) \frac{\partial^2 w}{\partial t^2}(x, t). \quad (\text{B.7})$$

From the theory of bending of beams,

$$M(x, t) = EI(x) \frac{\partial^2 w}{\partial x^2}(x, t), \quad (\text{B.8})$$

where E is the Young's modulus and $I(x)$ is the moment of inertia of the beam cross-section about the y axis.

Inserting equation B.8 into equation B.7, the equation of motion for the forced lateral vibration of a non-uniform beam is obtained:

$$\frac{\partial^2 [EI(x) \frac{\partial^2 w}{\partial x^2}(x, t)]}{\partial x^2} + \rho A(x) \frac{\partial^2 w}{\partial t^2}(x, t) = f(x, t). \quad (\text{B.9})$$

For a uniform beam in free vibration, this equation reduces to:

$$c^2 \frac{\partial^4 w}{\partial x^4}(x, t) + \frac{\partial^2 w}{\partial t^2}(x, t) = 0, \quad (\text{B.10})$$

where $c = \sqrt{\frac{EI}{\rho A}}$.

B.2.2 Motion of Particle on Stator Surface

It is observed in Figure B.2, the particle on the stator moves in an elliptical fashion when traveling waves are generated by piezoelectric elements. This phenomenon is used for actuation. The wave equation for a flexural beam is given by equation . The solution to this equation may be written as,

$$w(x, t) = a \sin(\omega t - kx), \quad (\text{B.11})$$

where a is a constant and ω is the angular frequency of the flexural wave.

The wave number k is expressed as

$$k = \frac{2\pi}{\lambda} = \omega^{1/2}(\rho S/EI)^{1/4}. \quad (\text{B.12})$$

The longitudinal displacement $u(x, z, t)$ can be calculated as

$$u(x, z, t) = -z \frac{\partial w}{\partial x} = azk \cos(\omega t - kx). \quad (\text{B.13})$$

Then, the locus of the particle motion is derived from equations B.12 and B.13 as

$$\frac{u^2}{(azk)^2} + \frac{w^2}{a^2} = 1. \quad (\text{B.14})$$

It is evident from equation B.14 that a particle on the surface of the stator moves

elliptically. By placing a movable object in contact with the flexural traveling wave, the movable rotor will be forced to move along the velocity of the particle at the crests of transverse flexural waves propagating down the beam. As a result, the rotor will move towards the source of the wave. If the direction of propagation of the wave is changed, the rotor similarly changes its direction.

B.3 Simulation Results

Based on the theory of USMs, finite element simulations are performed on a piezoelectric sheet of material PZT- 5H using COMSOL. Table B.1 shows the simulation parameters used.

Table B.1: USM Simulation Parameters

Subdomain	PZT-5A, density - $7750 \text{ kg}/m^3$
Applied voltage	60 V
Applied frequency	40,000 Hz
Default element type	Lagrange - Quadratic
Analysis type	Time dependent
Electrostatics formulation	Symmetric, Electrostatic
Weak constraints	Not applicable
Constraint type	Ideal
Consistent initialization of DAE systems	Backward Euler

B.4 Fabrication of Prototype

A square piezoelectric sheet made of PZT-5A manufactured by Piezo Systems Inc., with dimensions 2.85" X 2.85" X 0.040" is procured for fabricating a USM prototype

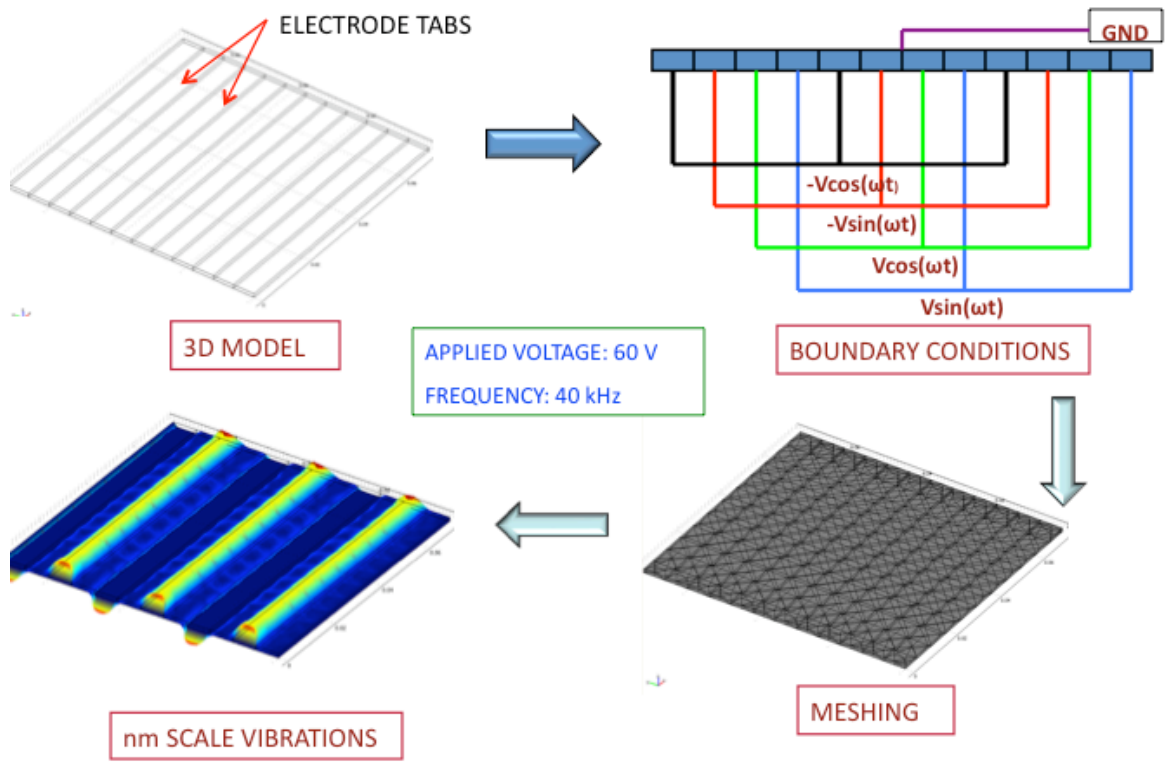


Figure B.5: Simulation results

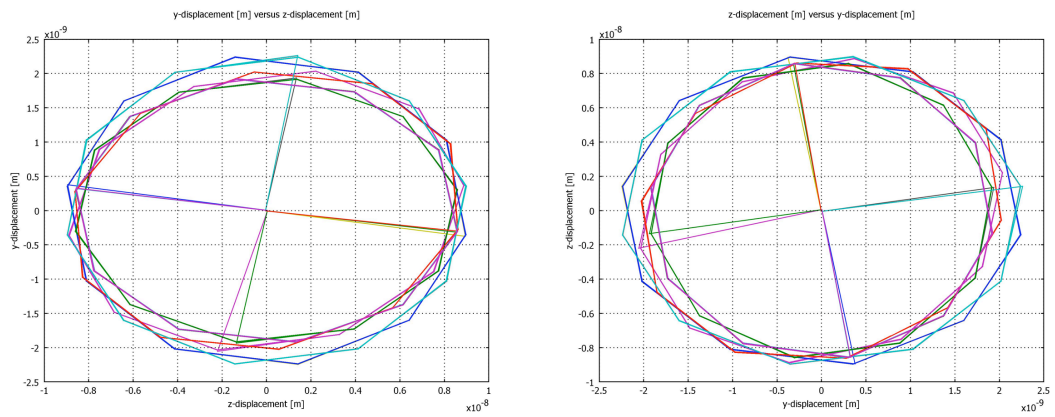


Figure B.6: Plot of Y-displacement vs. Z-displacement.

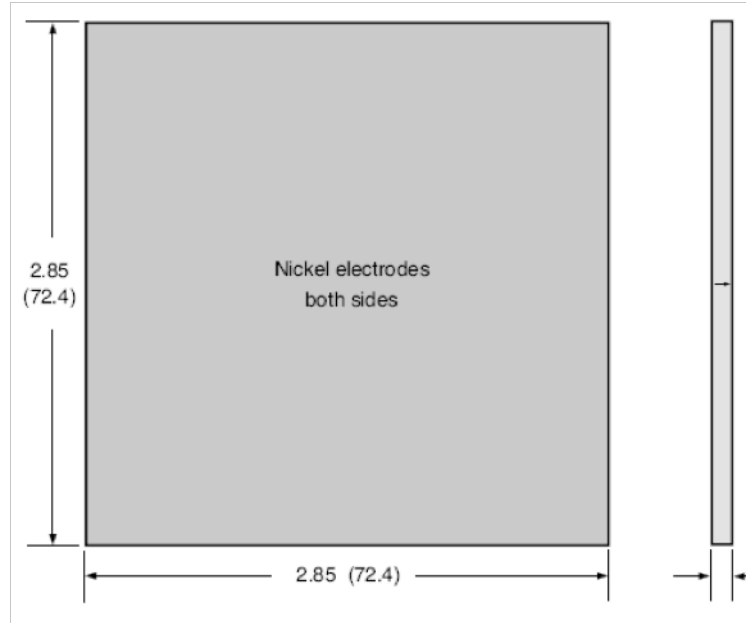


Figure B.7: PZT-5A piezoelectric sheet with Nickel electrodes.

(Figure B.7). This sheet has a thin vacuum sputtered nickel electrodes and produces extremely low current leakage and has low magnetic permeability. It operates over a wide temperature range and is relatively temperature insensitive.

When an electric field having the same polarity and orientation as the original polarization field is placed across the thickness of a single sheet of piezo ceramic, the piece expands along the axis of polarization (thickness direction) and contracts perpendicular to the axis of polarization (length and width direction). The motion in the thickness direction is on the order of tens of nanometers. Motion in the length direction is typically on order of the hundreds of nanometers.

PIEZOELECTRIC			
Composition		Lead Zirconate Titanate	
Piezo Systems Material Designation		Type 5A4E (Industry Type 5A, Navy Type II)	
Relative Dielectric Constant (@1KHz)	KT_3	1800	
Piezoelectric Strain Coefficient	d_{33}	390×10^{-12}	meter/Volt
	d_{31}	-190×10^{-12}	meter/Volt
Piezoelectric Voltage Coefficient	g_{33}	24.0×10^{-3}	Volt meter/Newton
	g_{31}	-11.6×10^{-3}	Volt meter/Newton
Coupling Coefficient	k_{33}	0.72	
	k_{31}	0.35	
Polarization Field	E_p	2×10^6	Volt/meter
Initial Depolarization Field	E_c	5×10^5	Volt/meter
MECHANICAL			
Density	ρ	7800	Kg/meter ³
Mechanical Q		80	
Elastic Modulus	Y^E_3	5.2×10^{10}	Newton/meter ²
	Y^E_1	6.6×10^{10}	Newton/meter ²
THERMAL			
Thermal Expansion Coefficient		$\sim 4 \times 10^{-6}$	meter/meter °C
Curie Temperature		350	°C

Figure B.8: PZT-5A piezoelectric sheet properties.

B.4.1 Selective Removal of Electrode Coating

There are different techniques for removing the electrode coating. In order to erode the electrode layer selectively, any one of the following methods may be used - chemical etching, sandblasting, sandpaper, or laser ablation. The sheet procured from Piezo Systems Inc. has a Nickel electrode coating on the order of 1000 angstroms. This layer is very thin and slight abrasion on the surface can damage the layer. The selective removal is aimed at creating a pattern on the surface of the ceramic. Electrode coating is discrete with tabs separated by a distance of 0.0196". 12 such tabs are created. Thus, the electrode surface is divided into tabs of 0.2196" separated by a gap of 0.0196".

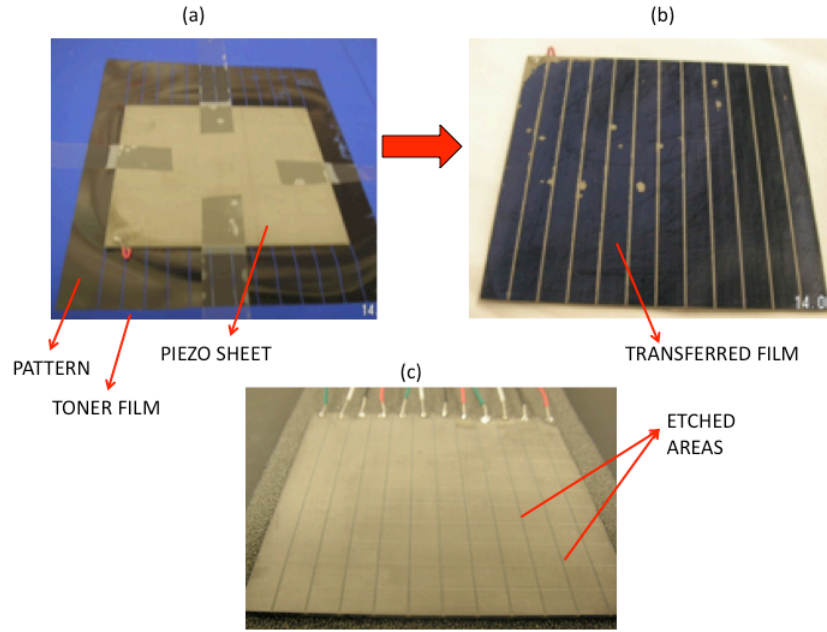


Figure B.9: Selective removal of Ni electrode on piezo sheet.

B.4.1.1 Press and Peel Technology

The required pattern is printed using a laser printer on to the 'Press and Peel' transfer film. The piezo ceramic is placed on the printed pattern of the film. Using a microscope, fine positioning is done to ensure that the desired electrode tabs are in proper position. Once the ceramic is placed, adhesive tape is used to fix its position. The film is then inverted and heat is applied using a pressing iron. The temperature range recommended is 275 °F to 325 °F. After 10 minutes, the heat source is removed and the ceramic with the film is quenched under cool water. The film is carefully peeled off. Figure B.9 shows the patterned electrode.

B.4.2 Phase Shifter Circuit

Based on the simulation results, it is known that the piezo sheet requires four signals, namely sine, -sine, cosine and -cosine. A signal generator creates a sine signal. To obtain a cosine signal, it is required to change the phase of the sine wave by 90 degrees. There are different ways of obtaining a phase shift. By using a differentiator or integrator operational amplifier circuit, a cosine signal can be obtained from a sine signal.

However, the differentiator circuit output tends to be noisy and the integrator circuit output creates a DC bias. At high frequencies, using these circuits do not yield desirable results. Instead, an all-pass filter circuit is created using a LM318 operational amplifier. This is a special filter that passes all frequencies but changes the phase of the signal. Depending on the values of the resistances and capacitances, the amount of phase shift can be adjusted. A typical 90 degree phase shifter all pass filter circuit is shown in Figure B.10. The implemented circuit and electronic setup is shown in Figure B.11.

B.5 Experimental Setup

A schematic of the drive electronics is shown in Figure B.12. Using a signal generator, a sine signal is fed into the all-pass filter circuit. The output cosine and the input sine signals are then passed through linear amplifiers to obtain the signals with opposite polarities. Thus, four signals, each out of phase by 90 degrees, are obtained. These four signals are used to excite the piezo sheet through the patterned electrodes.

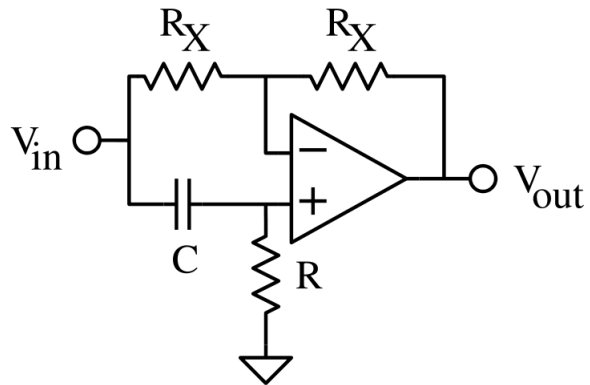


Figure B.10: All pass filter circuit.

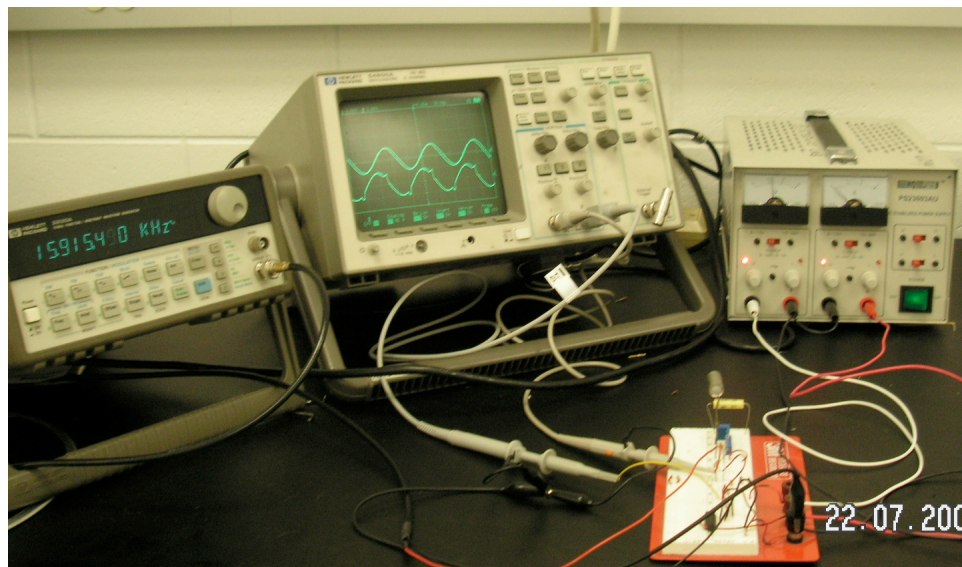


Figure B.11: All pass filter circuit implementation.

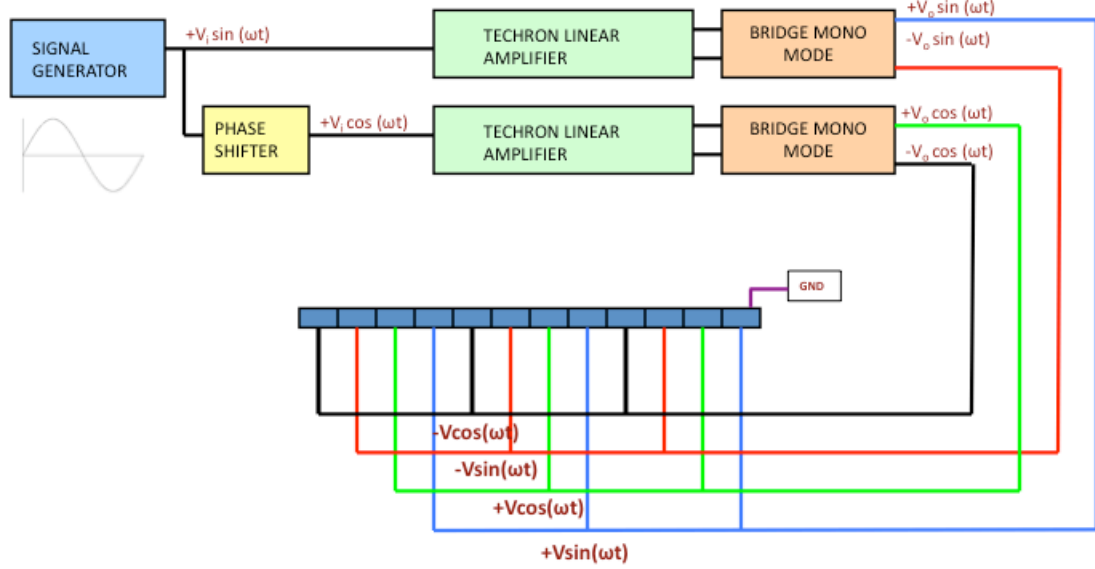


Figure B.12: Drive electronics for USM.

Using a laser vibrometer, the surface of the piezo sheet is scanned and displacement measurements are taken. These measurements are conducted at two frequencies - 20 kHz and 40 kHz. The laser vibrometer used for this purpose is a Polytec PSV 400.

B.6 Laser Vibrometer Measurements

The displacements are found to be on the order of 20 nanometers. However, the mode shapes exhibited are erratic unlike the simulation results. A number of traveling waves are formed on the surface of the stator piezo sheet. This is because the electrode is excited at a single point. The duration for the charge to travel from the source through the entire sheet is finite, particularly at high frequencies. Due to uneven charge distribution, a number of sources for wave propagation exist as is evident in the measurements (Figure B.14 and Figure B.15). Additionally, the phase

shift between the sine and cosine signals changes with frequency since the amplifier adds its own phase shift which may vary between 5 and 10 degrees.

B.7 Final Prototype

The final step is to place a movable object on the surface of the stator. In this case, a steel washer is placed on the piezo sheet. Due to erratic mode shapes on the surface, the rotor is found to move in a random fashion. At particular points on the surface, when traveling waves oppose each other at a distance, motion is created and transferred to the rotor (washer). As the voltage is increased, the speed of rotation also increases. The final prototype is shown in Figure B.13.

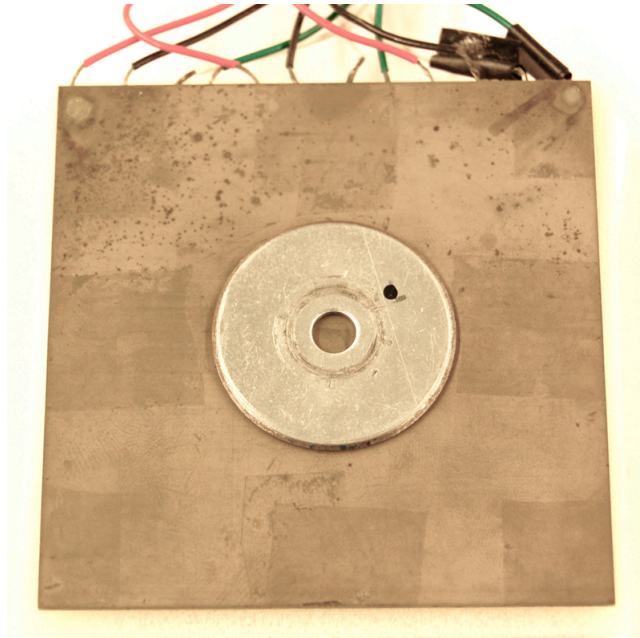


Figure B.13: Final prototype of ultrasonic motor.

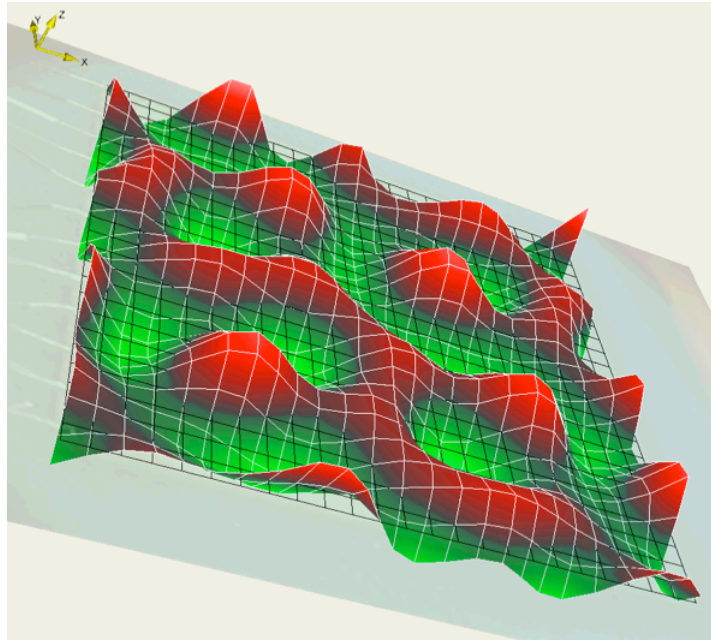


Figure B.14: Displacement measurement by laser vibrometer at 20 kHz.

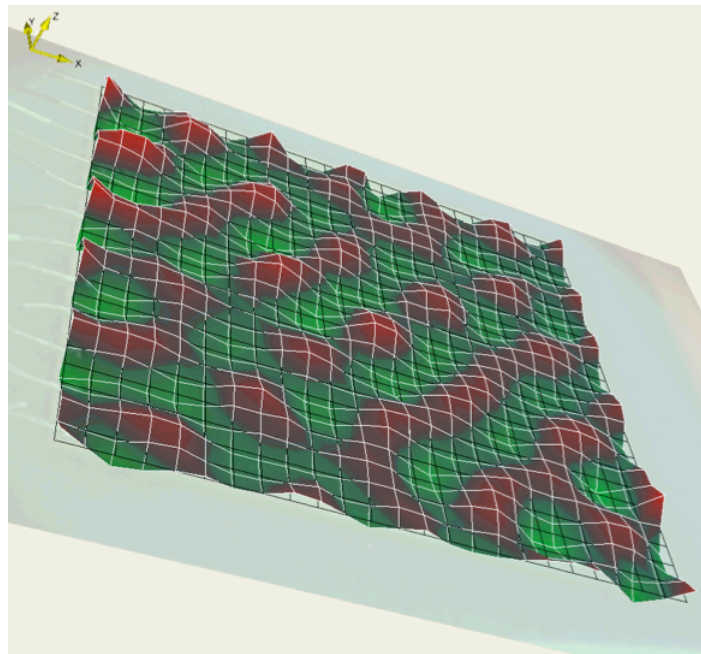


Figure B.15: Displacement measurement by laser vibrometer at 40 kHz.

B.8 Conclusion

A working prototype of an ultrasonic motor is designed and fabricated. The coefficient of friction between the stator (piezo sheet) and the rotor (washer) is critical. Since USMs are friction drives, a high coefficient of friction is desirable at the interface to prevent slip. In conventional USMs, a metallic layer is adhered to the top of the piezo element. This layer has “teeth” on its surface which transmit the motion to the rotor. Their purpose is to mechanically amplify the displacements produced by the piezoelectric sheet.

This research was conducted in order to understand potential applications of USMs in automotive systems. Based on this study, it can be concluded that these motors are more suited for low torque applications. Even with high friction at the interface of the stator and rotor, high torque transmission through friction is a challenge. USMs are one of the latest advances in the field of piezoelectric technologies. The contact mechanics in USMs can be correlated to the principle of active friction control using ultrasonics. This study supplements practical studies conducted in the field of ultrasonics and friction.

BIBLIOGRAPHY

- [1] J. Badertscher, K. Cunefare, and A. Ferri. “Braking impact of normal dither signals”. *Journal of Vibration and Acoustics*, 129:18–23, 2007.
- [2] B. Bhushan. *“Introduction to tribology”*. John Wiley and Sons, 2002.
- [3] K. Cunefare and A. Graf. “Experimental active control of automotive disc brake rotor squeal using dither”. *Journal of Sound and Vibration*, 250(4):277–287, 2002.
- [4] P. R. Dahl. “A solid friction model”. *Aerospace Corp. El Segundo, CA Report A029140*, 1968.
- [5] H.D. Fridman and P. Levesque. “Reduction of static friction by sonic vibrations”. *Journal of Applied Physics*, 30(10), 1959.
- [6] K. F. Graff. *“A history of ultrasonics”*. Academic Press, 1981.
- [7] K. F. Graff. *“High power ultrasonics and transducers in depth”*. Edison Welding Institute, March 2009.
- [8] M. A. Heckl and I. D. Abrahams. “Active control of friction control induced oscillations”. *Journal of Sound and Vibration*, 193(1):417–426, 1996.
- [9] T. Hesjedal, G. Behme, and W. E. Oliu. “The origin of ultrasound-induced friction reduction in microscopic mechanical contacts”. *IEEE Trans. Ultrasonics, Ferroelectrics, and Frequency Control*, 49(3):356–364, 2002.
- [10] D. P. Hess and A. Soom. “Normal vibrations and friction under harmonic loads: Part I - Hertzian contacts”. *Journal of Tribology*, 113(80), 1991.
- [11] T. Ikeda. *“Fundamentals of Piezoelectricity”*. Oxford University Press, UK, 1990.
- [12] W. D. Iwan. “A distributed-element model for hysteresis and its steady-state dynamic response”. *Journal of Applied Mechanics*, 33:893–900, 1966.

- [13] V. C. Kumar and I. M. Hutchings. “Reduction of the sliding friction of metals by the application of longitudinal or transverse ultrasonic vibration”. *Tribology International*, 37(10):833–840, 2004.
- [14] R.A. LeMaster and K. F. Graff. “Influence of ceramic location on high power transducer performance”. *Ultrasonics Symposium Proceedings*, pages 296–299, 1978.
- [15] M. Leus and P. Gutowski. “Analysis of longitudinal tangential contact vibration effect on friction force using Coulomb and Dahl models”. *Journal of Theoretical and Applied Mechanics*, 46:171–184, 2008.
- [16] S. Lin and F. Zhang. “Measurement of ultrasonic power and electro-acoustic efficiency of high power transducers”. *Ultrasonics*, 37:549–554, 2000.
- [17] W. Littmann, H. Storck, and J. Wallaschek. “Reduction in friction using piezo-electrically excited ultrasonic vibrations”. *SPIE’s 8th International Symposium on Smart Structures and Materials*, 4331:302–311, 2001.
- [18] W. Littmann, H. Storck, and J. Wallaschek. “Sliding friction in the presence of ultrasonic oscillations: superposition of longitudinal oscillations”. *Archive of Applied Mechanics*, 71:549–554, 2001.
- [19] M. Michaux, A. Ferri, and K. Cunefare. “Effect of tangential dither signal on friction induced oscillations in an SDOF model”. *Journal of Computational and Nonlinear Dynamics*, 2:201–210, 2007.
- [20] A. M. Mitskevich. “Motion of a body over tangentially vibrating surface, taking into account of friction”. *Soviet Physics-Acoustics*, 13:348–351, 1968.
- [21] E. A. Neppiras. “The pre-stressed piezoelectric sandwich transducer”. *International Conference on Ultrasonic Proceedings*, page 195, 1973.
- [22] H. Olsson, K. J. Aström, C. Canaudas de Wit, M. Gäfvert, and P. Lischinsky. “Friction models and friction compensation”. *European Journal of Control*, 1998.
- [23] R. Pohlman and E. Lehfeldt. “Influence of ultrasonic vibration on metallic friction”. *Ultrasonics*, 4:178–185, 1966.
- [24] T. Sashida and T. Kenjo. “*An introduction to ultrasonic motors*”. Oxford: Clarendon Press, UK, 1993.
- [25] H. Storck, W. Littmann, J. Wallaschek, and M. Mracek. “The effect of friction reduction in the presence of ultrasonic vibrations and its relevance to traveling wave ultrasonic motors”. *Ultrasonics*, 40:379–383, 2002.

- [26] R. Stribeck. “Kugellager Für beliebige Belastungen Zeitschrift des Vereins Deutscher Ingenieure”. *Band 45*, 3:73–79, 1901.
- [27] C. C. Tsai and C. H. Tseng. “The effect of friction reduction in the presence of in-plane vibrations”. *Archive of Applied Mechanics*, 75:164–176, 2005.